Contents

List of Figures

List of Tables

Todo list

Chapter 1

Introduction

In 2012, the Large Hadron Collider (LHC) has detected a new particle compatible with the boson predicted by the Higgs-Englert-Brout mechanism, which explains the spontaneous electro-weak symmetry breaking. Although the energy and luminosity upgrades could improve the knowledge on this new particle and also find existence of physics beyond the Standard Model (SM), the complex environment of the events generated by the LHC hide fundamental parameters that help to perform precise measurements.

One of the biggest scientific projects is being prepared. The International Linear Collider (ILC) will be a linear eletron-positron collider with a length of 31 kilometres and a center of mass energy $\sqrt{s} = 250 \ - \ 500$ GeV (with a possible upgrade to 1 TeV). It will be able to perform more accurate measurements of known particles (like the coupling of Higgs boson to the fermions), but also to study the dark matter and physics beyond the SM. This project imposes new challenges on the instrumentation side. For example, to measure the Higgs coupling to the charm quarks, a precise measurement of the secondary vertices created close to the interaction point is needed. The inner part of the detector dedicated to reconstruct vertices should combine a good spatial resolution ($\leqslant 3\ \mu$m) and a material budget of less than a thousand of the radiation length (X_0). This subdetector, called vertex detector, should be optimised to perform tracking in a high density particles environment. The PLUME collaboration is developing tools to overcome this challenge thanks to an innovative concept of double-sided pixelated ladders for tracking, called Pixelated Ladder with Ultra-low Material Embedding (PLUME). This detector is equipped with six CMOS pixels sensors, placed next to each other on each side of a very light mechanical structure. The collaboration tries to reach a material budget close to 0.35 % X_0. For each track, two positions will be measured, one on each side. This double-measurement will help to determine the intersection point of the particle with the detector, but also to know the origin and the movement of the particles.

Different aspects of the vertex detector development are discussed in the thesis. This work gives an overview of the validation and characterisation of such complicated detector and aims to give its performances, such as the spatial resolution, the benefits of double-sided measurements and the material budget of such device. The document is organised as followed: the theoretical context is presented in chapter 2, with an overview of the SM and theories beyond the SM. Chapter 3 describes the experimental context of the thesis, by presenting the future linear collider, the ILC, and focusing especially on one of the experiment, the International Large Detector (ILD). Chapter 4 introduced the different physics studies that will be performed at the ILC and focus especially on a possible analysis of the $\nu\overline{\nu}H$ channel at the ILC. In chapter 5, the different Vertex Detector (VXD) for the ILD are presented, as well as a description of the PLUME collaboration and the status of the detectors produced. The three last chapters are devoted to the studies performed during this thesis. In chapter 6, the validation in the laboratory of the different PLUME modules are reported. Chapter 7 is presenting the observation of the ladder deformation during a test beam campaign which was done in 2011 at CERN. It also shows the benefits of a double-sided measurement compared to a single-sided ladder. Chapter 8 deals with the measurement of the radiation length of the first fully working PLUME ladder, which has a weighted material budget (X_0) estimated to be 0.65 % X_0. Finally, the conclusion summarises the work performed during the thesis and the outlook is discussed.

Chapter 2

The secrets of nature

This chapter attempts to understand the world around us using a mathematical framework which describes the matter and its interaction. Firstly, the laws that rule the Universe will be presented. Then, it will focus on the mathematical framework itself with the description of three interactions: the electromagnetic interaction (EM), the weak and the strong interaction. Afterward, a framework that unifies the EM and weak interaction, as well as the spontaneous symmetry breaking will be studied. Finally, the limits of this theory and the possible solution to overcome these issues will be tackled.

Contents

2.1 The Standard Model

2.1.1 Introduction

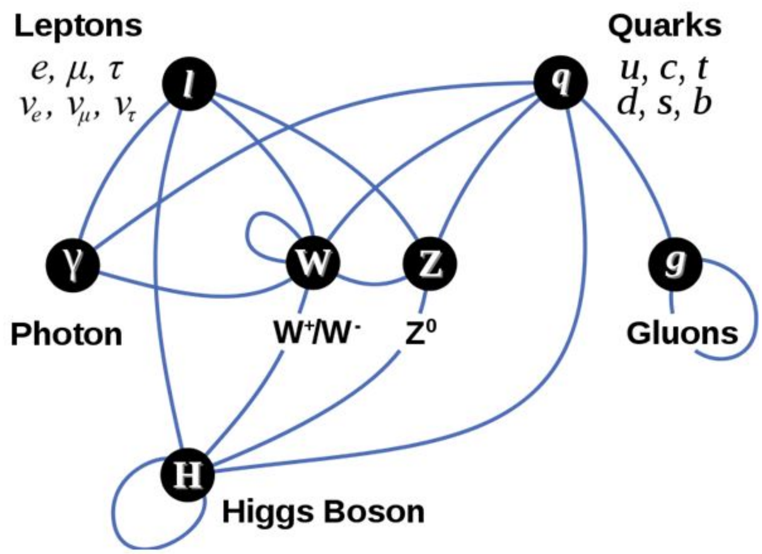

Figure 2.1 – Summary of the Standard Model particles with their interactions [67].

The Standard Model (SM) is a theory describing the elementary structure of the matter. It is one of the most successful achievements in modern physics. The elegant theoretical framework of the SM is explaining experimental results but predicts also a wide variety of phenomena. It depicts the interactions between the fundamental constituents of matter, called elementary particles. A quantum formalism describes an elementary particle with a set of quantum numbers. This quantum numbers are the spin, the intrinsic angular momentum, the parity P, the electric charge, etc. They are used to distinguish the 'matter' particles from the 'force carrier' particles.

The half-integer spin particles obey to the Fermi-Dirac statistics and are submitted to the Pauli exclusion principle: they cannot occupy the same quantum state at the same time. These particles, that are the constituents of the matter, are called fermions and they are to the number of twelve types. The fermions are divided into two categories: the leptons and the quarks.

They are six lepton types: three charged particles and three neutral ones, called neutrino ν. At the end of the 19$^{\text{th}}$ century, the first fundamental particles, the electron (e^-) was discovered by Thomson. The two other charged leptons were discovered in 1937 for the muon (μ) and in 1975 for the tau (τ). Three neutrinos are associated to the three flavored leptons: the electron neutrino (ν_e) discovered in 1953, the muon neutrino (ν_μ) in 1962 [27] and the tau neutrino (ν_τ) discovered in 2000 [17].

The quarks are to the number of six. They cannot be found alone in nature. They are carrying a quantum number: the color. The color quantum numbers are green, blue and red (and the anti-color associated). They are always in a bounded state to form composite particles that are colorless and are called hadrons. A quark and an anti-quark form an integer spin composite particle, called a meson. Three quarks bounded together are called baryons. The most known baryons are the proton and the neutron. They are made of the up quarks (u) and the down quarks (d). The other quarks were discovered in the second half of the 20$^{\text{th}}$ century. The strange quark (s) was discovered in 1968, followed by the charm quark (c) in 1974. Then, the bottom quark or beauty quark (b) was discovered in 1977. The last quark discovered was the top quark (t) in 1995.

Depending on the particle's mass, the fermions are divided into three categories called generation. The first generation of particles forms the ordinary matter and is composed of the electron, the electron neutrino, the u and d quarks. The two other generations are particles found in cosmic rays or in collisions with accelerators. All the fermions and their properties are summarised in table 2.1.

There is a second type of particles called bosons or gauge bosons. They have an integer spin and are following the Bose-Einstein statistics. Contrary to the fermions, the bosons are not limited to a single state occupancy. The bosons are the mediators of the four fundamental interactions, which are the followings:

EM interaction: It describes the interaction between two charges particles. It is mediated by the photon γ, a massless and chargeless spin 1 particle.

Weak interaction: It is the interaction responsible for the β radioactive decay (a nucleon decays into another one with the emission of a lepton and a neutrino). The mediators of the weak interaction are the neutral

Type	Family	Particle	L	B	Q_e	Mass (MeV)
Leptons	1^{st}	e	1	0	-1	0.511
		ν_e	1	0	0	$< 2 \times 10^{-6}$
	2^{nd}	μ	1	0	-1	105.66
		ν_μ	1	0	0	$< 2 \times 10^{-6}$
	3^{rd}	τ	1	0	-1	1.78×10^3
		ν_τ	1	0	0	$< 2 \times 10^{-6}$
Quarks	1^{st}	u	0	1	2/3	$2.3^{+0.7}_{-0.5}$
		d	0	1	-1/3	$4.8^{+0.5}_{-0.3}$
	2^{nd}	s	0	1	-1/3	95 ± 5
		c	0	1	2/3	$1.275 \times 10^3 \pm 2.5$
	3^{rd}	b	0	1	-1/3	$4.66 \times 10^3 \pm 30$
		t	0	1	2/3	$173.21 \times 10^3 \pm 511 \pm 711$

Table 2.1 – Summary of the 12 types fermions. L is a quantum number associated to the leptons. Its value is 1 for leptons and -1 for anti-leptons. B is a quantum number associated to the baryons. It is equal to 1 for a baryon and to -1 for an anti-baryon [60].

electrical charged boson (Z^0) and two electrical charged bosons (W^+ and W^-).

Strong interaction: It is responsible for the cohesion of the atom's nucleus, as well as the hadrons' cohesion. There are eight mediators called gluons.

Gravitational interactional: It is not described by the SM, but a quantum theory intends to associate a spin 2 boson, called graviton to the gravitational force. Nevertheless, finding a framework describing the equation of the general relativity and the equation of the quantum numbers is a difficult challenge.

Another boson is predicted by the SM but is not associated to a fundamental interaction, rather to the mass generation mechanism. It is the Higgs boson (H) that has been discovered in 2012 at the LHC [15][16]. The mass generation mechanism of particles is presented in section 2.2.2.

Table 2.2 summarises the different bosons of the SM.

2.1.2 Quantum Field Theory

The SM is based on a mathematical framework called Quantum Field Theory (QFT). It is a gauge theory, in which a Lagrangian describes an interaction following a particular symmetry. A symmetry is a transformation applied to a system that leaves it invariant. In 1918, Emmy Noether has demonstrated that all continuous symmetries of a system implies the conservation of a quantity during its evolution [58]. For examples, symmetries under space translation and time translation imply respectively conversation of linear momentum and conversation of energy.

In QFT, the interactions are described by following gauge group:

$$\mathrm{SU_C}(3) \otimes \mathrm{SU_L}(2) \otimes \mathrm{U_Y}(1), \tag{2.1}$$

with $\mathrm{SU_L}(2) \otimes \mathrm{U_Y}(1)$ the symmetry group of the electroweak (EW) interaction. The subscript L means that only the left-handed particles are interacting in the weak interaction, whereas the subscript Y is associated to the hypercharge. The gauge symmetry group associated to the strong interaction is $\mathrm{SU_C}(3)$. The subscript C means that only the particles that have a color charge are interacting via the strong interaction.

The gauge theory is invariant under a continuous set of local transformation. Taking the gauge symmetries and the least action into account, physicists were able to set up equations that describe the dynamic of the interactions by a Lagrangian. The steps to build Lagrangian for the three forces and the unification of the EM and weak interactions are going to be presented.

Force	Gauge bosons	Mass (GeV/c^2)	Electric charge	Range
Electromagnetic	γ	0	0	∞
Weak	Z^0	91.1876 ± 0.0021	0	10^{-18} m
	$W^\pm$	80.3980 ± 0.0250	± 1	
Strong	g (8 gluons)	0	0	10^{-15} m
	H	125 GeV	0	

Table 2.2 – Summary of the interactions and the bosons defined in the Standard Model [60]. The range corresponds to the distance on which the interaction is still effective. As the gravitational interaction is not part of the SM, the graviton is not included in this table.

Quantum Electrodynamic

Quantum Electrodynamic (QED) is the QFT that combines the electromagnetism and the quantum mechanics formalisms. The interactions are described using a relativistic Lagrangian that is invariant under a continuous set of transformation. For a free fermion with a mass m, the Dirac Lagrangian $\mathcal{L}_{\text{Dirac}}$ is:

$$\mathcal{L}_{\text{Dirac}} = \overline{\Psi}\,(x)\,(i\gamma^{\mu}\partial_{\mu} - m)\,\Psi\,(x)\,, \tag{2.2}$$

with $\Psi\,(x)$ the spinor field describing the fermion and γ^{μ} are the Dirac matrices.

As QED is built on a local gauge symmetry, the Lagrangian must be invariant under global U(1) transformations:

$$\begin{array}{rcrcl} \Psi\,(x) & \rightarrow & \Psi'\,(x) & = & e^{-i\alpha}\Psi\,(x)\,, \\ \overline{\Psi}\,(x) & \rightarrow & \overline{\Psi}'\,(x) & = & e^{i\alpha}\overline{\Psi}\,(x)\,. \end{array} \tag{2.3}$$

The corresponding local symmetry is:

$$\begin{array}{rcrcl} \Psi\,(x) & \rightarrow & \Psi'\,(x) & = & e^{-i\alpha(x)}\Psi\,(x)\,, \\ \overline{\Psi}\,(x) & \rightarrow & \overline{\Psi}'\,(x) & = & e^{i\alpha(x)}\overline{\Psi}\,(x)\,. \end{array} \tag{2.4}$$

By applying the transformation of equation 2.3, the Lagrangian from equation 2.2 becomes:

$$\mathcal{L}'_{\text{Dirac}} = \mathcal{L}_{\text{Dirac}} - \overline{\Psi}\gamma^{\mu}\Psi\partial_{\mu}\alpha. \tag{2.5}$$

Although the mass term of the Lagrangian in equation 2.5 stays invariant under the local symmetry, the term containing a partial derivative does not. To keep the Lagrangian invariant, a gauge field A_{μ} is introduced:

$$A_{\mu} \rightarrow A_{\mu} - \frac{1}{e}\partial_{\mu}\alpha. \tag{2.6}$$

Moreover, the partial derivative is replaced by a covariant one:

$$D_{\mu}\Psi\,(x) = (\partial_{\mu} - iQ_{e}A_{\mu})\,\Psi\,(x)\,. \tag{2.7}$$

The gauge field is not yet a dynamic field. To get a physical gauge field, a kinetic term should be added to the equation. This gauge invariant term that includes derivative from the A_μ field is:

$$F_{\mu\nu} = \partial_\mu A_\nu - \partial_\nu A_\mu. \tag{2.8}$$

The Lagrangian, which is local invariant, is the one that describes the QED:

$$\mathcal{L}_{\mathrm{QED}} = \overline{\Psi}(x)\left(i\gamma^\mu D_\mu - m\right)\Psi(x) - \frac{1}{4}F_{\mu\nu}(x)\,F^{\mu\nu}(x)\,. \tag{2.9}$$

A mass term $mA_\mu A^\mu$ for the field A_μ is missing because it would break the gauge invariance. That consideration matches to the fact that the photon is a massless boson.

Add details on the QED: coupling...

Weak interaction

In 1930, Pauli has explained the continuous spectrum of the electron in the β decay by the existence of new particle which respects the principle of energy conservation. It is a light particle, which does not interact so much with matter.

After the discovery of the neutron by Chadwick in 1932 [13], Fermi wrote a theory on weak interaction to explain the β decay [31]. He postulated that the neutron is decaying into a proton by emitting an electron and a light neutral particle, called neutrino. In analogy to the electromagnetism, he proposed a current-current Lagrangian to describe the β decay.

$$\mathcal{L}_{\mathrm{weak}} = \frac{G_F}{\sqrt{2}}\left(\overline{p}\gamma_\mu n\right)\left(\overline{e}\gamma_\mu \nu\right), \tag{2.10}$$

where, G_F is the Fermi constant $G_F = 1.166 \cdot 10^{-5}$ GeV^{-2}. p, n, e and ν are respectively the vector currents describing the proton, the neutron, the electron and the neutrino.

Nevertheless, the non-relativistic limit leads to an incomplete theory. The interaction considered with a 2-components spinor transforms a proton into a neutron without changing the position, the spin or the parity. However, Lee and Yang have postulated in 1956 that the weak interaction violates the parity after analysing the decays of the τ and θ particles [51]. The Wu experiment [74] confirmed this hypothesis in 1957 by studying the decay of ^{60}Co.

The Fermi interaction was modified by Feynman and Gell-Mann [32] to a $V - A$ theory[1]. The vector current is now subtracted by an axial vector current. For example, the neutrino current is replaced by:

$$\begin{aligned}\overline{e}(x)\gamma_\mu\nu \quad \rightarrow \quad & \overline{e}\gamma_\mu(1-\gamma_5)\nu \\ & = \overline{e}\gamma_\mu\nu - \overline{e}\gamma_\mu\gamma_5\nu,\end{aligned} \tag{2.11}$$

with $\overline{e}\gamma_\mu\nu$ a current vector and $\overline{e}\gamma_\mu\gamma_5\nu$ an axial current vector.

It was established that the weak current has the form $V - A$ instead of $V + A$. The weak interaction is only coupling left-handed particles and right-handed anti-particles. The Lagrangian describing the weak interaction can be written as a current interaction:

$$\mathcal{L}_{\text{weak}} = -\frac{G_F}{\sqrt{2}} J^\mu J^\dagger_\mu, \tag{2.12}$$

and J^μ is a combination of leptonic and hadronic currents.

Contrary to QED, the weak interaction obeys to a non-Abelian symmetry group[2], the SU(2) symmetry group. The matter field could be represented as a doublet Ψ_L and a singlet Ψ_R of this group.

$$\Psi_L = \begin{pmatrix}\nu_{eL} \\ e_L\end{pmatrix}, \quad \Psi_R = e_R. \tag{2.13}$$

The generators of the group are the three Pauli matrices σ_i, associated with a gauge field W^i_μ. The bosons of the weak interactions are the $W^\pm$ and Z.

As the left-handed leptons are combined into a doublet, a quantum number called weak isospin (I_3) is associated with them. The charged leptons have a weak isospin $I_3 = -\frac{1}{2}$ and for the neutrinos $I_3 = \frac{1}{2}$. Concerning the gauge bosons $W^\pm$ and Z, the weak isospin is respectively $I_3 = \pm 1, 0$.

Quantum Chromodynamics

Quantum Chromodynamics (QCD) is the quantum field theory of the strong interaction. In this model, the interaction is due to an SU(3) gauge group.

[1] V stands for vector and A for axial-vector

[2] A group is non-Abelian when the elements of the group are not commutating.

It produces 8 gauge fields called gluons. The spinors of this theory are the six quarks that form a triplet with respect to the gauge symmetry.

The SU(3) gauge group is a group of $9-1=8$ real parameters and of 8 generators. Those generators are the Gell-Mann matrices. The normalised generators are defined by:

$$T^a = \frac{1}{2}\lambda^a. \tag{2.14}$$

The structure constant f^{abc} can be expressed as:

$$if^{abc} = 2Tr([T^a, T^b]T^c). \tag{2.15}$$

Each of them is considered as a triplet state with respect to the SU(3) group:

$$q_i = \begin{pmatrix} q_i^1 \\ q_i^2 \\ q_i^3 \end{pmatrix}, \tag{2.16}$$

where q_i are the six quarks, that can have three different states, called color. These charged colors are red, blue and green.

As the local gauge symmetry U(1) is included into the SU(3) group, the gauge field A_μ is modified to be:

$$A_\mu = g_S A_\mu^a \frac{\lambda^a}{2}, \tag{2.17}$$

with $a = 1, \cdots, 8$ and corresponds to the 8 gluons. To keep the gauge invariance, there is no mass term $m_g A_a^\mu A_\mu^a$. Then, the gluons are massless.

The covariant derivative is also rewritten to keep the gauge invariance:

$$\begin{aligned} D_\mu &= \partial_\mu - iA_\mu \\ &= \partial_\mu - ig_S A_\mu^a \tfrac{\lambda^a}{2}. \end{aligned} \tag{2.18}$$

The QED field $F_{\mu\nu}$ is not gauge invariant in QCD. Nevertheless, an additional term to obtain gauge invariant field tensor can be introduced:

$$G_{\mu\nu}^a = \left(\partial_\mu A_\nu^a - \partial_\nu A_\mu^a\right) + g_S f^{abc} A_\mu^b A_\nu^c. \tag{2.19}$$

Finally, the QCD Lagrangian is given by:

$$\mathcal{L} = \sum_{i=1}^{6} \bar{q}_i \left(i\gamma^\mu D_\mu - m_i \right) q_i - \frac{1}{4} G^a_{\mu\nu} G^{\mu\nu}_a \tag{2.20}$$

2.2 Towards a unified theory

Late 1960, a model of unification was postulated by Glashow, Weinberg, and Salam to describe the electroweak (EW). The theory rests on a $\mathrm{SU(2)_L} \otimes \mathrm{U(1)_Y}$ symmetry group. It is the simplest group which conserves the properties of EM charge conversion and parity violation of weak interaction.

For the EW unification, the $\mathrm{U(1)_{EM}}$ symmetry group describing the EM interaction has to be rewritten. As the fermions are considered by left-handed doublets and right-handed singlets, the $\mathrm{U(1)_{EM}}$ breaks the gauge invariance. The weak isospin group $\mathrm{SU(2)_L}$ is combined with the EM charge to create the hypercharge give by the Gell-Mann-Nishijima relation:

$$Q = I_3 + \frac{1}{2} Y. \tag{2.21}$$

The I_3 term is the third component of the weak isospin. With the introduction of the hypercharge, the EM gauge invariance is conserved.

The EW Lagrangian is:

$$\mathcal{L}_{\mathrm{EW}} = \mathcal{L}_{\mathrm{YM}} + \mathcal{L}_{\mathrm{fermions}}. \tag{2.22}$$

The first term $\mathcal{L}_{\mathrm{YM}}$ is the Yang-Mills Lagrangian that describes the bosons gauges interactions (kinetic term + interaction between bosons). It has the form below:

$$\mathcal{L}_{\mathrm{YM}} = -\frac{1}{4} \mathbf{W}^a_{\mu\nu} \mathbf{W}^{a\mu\nu} - \frac{1}{4} \mathbf{B}_{\mu\nu} \mathbf{B}^{\mu\nu}, \tag{2.23}$$

where $\mathbf{W}^a_{\mu\nu}$ $(i = 1, 2, 3)$ and $\mathbf{B}_{\mu\nu}$ are the gauge fields corresponding respectively to SU(2) and U(1) groups. The tensors of these fields are written:

$$\mathbf{W}_{\mu\nu} = \partial_\mu \mathbf{W}_\nu - \partial_\nu \mathbf{W}_\mu - ig[\mathbf{W}_\mu, \mathbf{W}_\nu] \text{ and} \tag{2.24}$$

$$\mathbf{B}_{\mu\nu} = \partial_\mu \mathbf{B}_\nu - \partial_\nu \mathbf{B}_\mu. \tag{2.25}$$

Where g is the coupling constant of the SU(2) gauge group. In equation 2.24, $\mathbf{W}_\mu = \sum W^i_\mu \sigma^i/2$ is a vector of three gauge fields associated to $\mathrm{SU(2)_L}$ and σ^i are the Pauli matrices. The term $[\mathbf{W}_\mu, \mathbf{W}_\nu]$ is associated to the interactions between the gauge fields. In equation 2.25, $\mathbf{B}_\mu$ is the only gauge field associated to the $\mathrm{U(1)_Y}$ gauge group.

The Lagrangian describing the fermions field is given by:

$$\mathcal{L}_{\text{fermions}} = \overline{\Psi}_L \gamma^\mu D_\mu \Psi_L + \overline{\Psi}_R \gamma^\mu D_\mu \Psi_R, \tag{2.26}$$

with:

$$\begin{aligned} D_\mu \Psi_L &= \left(\partial_\mu + ig\mathbf{W}_\mu - i\tfrac{g'}{2} Y \mathbf{B}_\mu\right) \Psi_L \text{ and} \\ D_\mu \Psi_R &= \left(\partial_\mu - i\tfrac{g'}{2} Y \mathbf{B}_\mu\right) \Psi_R. \end{aligned} \tag{2.27}$$

In equation 2.27, the covariant derivative has two forms. The weak interaction does not allow coupling of the W bosons to right-handed fermions, whereas the γ and Z bosons do.

With the EW Lagrangian described above, the gauge bosons are considered as massless fields. The electroweak interaction does not allow a $m\overline{\Psi}\Psi$ term because it does not transform as a scalar under $\mathrm{SU(2)_L} \otimes \mathrm{U(1)_Y}$. Moreover, the $m^2 \mathbf{W}_\mu \mathbf{W}^\mu$ violates the $\mathrm{SU(2)_L}$ gauge invariance of the Lagrangian. The mass terms associated with the physical fields of the gauge bosons are given by a spontaneous symmetry breaking via the Higgs mechanism.

2.2.1 Symmetry Breaking mechanism and Goldston theorem

Before introducing the Higgs mechanism, the spontaneous symmetry breaking is presented for a global symmetry. This phenomenon appears in other physics fields, such as the phase transition or laser theory.

A Lagrangian density for a complex scalar field ϕ is considered here:

$$\mathcal{L} = \partial^\mu \phi^* \partial_\mu \phi - \mu^2 \phi^* \phi - \lambda(\phi^* \phi)^2, \tag{2.28}$$

where $\partial^\mu \phi^* \partial_\mu \phi$ is the kinetic term of a complex scalar field and $\mu^2 \phi^* \phi - \lambda(\phi^* \phi)^2$ is related to a scalar potential. The coefficient μ^2 is a real parameter. Nevertheless, depending on its sign, the potential can take two forms.

If $\mu^2 > 0$, the symmetry is unbroken and the potential has a minimum at $\phi = 0$ which does not degenerate. It describes a particle with a mass μ and a quartic self-coupling. As the transformation $\phi \to -\phi$ is respected, this solution is a symmetric one.

When $\mu^2 < 0$, there is not a unique ground state for this system but multiple states with the same vacuum energy. The minima is located on a circle of radius:

$$v = \sqrt{\frac{-\mu^2}{2\lambda}} > 0. \tag{2.29}$$

By choosing a particular solution as the ground state, the symmetry gets spontaneously broken. A parametrisation of the excitations around the ground state is possible by introducing a new field ϕ:

$$\phi(x) = \frac{1}{\sqrt{2}}\left(v + \rho(x) + i\Theta(x)\right), \tag{2.30}$$

with $\rho(x)$ and $\Theta(x)$ real fields and the value v is given by one of the solution from equation 2.29. By injecting this new field in equation 2.28, the Lagrangian becomes:

$$\mathcal{L} = \frac{1}{2}(\partial_\mu \rho)^2 + \frac{1}{2}(\partial_\mu \Theta)^2 - \lambda v^2 \rho^2 - \lambda v(\rho^3 + \rho\Theta^2) - \frac{\lambda}{4}(\rho^2 + \Theta^2)^2, \tag{2.31}$$

where the field $\rho(x)$ describes a state of mass $m_\rho = 2\mu^2$, coupled to the massless field $\Theta(x)$. The field $\Theta(x)$ describes excitations around a direction in the potential. These excitations are not costing any energy to the system and they correspond to massless bosons called Goldstone bosons.

2.2.2 Higgs mechanism

As seen with the QED and QCD Lagrangian, the bosons generated are massless. Nevertheless, the $W^\pm$ and Z bosons have a mass and equation 2.22 of EW interaction does not include a mass generator. The Higgs-Englert-Brout mechanism solves the origin of the fermions masses [38][26].

The invariant Lagrangian density under $\mathrm{SU(2)_L} \otimes \mathrm{U(1)_Y}$ gauge transformation is:

$$\mathcal{L} = (D^{\mu}\Phi)^{\dagger}(D_{\mu}\Phi) - V(\Phi), \tag{2.32}$$

with Φ a doublet of complex scalar fields defined as following:

$$\Phi = \begin{pmatrix} \phi^{+} \\ \phi^{0} \end{pmatrix}. \tag{2.33}$$

The covariant derivative in equation 2.32 is the one of $\mathrm{SU}(2)_{\mathrm{L}} \otimes \mathrm{U}(1)_{\mathrm{Y}}$ given by equation 2.27 and represents the kinetic term. The Higgs potential is similar to the one considered first and has also two solutions depending on the sign of μ^2, but only the negative solution is shown here. There is an infinite set of degenerated states with minimum energy:

$$\phi_0 = \sqrt{\frac{1}{2}}\begin{pmatrix} 0 \\ v \end{pmatrix} \text{ with } \mathrm{v} = \sqrt{\frac{-\mu^2}{\lambda}} > 0. \tag{2.34}$$

The field Φ is expanding around its minima using a new field $h(x)$, which describes quantum fluctuations. Moreover, three massless Goldstone fields $\theta^i(x)$ are included:

$$\Phi(x) = e^{i\frac{\sigma_i}{2}\theta^i(x)}\frac{1}{\sqrt{2}}\begin{pmatrix} 0 \\ v + h(x) \end{pmatrix}. \tag{2.35}$$

By choosing a particular gauge field, the Goldstone fields are absorbed into the physical field defined by $\mathrm{SU}(2)_{\mathrm{L}} \otimes \mathrm{U}(1)_{\mathrm{Y}}$. The absorption of the massless Goldstone bosons leads to the apparition of a mass term in equation 2.32. The mass generation mechanism is explained in the following. The new field injected in equation 2.32 modifies the derivative covariant. By omitting any terms containing h and by removing the partial derivative:

$$\left|\left(i\frac{g}{2}\mathbf{W}_{\mu} + i\frac{g'}{2}Y\mathbf{B}_{\mu}\right)\Phi\right|^2 = \frac{1}{8}\left|\begin{pmatrix} gW^3_{\mu} + g'B_{\mu} & g(W^1_{\mu} - iW^2_{\mu}) \\ g(W^1_{\mu} + iW^2_{\mu}) & -gW^3_{\mu} + g'B_{\mu} \end{pmatrix}\begin{pmatrix} 0 \\ v \end{pmatrix}\right|^2. \tag{2.36}$$

The charged fields can be expressed as a linear combination of gauge fields:

$$W^{\pm}_{\mu} = \frac{W^1_{\mu} \mp iW^2_{\mu}}{\sqrt{2}}. \tag{2.37}$$

The eigenstates are rewritten as decorrelated terms representing the neutral fields from the EW symmetry group:

$$Z_\mu = \cos\theta_w W_\mu^3 - \sin\theta_w B_\mu, \tag{2.38}$$

$$A_\mu = \sin\theta_w W_\mu^3 + \cos\theta_w B_\mu, \tag{2.39}$$

with θ_w the Weinberg angle, which represents a bound between the couplings g and g':

$$\sin\theta_w = \frac{g'}{\sqrt{g^2 + g'^2}} \; and \; \cos\theta_w = \frac{g}{\sqrt{g^2 + g'^2}}. \tag{2.40}$$

Equation 2.36 becomes:

$$\begin{aligned} \left|\left(i\tfrac{g}{2}\mathbf{W}_\mu + i\tfrac{g'}{2}Y\mathbf{B}_\mu\right)\Phi\right|^2 &= \tfrac{1}{8}\left|\begin{pmatrix} A_\mu\sqrt{g^2+g'^2} & gW_\mu^- \\ gW_\mu^+ & -Z_\mu\sqrt{g^2+g'^2} \end{pmatrix}\right|^2 \\ &= \tfrac{1}{2}M_Z^2 ZZ^* + \tfrac{1}{2}M_W^2 W^-W^+ \end{aligned} \tag{2.41}$$

With $M_Z = \frac{1}{2}v\sqrt{g^2 + g'^2}$ and $M_W = \frac{1}{2}vg$, the mass of the Z boson and the W$^\pm$ bosons. The mass of the photon is consistent with the expectation and is null.

The Higgs mechanism implies the existence of a massive gauge field, the Higgs boson. It is coupled to the other bosons and also to itself. This could be shown by extending the Higgs potential with the field defined in equation 2.35:

$$-\lambda v^2 h^2 - \lambda v h^3 - \frac{1}{4}\lambda h^4 \tag{2.42}$$

The first term gives the mass of the Higgs boson, $M_H^2 = 2\lambda v^2$, while the second and third terms are the Higgs self-interactions. The Higgs mass can not be predicted by the theory because it is given by a function of the parameter λ, which is one of the free parameters of the SM.

Yukawa couplings with fermions

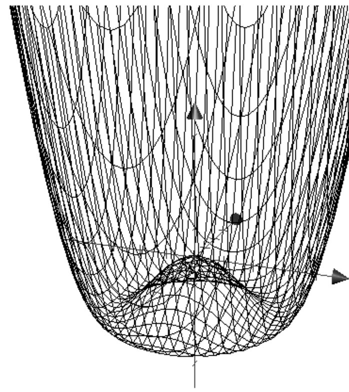

Figure 2.2 – Higgs potential $V(\phi)$ for $\mu^2 < 0$.

2.3 Beyond the Standard Model

The SM constitutes one of the most successful achievements in modern physics. One of its strength is to provide an elegant theoretical framework to describe the known experimental facts about particles, but it also predicts the existence of a mechanism to generate the particle masses via the Higgs mechanism. Nevertheless, this theory does not solved all the questions about the Universe.

Add plots to confirm the good SM predictions.

2.3.1 Limitations of the Standard Model

In the following, the limitations of the SM are described.

Free parameters

Up to 19 free parameters are used in the SM and this theory does not explain their existence. Even if it is not as major problem for the physics itself, the particle physics community has a lack of understanding and explaining these values. These free parameters are:

- the masses of the nine fermions,

- the coupling constants g and g' of respectively the $U(1)$ and $SU(2)$ groups,
- the coupling constant of the strong interaction α_s,
- the three mixing angles, as well as the CP-violating phase of the CKM matrix,
- the Higgs boson mass and the expected vacuum value for the Higgs field *vev*,
- $\theta_{\mathrm{CP}}^{\mathrm{QCD}}$, a parameter that allows the CP violation in QCD.

To this 19 free parameters, 7 other parameters can be considered, thus increasing the number of parameters to 26. This parameters are the masses of the three neutrinos, as well as the four parameters of the *Pontecovro-Maki-Nakagawa-Sakata* matrix[3].

Hierarchy problem

The hierarchy problem refers to two main energy scales problem of the SM.

First of all, the difference between the energy scale of the SM and the Planck scale is of seventeen orders of magnitude. No "intermediate" physics has been found between the two scales.

A second problem occurs while considering the Higgs boson mass. The SM does not predict its mass, but it sets some theoretical bounds with respect to Λ, the energy scale at which the SM is not valid anymore. The theoretical Higgs boson mass is higher than what it should be compared to the EW scale. The Higgs boson interacts with the particles of the SM (fermions, W and Z boson), but it also interacts with itself. Due to the scalar nature of the boson, there are quartic divergences while calculating the loop corrections. The quantum corrections, which take into account the coupling of the Higgs boson, are Λ^2 divergent and lead to a huge Higgs boson mass. To avoid that, delicate cancellations should occur between the quantum corrections. These cancellations are known as the fine-tuning problem.

[3] equivalent of the CKM matrix for the neutrinos' mass

Gravitation

Although particle physicists are dreaming of a "theory of everything" that will unify the electroweak, strong and gravitational interactions, there is no viable theory to describe the gravity in a quantum point of view to include it in the SM and which would be still valid at a macroscopic scale.

Neutrino mass

The neutrinos defined by the SM are assumed to be exactly massless. Nevertheless at the end of the year 1990, the Super Kamiokande experiment had surprising results [33]. The measured flux of solar and atmosphere neutrons was lower than expected. The result was interpreted by an oscillation of neutrinos between the three leptonic flavors. However, the oscillation is possible only if the neutrino has a mass. That phenomenon could be considered as a proof of physics beyond the SM.

Matter-antimatter asymmetry

As discussed at the beginning of this chapter, the SM defines an equal number types of particles and anti-particles. In the case of the Big Bang theory, it is assumed that the matter and antimatter were created in an exactly equal amount. However, if the amount of matter and antimatter was equal, the Universe would have been completely annihilated. A mechanism has favoured electrons, protons and neutrons with respect to positrons, antiprotrons and antineutrons. The asymmetry between the matter and antimatter proportion could come from a smaller production of antimatter compared to the matter during the Big Bang. The matter and antimatter have annihilated, but a part of matter has survived.

The study of the kaon oscillation has shown that this particle is able to transform spontaneously to its own antiparticle and vice-versa. Nevertheless, this transformation is not symmetric: the kaon is slower to turn into an antikaon than the inverse transformation.

Dark Matter and dark energy

Several astrophysical observations are indicating that the Universe is made not only of visible matter but also of matter that seems to be invisible to the electromagnetic interaction and is called the dark matter. In 1933, a measurement of the galaxies velocities in the Coma cluster to determine the cluster mass gives a surprising result. The mass was more than two orders of magnitude bigger than the mass of visible stars in the cluster. It was found that the matter of the SM describes only 5 % of the Universe content. The rest of the Universe is made of 22 % of dark matter and around 73 % of dark energy. The neutrinos are possible candidates to dark matter, as they couple to SM matter only via weak interaction, but they cannot account for the entire density of the universe. Nowadays only twelve particles (plus the anti-particles associated) have been observed.

2.3.2 Theories beyond the Standard Model

Supersymmetry

The Supersymmetry (SUSY) is a QFT, that relates the elementary fermions known to corresponding bosons, called sfermions and the bosons to corresponding fermions, called sbosons [66]. The new particles introduced are called super-partners. They have the same mass, the same quantum numbers but the spin is differing by a half factor. SUSY is a broken symmetry. This will allow the super-particles to acquire very high masses.

SUSY is a good candidate for physics beyond the SM, as it could solve the hierarchy problem without any fine tuning. For example, the loop contributions of one particle to the Higgs are cancelled by the loop contributions of its super-partner. It would be able to provide a framework for the unification of the three gauge interactions at a GUT scale. The lightest super-particle is a good candidate for the Dark Matter.

Despite it will answer many questions from the SM, there is a lack of understanding why SUSY is a broken symmetry.

Grand unification theory

After the success of the electroweak unification, the next step is to include the strong interaction to build the Great Unification Theory (GUT), an extension of the SM. In this framework, the three forces are different manifestations of a single interaction. It includes the $\mathrm{SU(3)_C}\otimes\mathrm{SU(2)_L}\otimes\mathrm{U(1)_Y}$ symmetry group into a larger SU(5) group. The quarks and leptons are ordered in left-handed decuplets and right-handed quintets. The coupling constants are described by only one parameter. There are 24 mediators, the 12 mediators of the SM plus 6 X mediators (charge $\pm 4/3$ and 3 colors) and 6 Y mediators (charge

$\pm 1/3$ and 3 colors). It predicts the existence of new particles as leptoquarks[4], multiple Higgs bosons and new currents.

Unfortunately, the theory is not validated because of its prediction of the proton lifetime. The first GUT was introduced by Georgi and Glashow in 1974 and predicted the decay of the proton [36]. The actual experimental limit of the proton lifetime is of 5×10^{32} years, whereas the predicted lifetime defined by the SU(5) group is one order of magnitude lower [60].

Technicolor

The technicolor is a theory that explains the mass generation. Contrary to the EW symmetry, the masses of particles are not generated by the spontaneous symmetry breaking but they are generated by a strong gauge interaction. This interaction is strong and confined at the energy that has been experimentally probed. The approach of the theory avoids the hierarchy problem induced by the SM.

String theory

The particle physicists have the dream of unifying the forces of the nature to have only one single interaction with four different manifestations. The string theory proposes a framework for the "theory of everything". The basic unit of matter is no more considered as particles but one-dimensional strings of which particles are various vibrational modes.

The string theory is a theory of quantum gravity. It tries to unify the gravitation to the quantum Extra dimensions of $10 - 11$ space-time dimensions. Possible explanation for the hierarchy problem.

2.4 Conclusions

Along this chapter, the successes and limits of the SM were discussed. The high energy physics community is trying to study as far as possible the limit of the SM and is also trying to find some proof of new physics beyond the SM. The LHC at CERN has permitted in 2012 to point out the existence of a Higgs boson. Nevertheless, the beam structure of the LHC is not efficient enough to perform very precise measurements. Because of the collision between

[4] Coupling between a lepton and a quark

protons, the energy of the collision can't be exactly known. The next chapter deals with a future experiment in high energy physics, where electrons and positrons are used to probe the matter instead of protons and anti-protons.

Chapter 3

Towards a linear future: the International Linear Collider

Since 2008, the LHC is the most powerful tool in high-energy physics. It will provide a better understanding of the universe, particularly with the discovery in 2012 of a new particle compatible with the Higgs boson responsible for the spontaneous symmetry breaking of the Standard Model (SM) [15, 16]. Although the LHC is an impressive machine able to collide protons at a centre-of-mass energy of 13 TeV, the complex environment of the events makes more difficult to access some fundamental parameters. To test the validity of the SM and other physics theories introduced in chapter 2, the high-energy physics community has converged on the necessity to build a linear electron-positron collider.

This chapter will explain the motivations to invest into a new global project. It will present the complementary nature of the lepton and hadron colliders and the main advantages of lepton collisions will be discussed. After giving an overview of the ILC with its basic design and the detector models, we will focus on the design of one of the detectors: the ILD.

Contents

3.1 Towards a linear electron collider

The most impressive accelerator ever built is located at Centre Européen pour la Recherche Nucléaire (CERN) in Geneva, Switzerland. It is the world's largest particle accelerator, with a circumference of nearly 27 kilometers, straddling the Swiss and French border. It is designed to collide two beams of protons or heavy ions, with the possibility to reach centre-of-mass energies of 13 TeV with a peak luminosity of 10^{34} cm^2.s^{-1}. The goals of the LHC are to perform tests of the SM and to search for new forces and/or particles. The collider covers a wide energy range at the constituent level while running at a fixed beam energy. Nevertheless, the particles used for the collision are not elementary ones, thus, the measurements are impacted by the hadronic background produced.

A machine dedicated to precision measurements, complementary to the LHC, would bring very valuable to the physics community. The advantages of linear electron collider will be presented in the following.

3.1.1 Advantages of a linear lepton collider

First of all, in a hadron collider because of the compositeness of the particles used, only a part of the total centre-of-mass energy is used during each collision. The four-vector momentum of the interacting particles is not known because of the unknown number of partons part of the interaction. By colliding leptons, which are structureless objects, the full centre-of-mass energy is available for the elementary process. The initial four-vector momentum of an interaction is exactly known, hence the event is fully reconstructed.

Secondly, with a lepton collider, the beam energy is tunable and both electron and positron beams can be polarised. The spin of the initial state is known. The selection of an appropriate polarisation can enhance the signal and suppress the background.

Thirdly, the proton-proton interaction cross section is dominated by inelastic background QCD processes. The signal event is then accompanied by large backgrounds produced by the bunches interaction. This background masks the elementary process of interests, such that it has an impact on the detector design, that should have a high radiation tolerance and implement a selective trigger to reduce the data rate. The lepton colliders do not suffer from this kind of background and at similar energies, the event rate is lower than those at hadron colliders. Moreover, the interaction of electrons and positrons is purely electroweak. In consequence, the detector does not have to handle extreme data rates and can be used without any trigger. Hence, the sensitivity to any possible signature of new physics is improved. REPHRASE EVERYTHING

Although the electron and positron, have clear advantages over hadrons to perform precise measurements, the choice of a linear collider over a circular one comes from the physics of accelerating charged particles. When charged particles move in a circular accelerator, they lose some energy by emitting photons via synchrotron radiation. Equation 3.1 describes this energy loss:

$$\Delta E_{\mathrm{sync}} \sim \frac{E^4}{m^4 r}. \tag{3.1}$$

The radiative energy loss ΔE_{sync} is inversely proportional to the radius r of accelerator, the energy of the particle E to the power of the fourth and its mass m to the power of the fourth. As the electron mass is $\sim 1.8 \times 10^3$ smaller than the proton mass, the energy loss radiated by the electron is much higher than the energy loss radiated by proton at the same centre-of-mass energy. To compensate the energy loss, a circular electron-positron accelerator should have an extremely large radius (larger than the actual LHC), increasing the cost to build the experiment. Another solution to overcome the synchrotron radiation is to accelerate the particles in a linear collider. The centre-of-mass energy has to be reached only passing once through the accelerator, whereas a bunch of particles in a circular collider is accelerated many times until the desired energy of collision is reached. The choice of a linear collider over a circular one comes also from the cost, which has a quadratic energy dependence for a circular one, whereas it follows a first power energy for a linear one [63]. To work at the same energy scale, a linear collider would require a bigger number of accelerating cavities and would make a much bigger and more expensive collider than a circular one.

3.1.2 Future linear lepton collider

Since the 1980's, several linear collider technologies have been developed, leading in the 1990's to five major accelerator technologies: Superconducting Radio-Frequency (SRF), the Compact LInear Collider (CLIC) technology and three different normal conducting technologies (S-band, C-band, and X-band) [23]. Different projects are under studied for the next high-energy physics experiment. All the projects aim to perform precise measurements. CERN is preparing a electron/positron linear collider, called CLIC. It has a challenging technology to aim a nominal energy of 3 TeV. The accelerator will use radio-frequency structures and a two beam concept [14]. Another idea would be to develop a muon collider instead of electron-positron collider [53]. As the electron, the muon is a pointlike particle, therefore the centre-of-mass energy can be easily adjusted to perform a precise study. The muon mass is 207 times larger than the electron mass, which means that a muon beam would suffer less energy loss by synchrotron radiation. Hence, a muon circular collider could be feasible. However, the muon has a lifetime of only 2.2 μs making up a more challenging acceleration design.

At the beginning of the 2000's, the International Committee for Future Accelerators (ICFA) was formed and has chosen in 2004 the SRF technology [40] to build the ILC [41]. The technology developed for this future experiment is also used for the XFEL at Deutsches Elektronen-Synchrotron (DESY) in Hamburg and at KEK in Japan.

The CLIC and muon colliders will not be described further in this thesis.

3.2 The ILC machine

The ILC should be the next lepton collider experiment and will be situated in Japan. In 2016, the physics community was waiting for an official decision of the Japan government concerning the final experimental site. At the time when this thesis was written, the scientific community has chosen a site candidate in the north of Japan, in the region of Kitakami.

Reference to the decision but which one?

3.2.1 Baseline design

The ILC is planned to collide electrons and positrons at the center-of-mass energies varying between 250 GeV and 500 GeV for 31 kilometers long accelerator. An upgrade to reach the centre-of-mass energy of 1 TeV is possible, but the accelerator will have to be extended to achieve a total length of

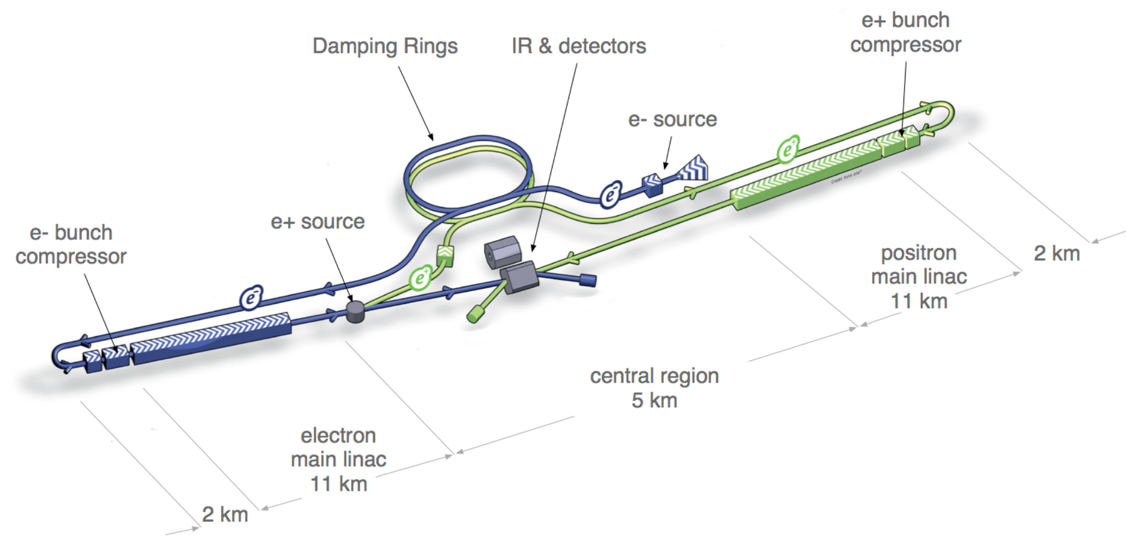

Figure 3.1 – Schematic layout of the International Linear Collider (ILC) [8].

50 kilometers. It is designed to generate a total of 500 fb^{-1} of data during the first four years of operation. The luminosity will reach a peak of 2×10^{34} $\mathrm{cm}^{-2}.\mathrm{s}^{-1}$ at $\sqrt{s} = 500$ GeV.

The main components of the ILC are presented in the following order. An overview of the electron source and their acceleration via the conducting and superconducting structures is presented, then the role of the damping rings, the injection into the main linacs, followed by the positron source and the Beam Delivery System (BDS) are described. Finally, the interaction region (IR) is presented. A detailed description of the ILC can be found in the Technical Design Report [3].

3.2.2 Machine design and beam parameters

Polarised electrons are produced by a laser firing into strained GaAs photocathode in a Direct-current (DC) gun. To implement a redundancy, the electron generation system is made of two lasers and DC guns, providing bunches with a polarisation of 90 %. The electrons are then pre-accelerated to 76 MeV using non-superconducting accelerating structures. They are then injected into a 250 m long superconducting linac to reach the energy of 5 GeV. The dimension and density of the bunches are quite extended, thus their emittance is too wide. Before injecting the bunches into a damping ring, which is used to decrease the emittance and reach the desired luminosity, superconducting solenoids rotate the spin vector into the vertical direction, while SRF cryomodules are used for an energy compression.

The damping ring has a 6.7 km circumference and is made of magnets and wrigglers that are going to force the particles to get a bent track. This system is used to dump the electrons with large transverse and longitudinal emittance to the low emittance required for the luminosity production. The reduction of the emittance should be achieved within 200 ms between the machine pulses. Although the positron source was not yet introduced, their bunches suffer from the same problems as the electron ones. A second damping ring, placed in the same cavern as the electron one, is also in charge to get the desired emittance.

The bunches are then extracted from the damping rings and transferred via the Ring To the Main Linac (RTML) structure, the longest continuous beam line at the ILC. It is divided into five subsystems to transport the bunches from the damping rings to the BDS. It is orienting the beam into the desired polarisation by rotating the spin of the particle. The beam bunch length is compressed from several millimeters to a few hundred by using a two-stage bunch compressor. While the bunches are compressed, sections of SRF technology accelerate the bunches from 5 GeV up to 15 GeV. One of the challenges of the RTML is to preserve the emittance obtained after the damping rings, while the length and the energy of the bunches are tuned. Then, the particles are delivered to the main linac, an 11 km long accelerator using 1.3 GHz SRF cavities, made of niobium.

What are the others made of?

Before reaching the interaction region, the primary electron beam is transported through a 147 m superconducting helical undulator to produce photons from $\sim$ 10 up to $\sim$ 30 MeV, depending on the energy of the primary beam. This primary beam is separated from the photons and sent back to the BDS with an energy loss of $\sim$ 3 GeV. The photons are directed onto a rotating Ti-alloy target to create e^+e^- pairs that are separated. The positrons collected are accelerated to 125 MeV using a normal conducting linac and then accelerated to 5 GeV with a superconducting boost linac. Finally, they are injected into the damping ring to reduce their emittance.

The two beams are transported from the high energy linacs to the IR by the BDS, in charge to focus the beams to the sizes required to meet the desired luminosity. It is divided into five main subsystems. In the direction of the beam, a system is in charge to perform some emittance measurement and matching, to give a trajectory feedback, and provide a polarimetry and energy diagnostic. Then, the beam is collimated to remove the beam-halo particles that would generate a huge amount of background in the detector. Muons generated during the collimation process are deflected by magnetised iron shielding. Thereafter, strong compact quadrupoles focus the beam to the sizes required to meet the desired luminosity. Before the collisions, crab cavities rotate the bunches in the horizontal plane for effective collisions and to achieve a 14 mrad total crossing angle. After the collisions, an extraction line is dedicated to transport the beams into the main beam dump.

Although two experiments will run at the ILC, there will be only one interaction region due to cost reasons. To have two experiments running at the same time, it requires two separate BDS of 4 km long each. Thanks to a push-pull scheme, the detectors will work alternatively: while one is taking data, the other one is sitting in the garage for maintenance. The two detectors will be presented in more details in section 3.3.

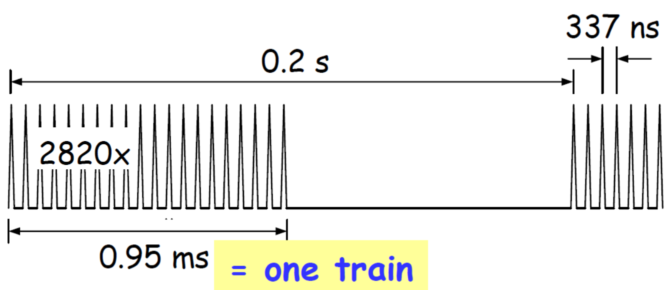

Figure 3.2 – Schematic view of the bunch structure at the ILC. One bunch train is made of 2625 bunches and lasts 0.95 ms. Each bunch crossing is spaced out by 337 ns. Two bunch trains are 0.2 s apart from each other [52].

The accelerator described above will create bunch trains at a repetition rate of 5 Hz. Each train is composed of 2625 bunches that contain 2×10^{10} particles and lasts 0.95 ms. The interval between two trains is 2 ms long. This structure is a key feature to develop detectors able to be switched off during the dead time in order to reduce the power consumption.

Write TDR values, see Marcel's talk

3.2.3 Beam backgrounds

To design the detectors of the ILC, the backgrounds must be understood and taken into account to give optimal performances. The event reconstruction becomes more complicated with hits caused by background particles. Their are two kinds of background, the one created by the BDS and the one related to the interaction point. As it was discussed in subsection 3.2.2, the collimator placed closed to the interaction point (IP) to remove the beam halo, that can produce muons by an electromagnetic shower. To sweep them away, iron spoilers are used to create a magnetic field and deflect the muons. A side effect is to increase the number of neutrons created in photo-nuclear reactions. A concrete wall placed at the entrance of the experimental hall vanishes the neutron background.

Contrary to the LHC, the ILC will not suffer from QCD background, as mentioned in section 3.1.1. Nevertheless, due to the nature of electrons and positrons, the two beams will interact each other before they collide. The electromagnetic beam field of each bunch is high and causes the focusing of the opposite bunch. It is bending the electron/positron trajectories near the IP. On the one hand, this effect helps to focus the incoming beams and enhance the luminosity. On the other hand, as the charged particles have bending track, they are emitting hard photons via beamstrahlung, creating e^+e^- pairs background. The hard photon is strongly focused in the forward region and do not contribute strongly to the background in the detector. However, the e^+e^- pairs created contribute to the background directly or through backscattered particles. In consequence of the beamstrahlung, the beam particle energy is reduced, hence the collisions occur at different energies from the nominal one and this affects the physics cross-section. The beamstrahlung photons can also produce neutrons by hitting components. The other source of hard photons is the initial state radiation. With the beamstrahlung, they contribute reducing the luminosity [55].

Peak luminosity may-be?!

Different kinds of soft pairs background can be expected at the ILC: the coherent and incoherent pair production. The coherent pair production appears when beamstrahlung photons are interacting with the strong electromagnetic field of the beams. In the ILC environment the coherent pair background are negligible, whereas the incoherent pair production is dominant. It corresponds to e^+e^- pairs created by the interaction of only two particles. They are to the number of three depending on the nature of the scattered photons creating the e^+e^- pair. The Bethe-Heitler process corresponds to the scattering of one real photon while the second one is virtual. It contributes to approximately two of the third pair production. The second process is the Landau-Lifshitz, where the two scattered photons are virtuals and contribute to approximately to a third of the pair creation.The last production occurred via two real photons (Breit-Wheeler process) and contribute only to a percent level. The incoherent e^+e^- pairs are produced at a relatively low transverse momentum and are emitted in the forward direction.

Sentence not clear

3.3 The ILC detectors concept

3.3.1 Overview of the two experiments

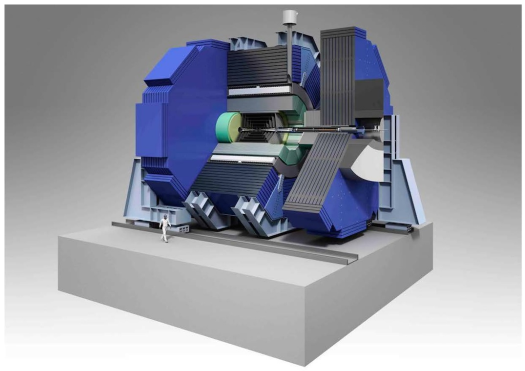

(a) The Silicon Detector

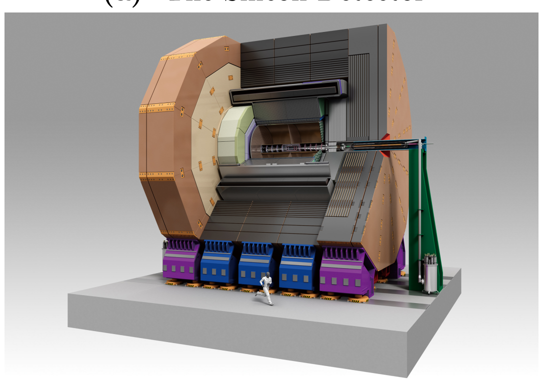

(b) The International Large Detector

Figure 3.3 – Overview of the two detectors designs at the ILC. Fgure (a) represents the SiD design while figure (b) shows the ILD approach [9].

As it was presented in section 3.2.2, the ILC will be built with only one interaction region due to cost reasons, whereas two detectors are foreseen. The push-pull operation scheme will allow for data taking of one detector, while the second one is out of the beam in a close-by cavern for maintenance. The interval to switch the detectors should be short enough and of the order of one day. This time efficient implementation sets specific requirements for the beam structure but also for the detector design. The detectors should be placed on platforms to preserve the alignment and to distribute the load equally onto the floor. Another requirement on the detector design is that the magnetic fields outside the iron return yokes must be small enough to not disturb the second detector on the parking position. It is assumed that a limit of 5 mT at a lateral distance from the beam line should be sufficient.

The motivation to build two detectors with a different approach is mainly to provide a cross-check and a confirmation of results and complementary strengths. Both detectors are optimised to study a broad range of precision measurements and search of new physics drove by the ILC expectations. Their performances are driven by the Particle Flow Algorithm (PFA) to be able to measure the final states of events with a high accuracy. To do so, both detectors should have a high hermeticity, high granularity calorimeters and excellent tracking and vertexing. The PFA is shortly presented on subsection 3.3.2.

The Silicon Detector (SiD) is a compact detector made of a silicon tracking and 5 T magnetic field. The tracking system provides robust performance thanks to the time-stamping on single bunch crossings. The calorimeters are highly granular to perform the PFA.

The second detector is ILD. In contrast to the SiD, the tracking system is based on a continuous readout Time-Projection-Chamber (TPC) surrounded by silicon tracking detectors. The magnetic field will be only of 3.5 T combined with granular calorimeters for a good particle-flow reconstruction

3.3.2 Particle flow algorithm

The main purpose of the ILC (or the CLIC) is to achieve precise measurements of physics processes that produce final states with multiple jets. The jet energy resolution at the ILC should be sufficient to cleanly separate W and Z hadronic decays. Typically, the jet energy resolution is deduced from equation 3.2, where α is the stochastic term usually greater than $\sim 60\ \%/\sqrt{E(\mathrm{GeV})}$.

$$\frac{\sigma_E}{E} \simeq \frac{\alpha}{\sqrt{E(GeV)}} \oplus \beta. \tag{3.2}$$

The PFA approach is the extended version of the Energy Flow approach (used at H1, D0, CMS) for a highly granular detector. The goal of this framework is to achieve a stochastic term for the energy resolution greater than $30\ \%/\sqrt{E(\mathrm{GeV})}$, not reachable with a traditional calorimeter. Each sub-detector should be efficient enough to separate and to reconstruct the four-vectors of all visible particles in an event. The energy of charged particle is measured in the tracking detectors, while the energy measurements for photons are done in the electromagnetic calorimeter and neutral hadrons are done in the hadron calorimeter.

Why better? 60 % tracks

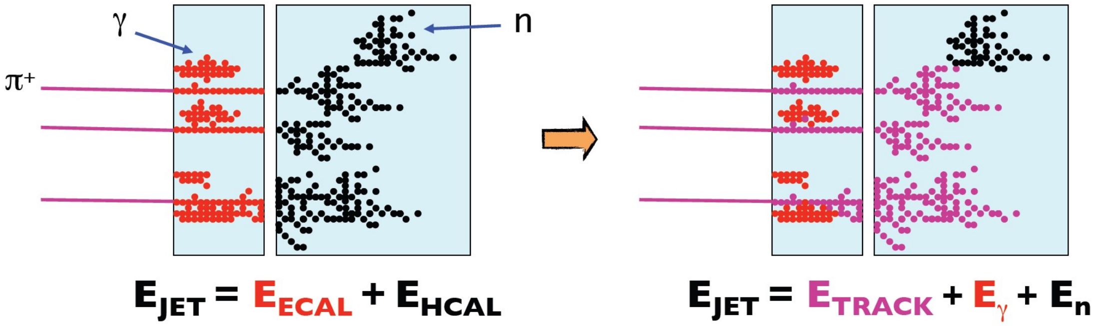

Figure 3.4 – Two different approaches for calorimetry. On the left is the traditional calorimetry method used on most of the experiments, the right one is the particle flow approach for calorimetry. The particle track is taken into account to calculate the jet energy [37].

The PFA requirements drive the design of the detectors at the ILC. For both experiments, the electromagnetic and hadronic calorimeter have to be located inside the solenoid. Moreover, each sub-detector must be able to distinguish single particle signals, imposing a better tracking precision and higher granular calorimeters than the traditional detectors in high energy physics.

3.3.3 The ILD detector

The design of ILD follows the requirements for optimal PFA performance. In summary, the detector should be highly granular to have a robust three-dimensional imaging capability. It will combine a high-precision Vertex Detector (VXD) system, a hybrid tracking system and calorimeters inside a 3.5 T solenoid. On the outside, a coil and iron return yoke will be instrumented as a muon system and a tail catcher. The figure 3.5 represents the different parts of the detector.

The ILD system coordinate is as following: the Cartesian coordinate system, where x and y are the horizontal and vertical coordiantes respectively, in the plane transverse to the beam line, while z is along the beam line. For the spherical coordinate system, r is the distance from the beam line, θ the

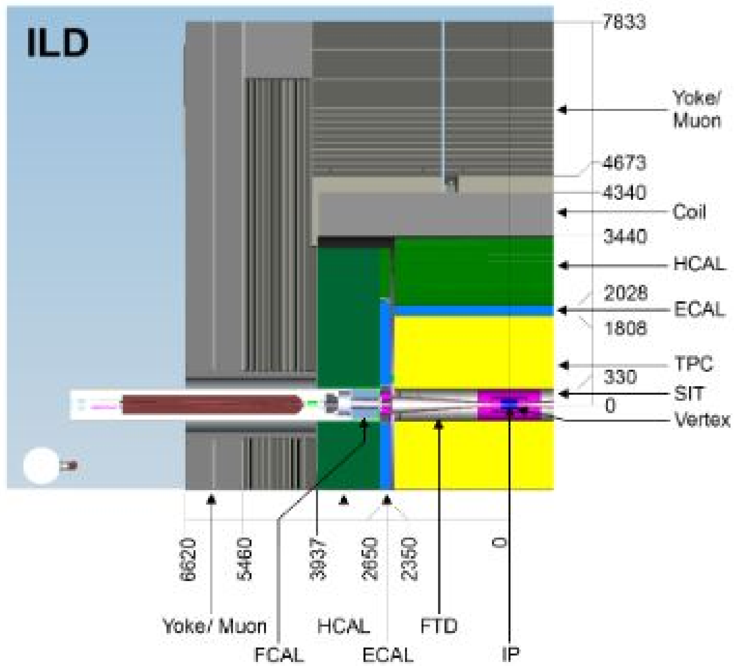

Figure 3.5 – Quadrant view of the ILD detector concept with its subdetector system [9].

track polar angle and ϕ the azimuthal angle. The third coordinate system is the cylindrical one. In this system, r is the distance from the beam line, ϕ the azimuthal angle and z the coordinate along the beam line.

Vertex detector

The VXD is the closest detector to the interaction region and is in charge to measure particles' tracks and to reconstruct the decay vertices of the particles. For the moment, two vertex detector design are under study, but both of them have a pure barrel geometry. One geometry is made of five single sided layers, whereas the other one has three double-sided detection layers. Chapter 5 will introduce in more details the vertex detector requirements for the ILD, such as the material budget and the measurements precision aimed. The different design proposals will be presented.

Tracking

The main tracking system for the ILD is performed by the TPC. It is a gaseous detector with a low material budget designed to measure the particles' trajectory. When a particle traverses through the TPC, it ionises the gas, creating electrons that are drifting to the anode thanks to a high voltage. The anode is the part where the readout plates are installed. It provides a 3D position of the particles tracks thanks to the wires and the anode (give x-y) and the z coordinate is given by the drifting time. In addition to the exact position measurement, this detector is also able to measure the energy $\frac{dE}{dx}$ deposited by the particle, which can be used for particle identification.

The requirements to design a TPC at the ILC are given by two main values:

- The single point resolution $\sigma_{s.p.}$ which should be lower than 100 μm in the $r\phi$ direction and less than 500 μm in the z direction;
- The minimum distance to separate two hits which should be lower than 2 mm.

The TPC envisioned for ILD is constituted of a central barrel part, with an inner radius of $\simeq$ 33 cm and a outer radius of $\simeq$ 180 cm and two endcaps with a detection area of 10 m^2. The solid angle coverage is up to $|\cos\theta \simeq 0.98|$. The barrel will be filled with a gas mixture called T2K (3 % of Ar-CF4 and 2 % of isobutane). Due to the low material budget and the ability to cope with a high magnetic field, the TPC is compliant with the PFA (see subsection 3.3.2).

To improve the track reconstruction, the TPC is surrounded by highly granular silicon detectors: two barrel components, the Silicon Internal Tracker (SIT) and the Silicon External Tracking (SET); an end-cap component, the End-cap Tracking Detector (ETD) and the Forward Tracking Detector (FTD). The SIT provides tracking between the VXD and the TPC, whereas the SET is giving an entry point to the Electromagnetic CALorimeter (ECAL) after the TPC. Both systems provide precise space points and improve the overall momentum resolution. The goal of the SIT is to improve the momentum resolution, the reconstruction of low p_T charged particles and the reconstruction of long-lived particles. The coupling of the SIT and SET provide also a time-stamping information.

The ETD is located within the gap separating the TPC and the endcap calorimeter. It improves the momentum resolution for charged tracks with a reduced path in the TPC. It also reduces the effect of the material of the TPC end-plate. The material budget of this end-plate is estimated to 15 % of X_0.

As the TPC does not provide any coverage in the forward region, seven silicon disks ensure efficient and precise tracking down to very small angles, whereas the ETD and the FTD make sure to get a full tracking hermeticity.

To simplify the system layout and the maintenance, the SIT, SET and ETD are made of single-sided strip layers tilted by a small angle with respect to each other. They are placed in a so-called false double-sided layers. The SIT has two layers of microstrip, instead of one layer for the SET. The technology studied are microstrip sensors with an area of 10×10 cm^2, with a pitch of 50 μm, a thickness of 200 μm and an edgeless. The dead area of the sensors will be reduced down to few microns instead of 100 μm. The spatial point resolution aimed for this detectors is $\sim$ 7.0 μm in the $r\phi$ direction. The table 3.1 gives the single point resolution aimed, as well as the angular coverage and the material budget.

Detector	Single point resolution (μm)	Coverage	Material budget X_0 (%) / layer
SIT	$\sigma_{R-\phi} = 7.0$ $\sigma_Z = 50.0$	$\cos\theta \sim 0.91$	0.65
SET	$\sigma_R = 7.0$	$\cos\theta \sim 0.79$	0.65
ETD	$\sigma_X = 7.0$	$\cos\theta \sim 0.799 - 0.985$	0.65

Table 3.1 – Parameters aimed for the silicon tracker using micro-strips sensors.

The FTD is placed in the forward direction, between the beam pipe and the inner field cage of the TPC, where the magnetic field becomes less and less useful to bend charged tracks and so the determination of a precise momentum is more difficult. It consists of seven tracking disks: the two firsts are pixel detectors to cope with expected high occupancies and the five others are strip detectors. The pointing resolution will vary between $3.0 - 6.0$ μm for the two first layers and 7.0 μm for the five other ones.

Check the table and values....

Calorimeters

The calorimeters design is driven by the particle flow requirements. Each particle must be reconstructed individually in the detector with a jet energy measurement equal to:

$$\frac{\Delta E}{E} = 30\ \%/\sqrt{\frac{E}{GeV}}. \tag{3.3}$$

The energy resolution obtained in equation 3.3 is obtained thanks to a combination of information from the tracking system and the calorimeters. The choice of technology used for the calorimeter will be determined by the pattern recognition performance. One of the ILD detector's goal is, for example, to be able to get a jet energy resolution sufficient to clean separate W and Z hadronic decays.

The average jet energy distribution is roughly:

- 62 % are charged particles (mainly hadrons)
- 27 % are γ
- 10 % are long-lived neutral hadrons
- 1.5 % are ν

The ECAL is the first calorimeter right after the tracking system. Its role is to identify photons and leptons and measure their energy, nevertheless, it is also the first section to develop the hadron showers. The fine segmentation makes an important contribution to hadron-hadron jet separation. For the ILD, a compromise between the performance and the cost has led to use a sampling calorimeter realised with tungsten absorber. They are three options under study for the active area. The first one called SiW-ECAL, is made of silicon pin diodes with a pitch of 5×5 mm^2. It has the advantage to cover a large area, to be reliable and simple to operate, to have thin readout layers and can be operated in 3.5 T magnetic field. The second option is made of scintillator strips readout by photo-sensors and is called ScECAL. It has an active area of 5×45 mm^2 arranged in alternative directions to achieve an effective granularity of 5×5 mm^2 The weakness of this technology happened in dense jets environment, where the reconstruction becomes more and more complicated.Some alternatives are also thought, like the Micromegas chambers. Nevertheless, this technology is less advanced compared to the others. One other good candidate could be the use of Monolithic Active Pixel Sensor (MAPS) sensors. They have the advantage to get the signal sensing and processing on the same substrate and by choosing standard CMOS processes, the cost of fabrication would be reduced. ???

The HAdronic CALorimeter (HCAL) has the role to separate the deposits energy of charged and neutral hadrons and to precisely measure the energy deposited. It is also a sampling calorimeter using stainless steel instead of tungsten as an absorber. The rigidity of stainless steel makes possible to get a self-supporting structure limiting the dead areas. Two baseline technologies for the active medium area are studied. The Analogue HCAL (AHCAL) is made of scintillator tiles, whereas the semi-digital, called Glass Resistive Plate Chamber (GRPC), is based on the Semi-Digital HCAL (SDHCAL).

In order to monitor the luminosity and the beamstrahlung, the calorimeter system is completed in the very forward region by three different subsystems covering very small angles also for neutral hadrons: the LumiCal, the BeamCAL, and the Low angle Hadron CALorimeter (LHCAL). The LumiCAL is placed in a circular hole of the end-cap ECAL and covers polar angles between 31 and 77 mrad. It serves as luminosity monitor by measuring the Bhabha scattering $e^+e^- \rightarrow e^+e^-$ via emission of virtual γ. The luminosity $\mathcal{L}$ is determined by measuring the ratio of the number of counted events N_B in a considered polar angle ranged and the integral of the differential cross-section σ_B in the same region. The measurement precision should be better than 10^{-3} at 500 GeV. After each bunch crossing, the beamstrahlung pairs hit the BeamCal. This would permit to get an estimation of the bunch-by-bunch luminosity, but also to determine the beam parameters. It is placed in front of the final focus quadrupole and covers polar angles between 5 and 40 mrad. The third system, the LHCAL, ensure the coverage of the hadron calorimeter to small polar angles.

WHY ?

Magnetic Field and yoke

By applying a high magnetic field inside the detector, the charged particles have a bent track helping in the identification and the energy measurement. At the ILD, the nominal magnetic field is 3.5 T and should have a high homogeneity inside the TPC. Moreover, as mentioned in subsection 3.2.2, the magnetic beyond the coil has to be reduced to avoid any perturbations with the second detector in its parking position. A superconducting coil surrounding the tracking and calorimetric system generate the magnetic field. It has a diameter of 6.88 m, a length of 7.35 m and made of three modules.

Surrounding the coil, an iron yoke ensures to return the magnetic flux. It is constituted by a barrel of 2.88 m thickness and 2 end-caps of 2.12 m thickness. Muon detectors are inserted inside the iron yoke in a sandwich-like structure. They are performing measurement on muons but they are also used as tail catchers, to improve the energy resolution of high energetic jets escaping the calorimeters.

3.4 Conclusions

The pros and cons of a linear collider using a electron/positron beam have been discussed. The main advantage of this type of collider is to precisely know the initial collision state and to avoid any QCD background contamination. Thus, precise measurements of the Higgs boson, such as a fine determination of its mass, its width and its couplings could be performed. Contrary to the LHC, which is using the tunnel built for Large Electron Positron collider (LEP), the ILC will be built on a new site. The tunnel, the accelerator, the detectors and the scientific campus have to be built. To reduce the costs, only one interaction region is planned, on which two detectors are going to be operated alternatively. The design of these detectors is driven by the particle flow approach, which sets an energy resolution of $30\ \%/\sqrt{E(\mathrm{GeV})}$ for the calorimeters. The ILD detector concept was introduced and the different sub-detectors and technology options were discussed, except for the vertex detector. The chapter 5 is dedicated to the vertex detector at the ILD.

After describing the status of the SM and the next high-energy experiment, the next chapter will introduce the physics cases at the ILC, especially by describing an approach of a physics analysis to study the $H \to c\bar{c}$.

Chapter 4

Physics at the ILC

In chapter 2, the framework of particles physics was described. Since the beginning of the high-energy physics, different experiments have been performed to confirm the exactness of the Standard Model (SM) and to try to find traces of new physics beyond the SM. Depending on the type of colliders used, the measurements do not achieved the same precision. For example, the LHC with its high luminosity and high energy beam, is able to reach new energy scales, whereas the ILC with its electron/positron interaction at lower energy beam is able to perform more precise measurements, due to the known initial state and the free QCD background. Along this chapter, the physics scenarios that are scheduled at the ILC are discussed. Afterward, the emphasis will be on the Higgs physics and the measurement that would be performed at the ILC. The last section aims to introduce a physics analysis scenario to study the processes leading to a Higgs boson and two neutrinos in the final state.

Contents

4.1 Potential studies

As seen in chapter 3, the ILC will have a vast and variable tunable centre-of-mass energy. Due to the features of an e^-e^+ collider, there is no contribution from strong interaction background and the initial state of collision is well defined, contrary to the LHC. Moreover, the electroweak background is calculable and controlled. All the conditions are reunite to perform precise physics measurements and to look for an evidence of new physics beyond the SM. The different measurements which will be performed are presented below.

First of all, a study of the Z boson at the centre-of-mass energy of $\sqrt{s}$ = 91 GeV around the Z resonance is scheduled. This program called *GigaZ* will be able to collect more Z boson events than the Large Electron Positron collider (LEP) did, because of a luminosity two to three times higher than what was achieved. The data collected will allow a study on the asymmetries of the Z boson couplings. A second program, called *MegaW*, will be performed at the centre-of-mass energy of $\sqrt{s}$ = 160 GeV reaching the WW production threshold and trying to measure the W boson mass with a precision of MeV/c^2. At higher energy, it will also be possible to measure more precisely the W boson couplings.

Afterward, the centre-of-mass energy will be adjusted to $\sqrt{s}$ = 250 GeV to perform a study on the Higgs boson couplings, as well to measure the quantum numbers associated to the boson. At this energy, the Higgs boson is mainly procduced via Higgs-strahlung. The measurement is done thanks to the recoil mass independently of the Higgs decay products.

Then, for a centre-of-mass energy between 350 and 400 GeV, two studies are achievable. The WW-fusion process starts to rise and permits to measure the couplings of the Higgs boson to the W ones in order to look for deviation from the Standard Model. Moreover, this channel allows to study some rare decays. This energy range corresponds also to the threshold of the top quark pairs production. Due to the top quark life-time, the two quarks created are not in a bounded-state. By performing a threshold scan, the mass of the top quark can be measured with a precision reaching 100 MeV/c^2.

The nominal energy of the ILC is achieved at $\sqrt{s}$ = 500 GeV. This energy scale is suitable to look for supersymmetry candidates and possible extended states of the Higgs boson.

An upgrade of the ILC to reach the centre-of-mass energy $\sqrt{s}$ = 1 TeV is also scheduled. Up to 1 TeV, new measurements are possible, such as the coupling of the Higgs boson to the top quark, the Higgs boson self-coupling, or its compositeness. Although, search for new exotic particles and physics beyond the SM is possible.

The table 4.1 summarises the different physics programs at the ILC for the different energy reachable.

Energy (GeV)	Reaction	Physics Goal
91	$e^+e^- \to$Z	ultra-precision electroweak
160	$e^+e^- \to WW$	ultra-precision W mass
250	$e^+e^- \to Zh$	precision Higgs coupling
350 - 400	$e^+e^- \to t\bar{t}$	top quark mass and couplings
	$e^+e^- \to WW$	precision W couplings
	$e^+e^- \to \nu\bar{\nu}h$	precision Higgs couplings
500	$e^+e^- \to f\bar{f}$	precision search for Z'
	$e^+e^- \to t\bar{t}h$	Higgs coupling to top
	$e^+e^- \to Zhh$	Higgs self-coupling
	$e^+e^- \to \tilde{\chi}\tilde{\chi}$	search for supersymmetry
	$e^+e^- \to AH, H^+H^-$	search for extended Higgs states
700 - 1000	$e^+e^- \to \nu\bar{\nu}hh$	Higgs self-coupling
	$e^+e^- \to \nu\bar{\nu}VV$	composite Higgs sector
	$e^+e^- \to \nu\bar{\nu}t\bar{t}$	composite Higgs and top
	$e^+e^- \to \overline{t}t^*$	search for supersymmetry

Table 4.1 – Summary of the major processes that will be studied at the ILC for different energies [5].

4.2 Higgs physics

The Higgs boson found at the LHC has to be characterised more precisely. One of the goal study at the ILC is to determine if the particle found is compatible with the one defined by the Standard Model, or if other states exist. The measurement of the Higgs boson couplings to the Standard Model particles is one of the key to verify the exactness of the mass generation mechanism described by this theory and to open the door to any proof of physics beyond the Standard Model. The production, the decay modes of

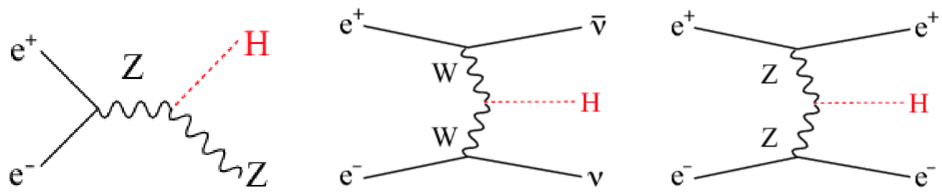

(a) Higgs-Strahlung **(b)** WW-fusion **(c)** ZZ-fusion

Figure 4.1 – Feynman diagrams of the main Higgs production at the ILC [4][70].

the Higgs boson, as well as the measurement feasible are presented below in the case of the ILC.

4.2.1 Production of the Higgs at the ILC

Due to the beam structure at the ILC, the Higgs boson is accessible by direct measurement. The production of the Higgs boson defined by the Standard Model is done via three major processes: the Higgs-strahlung (see figure 4.1a), the WW-fusion (see figure 4.1b) and the ZZ-fusion (see figure 4.1c).

$$\textbf{Higgs-strahlung: } e^+e^- \rightarrow ZH \rightarrow f\overline{f}X$$

$$WW\textbf{-fusion: } e^+e^- \rightarrow \nu_e\overline{\nu_e}W^+W^- \rightarrow \nu\overline{\nu}H$$

$$ZZ\textbf{-fusion: } e^+e^- \rightarrow e^+e^-ZZ \rightarrow e^+e^-H$$

At the centre-of-mass energy $\sqrt{s} = 250$ GeV, the Higgs-strahlung is the dominant process and occurs via a s-channel. Its cross-section falls off as $1/s$ as the centre-of-mass energy $\sqrt{s}$ increases. Contrary to the Higgs-strahlung, the WW-fusion and the ZZ-fusion are t-channel processes which have a cross-section growing logarithmically with the centre-of-mass energy. Thus, at 250 GeV, the cross-section of the WW-fusion is one order smaller than the Higgs-strahlung and the ZZ-fusion is negligible. Nevertheless, around 500 GeV, the WW-fusion and the Higgs-strahlung have the same cross-section, which is around 120 fb. The figure 4.2 shows the cross-section production of the Higgs at the ILC regarding the energy of the collision.

The WW-fusion occurs only with left-handed electrons associated to right-handed positrons. Thus, by modifying the beam's polarisation, the signal mixture can be changed, as well as the background processes.

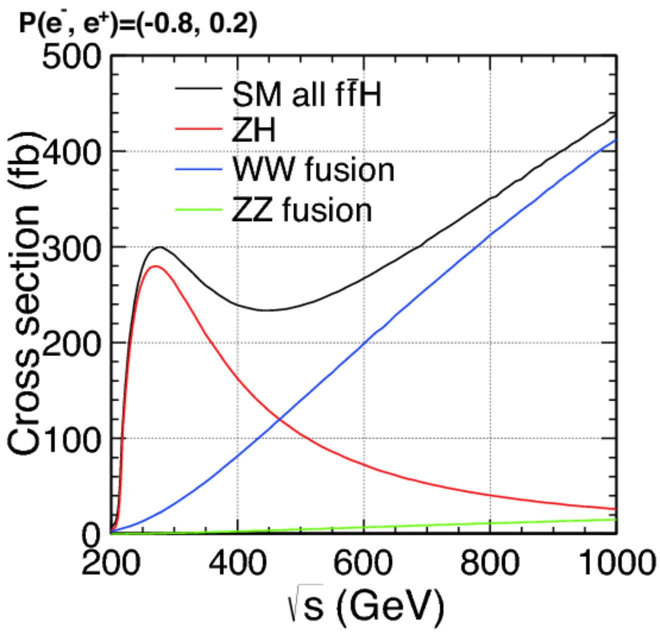

Figure 4.2 – The cross section production of the Higgs boson with a mass of 125 GeV [4].

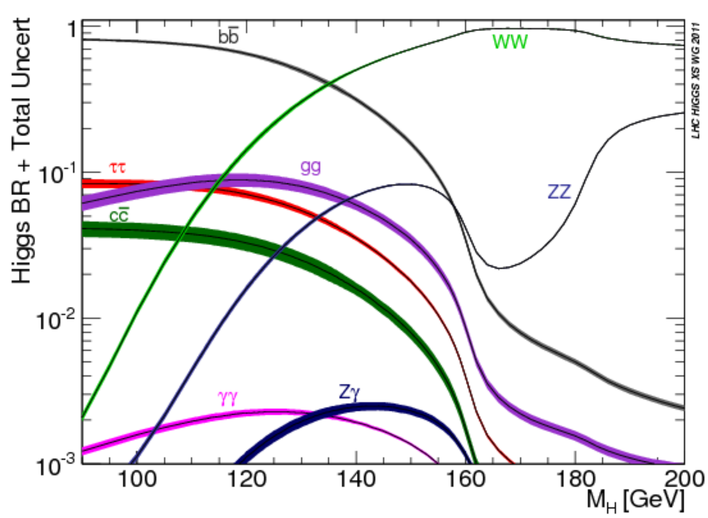

Figure 4.3 – The Higgs branching ratio with the branching ratio uncertainties for the Higgs mass varying from 80 to 200 GeV [21].

4.2.2 Higgs studies

This section gives few ideas of possible Higgs physics studies.

Mass measurement

The first study will be at the peak production of the Higgs-strahlung. The well defined four-momentum initial state allows to measure the Higgs boson mass regardless its decay products. The Higgs invariant mass M_H can be calculated by using the recoil technique:

$$M_H^2 = s + M_Z^2 - 2\sqrt{s}\,(E_1 + E_2)\,, \tag{4.1}$$

where M_Z is the mass of the Z boson, E_1 and E_2 are the energy of the Z decay products. This technique works well for the Z boson decaying into leptons at the centre-of-mass energy $\sqrt{s} = 250$ GeV. However, this method can not be performed for a Higgs decaying into quarks at the same energy. The Z and the Higgs bosons are produced almost at rest, thus, the identification of the jets coming from the Z boson to the ones coming from the Higgs is more difficult. Nevertheless, at higher energy ($\sqrt{s} = 500$ GeV), the two bosons are enough boosted to separate their jets and then to apply again the recoil mass. Depending on the decay channel of the Z boson, the statistical precision on the mass measurement varies between 40 MeV (for $Z \to \mu^+\mu^-$) to 80 MeV (for $Z \to e^+e^-$) and can reach 32 MeV by combining the two results.

Spin measurement

At the thresholds production of the Higgs-strahlung ($\sqrt{s} = 250$ GeV), besides the mass measurement, the determination of the spin and the CP-violation are scheduled. From the LHC analysis, it has been determined that a spin-1 Higgs boson is forbidden because of the di-photon channel observation [69]. The spin will be determined by studying the Higgs-strahlung production mode. The cross-section has different behaviour, depending on the spin and the CP-violation. For a spin-0 and CP-even Higgs boson, the production cross-section follows s, whereas for CP-odd, it has a $\sqrt{s}^3$ dependency.

Branching ratio measurement

Although the decay $H \rightarrow b\bar{b}$ is the dominant decay mode of the Higgs at hadrons colliders, the existence of the boson was observed by studying the di-photons channel. The other decay states are challenging to separate from the background. The properties of the ILC beam allow to perform measurements of the Higgs couplings to the particles defined in the SM. Thus, the following decay modes are available: $b\bar{b}$, WW, ZZ, gg, $c\bar{c}$, $\tau\tau$, $\gamma\gamma$, γZ. The observation of the $H \rightarrow c\bar{c}$ is one of the constraint parameter to build the detectors, specifically, the vertex detector that should be able to distinguish the vertices coming from the b-quarks to the ones coming from the c-quarks. The figure 4.4 depicts the mass-coupling relation of the Higgs boson to the particles of the SM. Any deviations from the Higgs fermionic coupling would indicate multiple states for the Higgs boson.

H decays at LHC: bb, WW, tau tau, gamma gamma, gg and ZZ

Not clear enough

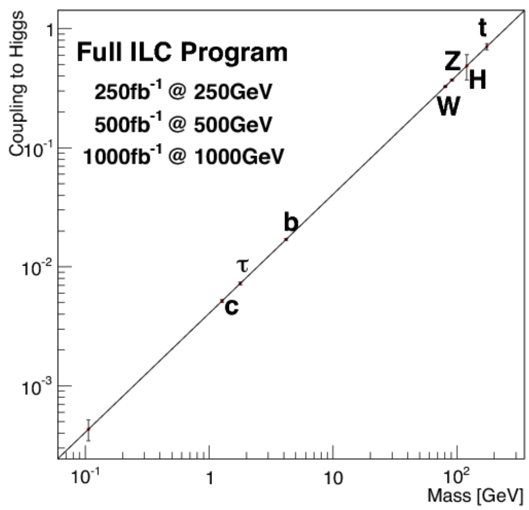

Figure 4.4 – Mass-coupling relation of the Higgs boson to the particles defined in the standard model [70].

4.3 Analysis of simulated data

Due to the restricted time to conduct the thesis, this section is introducing the tools to perform an analysis of simulated data at the ILD. The results shown here are not the last update and are already demonstrated [30]. Nevertheless, the philosophy to perform a study of the Higgs production at the center-of-mass energy $\sqrt{s} = 350$ GeV and a luminosity of 250 fb^{-1} is here presented.

4.3.1 Simulation set-up

The physics events are generated with Monte-Carlo simulation tools and is performed with different software. The collisions of electrons and positrons is done with the software WHIZARD [72]. It supports the SM processes, as well as a large variety of BSM models. For linear collider physics, the beamstrahlung, the Initial State Radiation (ISR) and the beam polarisation are simulated, but the hadronisation and fragmentation are not implemented and the simulation of this events was performed with PYTHIA [62].

The linear collider community has developed Monte-Carlo simulation and analysis software frameworks dedicated for a future linear collider, such as the ILC. The different packages developed by the community are grouped into the ILCSoft framework [42]. It includes software for Monte-Carlo simulation, as software for test beam analysis (see chapter 8) and other tools. The main package is the Linear Collider I/O (LCIO), a persistence framework and event data model for the linear collider detector studies [50]. It provides a common data format and event data model for both the simulation studies and the analysis framework in order to share results and compare reconstruction algorithms.

Afterward the physics events are generated, the particle interaction inside the detector is simulated with Mokka [57]. The software is based on GEANT4 simulation toolkit [34] and is part of the ILCSoft. For the analysis, the detector model used is ILD_o1_v05. This model simulates the dead areas due to cabling, cooling system and mechanical structure and has a silicon-tungsten electromagnetic calorimeter, as well as an analog hadronic calorimeter.

The detector geometry is described by a XML steering file and is used as an interface during the data reconstruction and analysis. This is managed by the GEometry Api for Reconstruction (GEAR) software [35].

Finally, the events are reconstructed with the Modular Analysis and Reconstruction for the LINear collider (Marlin) package [22]. It is a C++ software framework used for the data reconstruction and the data analysis and it handles LCIO data format. The different steps of the analysis or the reconstruction are grouped into modules, also called processors that read an input file, perform the defined tasks and write an output file that could be processes by another Marlin module. A steering file written in XML is used to select the processors to use and the order of their execution time.

4.3.2 Event generation

Event samples

The ILD generator group has produced signal and background samples for two different polarisations: $\mathcal{P}_{e^-,e^+} = (-1, +1)$ and $\mathcal{P}_{e^-,e^+} = (+1, -1)$. Although the scheduled polarisation are $\mathcal{P}_{e^-,e^+} = (-0.8, +0.3)$ and $\mathcal{P}_{e^-,e^+} = (+0.8, -0.3)$, the simulated beam polarisation is re-weighted according to:

$$\begin{aligned} \sigma_{\mathcal{P}_{e^-,e^+}} &= \tfrac{(1-P_{e^-})(1+P_{e^+})}{2}\sigma_{LR} + \tfrac{(1+P_{e^-})(1-P_{e^+})}{2}\sigma_{RL}, \\ \sigma_{-0.8,+0.3} &= 0.585 \times \sigma_{LR} + 0.035 \times \sigma_{RL}, \\ \sigma_{+0.8,-0.3} &= 0.035 \times \sigma_{LR} + 0.585 \times \sigma_{RL}. \end{aligned} \tag{4.2}$$

The cross-section σ_{LR} is for the polarisation $\mathcal{P}_{e^-,e^+} = (-1, +1)$, whereas σ_{RL} is the cross-section of the polarisation $\mathcal{P}_{e^-,e^+} = (+1, -1)$. On the one hand, the Higgs-strahlung and the WW-fusion processes are equally important for the beam polarisation $\mathcal{P}_{e^-,e^+} = (-0.8, +0.3)$, leading to a larger $\nu\overline{\nu}H$ cross-section. On the other hand, the polarisation $\mathcal{P}_{e^-,e^+} = (-0.8, +0.3)$ is used to perform a cross-check measurement. The W-boson cannot couple to right-handed electrons and left-handed positrons. Thus, the WW-fusion process is largely suppressed. Besides, the Z-boson depends on the isospin and the Higgs-strahlung contribution is also reduced but not suppressed. The same effect occurs on the backgrounds leading to a smaller background contamination on the signal and a cleaner signal sample for the Higgs-strahlung.

The data set are scaled to an integrated luminosity of 250 fb^{-1} for each beam polarisation.

Signal

The signal to study is the final state $\nu\overline{\nu}H$, on which the Higgs boson decays into a pair of quarks, such as $H \to b\bar{b}$ and $H \to c\bar{c}$, or a pair of gluons $H \to gg$. The other decay modes are considered here as a source of background. The dominant production processes leading to this final state are the Higgs-strahlung and the WW-fusion. Their leading order Feynman diagrams are displayed respectively on figure 4.1a and 4.1b. Although the neutrinos produced in the WW-fusion process are only ν_{e} and all neutrino flavors are equi-probable in the Higgs-strahlung, the neutrino flavors cannot be detect and only the missing energy is the signature of neutrino production.

The figure 4.5 represents the distribution of the missing mass for the signal events for the two polarisations considered at the ILC. The first effect

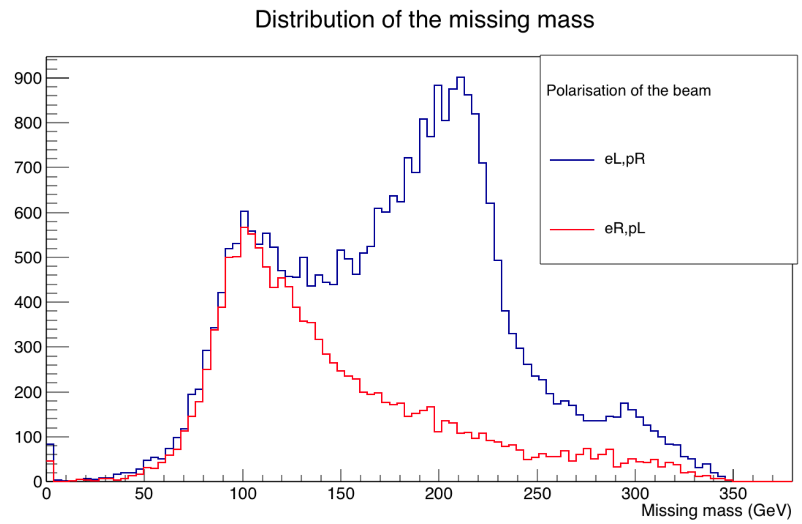

Figure 4.5 – Distribution of the missing mass with different beam polarisations and for the Higgs-strahlung and WW-fusion leading to $\nu\overline{\nu}H$ final state. The background contribution is not taken into account here.

of the polarisation is the suppression of the WW-fusion contribution and also a reduction of the Higgs-strahlung for right-handed electrons and left-handed positrons. For the other polarisation, the missing mass distribution shows three peaks. Once centered around 90 GeV corresponding to the decay of the Z-boson into a pair of neutrinos. The second peak is broader and its maximum is at 200 GeV. This comes from the WW-fusion. A third peak is visible at 300 GeV and is coming from the Higgs boson decaying not hadronically and is considered as a source of background.

Background processes

The signal hypothesis is that the final state is consisting of two jets coming from the hadronic decay of the Higgs boson, as well as missing energy coming from the undetected neutrinos produced by the Z boson decay. Nonetheless, this signal is drown into the background processes. The background consists to the events with the same final states as the signal, called irreducible background and the events with a similar detector response. Their contributions depend on the beam polarisation. For example, the cross-section for a beam polarisation $\mathcal{P}_{e^-,e^+} = (+0.8, -0.3)$ is smaller by an order of magnitude due to the W boson.

Two irreducible backgrounds are considered here, the one involving a W-boson exchange and the one with a Z-boson exchange. The cross-section of this processes is few times larger than the signal one. For both, single W-boson and Z-boson exchange, the final state contains two jets with missing energy. Nevertheless, the final state with quarks is more likely than the final state with two gluons due to the loop formed in the final state on which the gluons are emitted.

The background involving W-bosons, such as $e^-e^+ \to W^{\pm}e^{\pm}\nu_e \to e^{\pm}\nu_e q\overline{q}$ is two orders magnitude bigger than the signal cross-section. The neutrino produced carries a large transverse momentum, whereas the electron or positron has a low transverse momentum. Hence, it can be undetected and be considered as a missing energy.

The W-pair production can lead to semi-leptonic, hadronic and leptonic decay modes. The semi-leptonic mode consists of two jets and a lepton with its associated neutrino ($e^+e^- \to W^+W^- \to \nu_l l^{\pm} q\overline{q}$) and it is the major background process for the W-pair production. This background is detected by looking for an isolated lepton. Nevertheless, the lepton could escape the detector undetected or be inside a jet. The second W-pair production is the hadronic decay on which there is no missing energy ($e^+e^- \to W^+W^- \to q\overline{q}q\overline{q}$). This background is reduced by applying cuts on the missing momentum and the di-jet invariant mass. The last contribution is the leptonic final state, which is easy to distinguish from the signal. Thus, it is not considered in the study.

The Z-pair background is ten times smaller than the W-pair production. The $e^+e^- \to ZZ \to \nu_l\overline{\nu_l}q\overline{q}$ process is an irreducible background. The hadronic decay $e^+e^- \to ZZ \to q\overline{q}q\overline{q}$ is reduced by cutting on the missing momentum and the di-jet invariant mass. The semi-leptonic process $e^+e^- \to ZZ \to l^+l^-q\overline{q}$ is easier to detect because of the second isolated lepton in the event.

Finally, the last background to take into account is the one with the Higgs boson produced in the final state. The Higgs-strahlung can lead to $q\overline{q}H$ and $l^{\pm}l^{\mp}H$ has cross-section three times larger than the signal, but it is easily identify due to the absence of neutrino. All the decay mode of the Higgs different from $H \to b\bar{b}$, $H \to c\bar{c}$ and $H \to gg$ are considered as part of the background.

The figure 4.6 displays the distribution of the visible mass for all the processes taken into account during the analysis and a beam polarisation $\mathcal{P}_{e^-,e^+} = (-0.8, +0.3)$. A selection has to be performed in order to isolate the peak at 125 GeV.

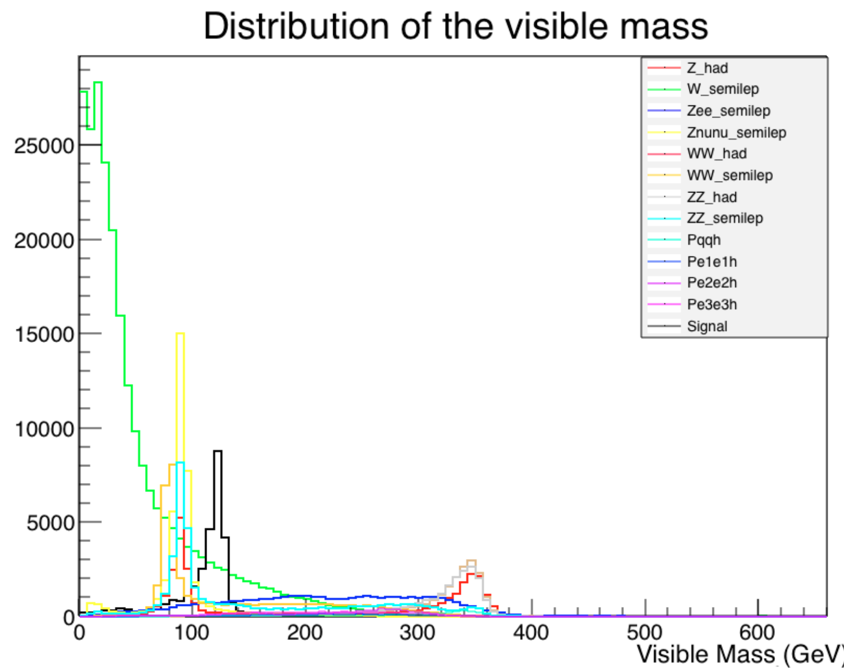

Figure 4.6 – Distribution of the visible mass for the signal and background together and the polarisation $\mathcal{P}_{e^-,e^+} = (-0.8, +0.3)$.

4.4 Results

4.4.1 Event reconstruction

The assumption to study the $H\nu\nu$ channel is to reconstruct a final state which is giving a two jets and missing energy in the detector response. The reconstruction consists to select and highlight this detector response.

The first step consists to identify in the events the presence of isolated leptons in the final state and to remove them from the physics list. The lepton detected outside a jet are considered as a source of background. Thus, a neural network is used to identify in an event the different leptons and checks if they belong to a jet. This selection is based on different criteria, like the vertex information, the energy deposited inside the ECAL, the HCAL and the muon system. The processor used for the identification is called *IsolatedLeptonTagger* and has a veto efficiency of roughly 90 %. The 10 % of leptons undetected are coming from events in which the leptons are moving into the forward region and they could escape the detector without being identify by the processor. A better selection is done after the jet reconstruction and is discussed later.

A second source of background is coming from the $\gamma\gamma$ interactions which produce low p_t hadrons. This hadrons with a small transverse momenta and a small relative angle to the beam axis are detected as jet-like objects in the forward region of the detector. The identification of the beam jets is based on the k_T algorithm [10]. It consists to define a "distance" d_{ij} between two particles and to find the first closest constituent.

$$\begin{aligned} d_{ij} &= \frac{\min\left(\mathrm{p}^2_{\mathrm{T_i}},\mathrm{p}^2_{\mathrm{T_j}}\right)\cdot\Delta\mathrm{R}^2_{\mathrm{ij}}}{R^2}, \\ d_i &= p^2_{T_i}, \end{aligned} \tag{4.3}$$

with $\Delta R^2_{ij} = (y_i - y_j)^2 + (\phi_i - \phi_j)^2$, y_i the pseudo rapidity, ϕ_i the azimuthal angle and p_{T_i} the transverse momentum of the particle studied. The minimum between d_{ij} and d_i is calculated. If d_{ij} is the minimum value, then, the particles i and j are merged into a jet candidate, they are then removed from the physics list and the jet candidate is added instead. If the minimum value is d_i, the particle is considered to be part of the beam jet and is removed from the particle lists. This algorithm is repeated iteratively until the number of jets created is equal to the number of jets expected.

After removing the isolated leptons and the low p_t hadrons from the physics list, the jet clustering and the flavor tagging processors are applied. Because of the k_T algorithm, which removes particle from the physics list, the vertex finder is run again before to use the jet clustering algorithm.

4.4.2 Event selection

To improve the signal to noise ratio, an event selection is performed by applying different cuts that reduce the background contribution. The order and the performances of the selection cuts are determined by maximising the significance s, which is:

$$s = \frac{\mathrm{N_{sig}}}{\sqrt{\mathrm{N_{sig}} + \mathrm{N_{bg}}}}, \tag{4.4}$$

with, $\mathrm{N_{bg}}$ the number of remaining background and $\mathrm{N_{sig}}$, the number of remaining signal. The maximisation of s is needed to minimise the statistical error. Firstly, the procedure starts with the definition of a collection of observables that could help to discriminate the signal from the background. Then, a test of the possible cut values is performed in a given range and for a given step size. The value leading to the largest significance is chosen as the optimum observable and is the first selection variable which is applied to a signal sample (containing WW-fusion and Higgs-strahlung processes) and the least tight constraint is selected in order to maintain a good signal efficiency. Finally, the cut values of this optimum observable is applied on the complete data set and the procedure is applied again.

The first observable to be applied is the veto information used to find any isolated lepton. As already mentioned, the *IsolatedLeptonTagger* processor has a veto efficiency of roughly 90 %.

The second observable is the visible transverse momentum $P_{\mathrm{t,vis}}$ of the di-jets.

$$\begin{aligned} P_{\mathrm{t,vis}} &= \sqrt{P^2_{x,vis} + P^2_{y,vis}}, \\ P_{\mathrm{x/y,vis}} &= P_{\mathrm{x/y,j1}} + P_{\mathrm{x/y,j2}}. \end{aligned} \tag{4.5}$$

$P_{\mathrm{x/y,j1}}$ and $P_{\mathrm{x/y,j2}}$ are the visible momentum in the x and y-directions for the two jets $j1$ and $j2$.

The third observable is the invariant visible mass m_{vis}, which is the signal signature.

$$\mathrm{m_{vis}} = \sqrt{\mathrm{E}^2_{\mathrm{vis}} - \overrightarrow{P}^2_{\mathrm{vis}}}, \tag{4.6}$$

with E_{vis} and P_{vis} the visible energy and momentum of the event. The expected visible mass is $\mathrm{m_H}$ = 125 GeV and its width is mainly driven by the jet energy resolution.

The table 4.2 summarises the order of the different cut selection for different observables applied on the simulated data set. After eight consecutively cuts, the background contribution is three orders smaller, whereas the signal is almost one order smaller than the beginning. Nevertheless, the significance is still less than 70 and applying more cuts is affecting strongly the signal.

4.5 Outlooks

To preserve the sample quality, it is rather better to use a multivariate analysis (MVA) method to extract the signal from the background. The complete information is then used simultaneously to find the best sets of variable. This

Process	Background	Signal	Significance
Cross-section (fb)	$5.69 \cdot 10^4$	$6.82 \cdot 10^2$	
Expected event number	$1.88 \cdot 10^7$	$2.25 \cdot 10^4$	5.2
No isolated leptons	$1.65 \cdot 10^7$	$2.23 \cdot 10^4$	5.5
$35 < \mathrm{P_t^{vis}} < 155$ GeV	$9.31 \cdot 10^5$	$1.82 \cdot 10^4$	18.7
$95 < \mathrm{m_{vis}} < 140$ GeV	$1.50 \cdot 10^5$	$1.66 \cdot 10^4$	40.6
$-1 < \cos\alpha < 0.22$	$8.76 \cdot 10^4$	$1.57 \cdot 10^4$	48.8
26 < (N.R.C > 1GeV) < 99	$2.25 \cdot 10^4$	$1.19 \cdot 10^4$	56.3
0.11 < DurhamjD2ym < 1	$1.78 \cdot 10^4$	$1.05 \cdot 10^4$	62.3
0 < abs(RefinedjPzvis) < 113 GeV	$1.51 \cdot 10^4$	$1.01 \cdot 10^4$	63.5
156 < RefinedjEmiss < 230 GeV	$1.37 \cdot 10^4$	$9.85 \cdot 10^3$	64.1

Table 4.2 – Cut-flow table for a beam polarisation $\mathcal{P}_{e^-,e^+} = (-0.8, +0.3)$.

analysis was already performed and a MVA method was used, achieving a significance above 70.

The next step of this analysis is to focus on the decay mode of the Higgs boson into two pairs of charmed quarks and to optimise the flavor tagging performances to separate more accurately the b and c quarks events. For the events and the detector simulated in this chapter, the vertex detector geometry was not optimised and was made of five single sided layers. Nevertheless, the double sided option has to be investigated. This geometry offers multiple possibilities, like using two different types of sensors on the same ladder or the possibility of two point measurements per ladder for a track. One side could be equipped with ultra-fast integration time ($\mathcal{O} \sim 1\ \mu$s) sensors, whereas the other side could embed sensors with an excellent pointing resolution ($\sigma_{\mathrm{s.p}} \leqslant 3\ \mu$m). With two sensors on the same mechanical structure, a track is reconstructed by two points of measurement. Thus, these two measurements could be combined together to form "mini-vectors". Studying the "mini-vectors" could help to identify the beam-strahlung from the collision events.

Chapter 5

As light as a feather

Since the end of the 1960's, the development of position sensitive silicon sensors has permitted to confirm the prediction of the Standard Model (SM) with a high precision, as well as the discovery of the top quark. These sensors, mostly employed for the Vertex Detector (VXD), are in charge to track the particles down to their decay vertices. The design of such device is driven by the physics requirement of the experiment and is playing a crucial role at the International Linear Collider (ILC). For example, one flagship measurement is the study of the Higgs boson couplings to the fermions and other bosons. This can be achieved only with a precise heavy flavor tagging and the ability to separate the b quarks from the c quarks. Actually, the lifetime of the two quarks is of the same magnitude ($1.3 \cdot 10^{-12}$ s for the b quark and $1.1 \cdot 10^{-12}$ s for the c quark), leading to very close decay vertices.

Along this chapter, the role of the vertex detector and the physics requirements to develop one for the ILC environment will be presented. Then, the different options of the International Large Detector (ILD) are shown, to focus on the double-sided ladders developed by the PLUME collaboration. To finish, the principle of Complementary Metal Oxide Semi-conductor (CMOS) sensors and their use in physics are described.

Contents

5.1 The ILD vertex detector specifications

The VXD is the closest sub-detector to the interaction point (IP) in charge of reconstructing the vertex by extrapolating particles back to their origin of production. This detector should be optimised to track particles in a high-density environment and to be able to extract the tracks from the different particles, especially those originating from the decay of the b and c quarks in the case of the ILC. The reconstruction of the displaced vertices should be efficient enough to perform a good flavour tagging. Therefore, the detector has to measure particles with a lifetime in the picosecond regime, representing a decay length between 150 and 500 μm. The minimum distance of the first VXD layer is determined by the beam pipe radius, and the background induced by beamstrahlung, to limit the pixel occupancy. This sub-detector has a central role in the tracks' reconstruction. Depending on the option chosen (see section 5.1.2), the VXD has to provide five or six points of measurement with a very high precise spatial resolution. For the studies requiring vertex charge identification, it should be able to reconstruct low-momentum and very forward tracks.

5.1.1 Physics requirements

The ideal VXD should be made of sensors with a fine granularity in order to increase the ability to locate precisely the particle impacts and to distinguish two nearest particles. The mechanical structure of the detector should provide a good stiffness and stability of the whole system but has to be at the same time as light as possible to reduce the interaction of the particles traversing it, before they reached another part of the main detector. As well, in order to reduce the unwanted interactions, the sensor technology used has to have a low power consumption to avoid any special cooling system which can have a bad impact on the material budget. The design of such detector, like the minimal distance of the first layer to the IP and the spacing between different layers, is determined by both the beam background and the physics to study. The flavour tagging ability, the vertex charge measurement and tracking, and the displaced vertices reconstruction are the main physics parameters driving the design. The distance of closest approach of a particle to the collision point is called the impact parameter and the resolution achievable by the detector can be approximated with formula 5.1 [6].

$$\sigma_{IP} = a \oplus \frac{b}{p \sin\theta^k} \text{ , with k } = \begin{cases} \frac{3}{2} & \text{in the } R-\Phi \text{ projection,} \\ \frac{5}{2} & \text{in the z projection.} \end{cases} \tag{5.1}$$

Where θ is the track polar angle (ILD coordinate systems are presented in section 3.3.3), a and b are explained in the following.

The first term a is the impact parameter resolution of the sensors used for the VXD, which is linked up to the radius of the inner R_{int} and outer R_{ext} layers and the single point resolution $\sigma_{s.p.}$, as described in equation 5.2.

$$a = \sigma_{s.p} \cdot \frac{R_{\text{int}} \oplus R_{\text{ext}}}{R_{\text{ext}} - R_{\text{int}}}. \tag{5.2}$$

In the case of the ILD, the single point resolution should not be higher than $\sigma_{sp} \simeq 3$ μm, leading to an impact parameter with a resolution of the order of $a \simeq 5$ μm.

The second term, b, presented in equation 5.3, is related to the multiple scattering inducing an uncertainty on the impact parameter. It depends on the charge Z of the impinging particle, the material crossed by the particle $\frac{x}{X_0 \sin\theta}$ and the distance of the innermost layer to the IP. Depending on the momentum or the crossing angle of the incoming particles, the two parameters are more or less important. For low momentum particles or crossing particles with a shallow angle, the b parameter becomes important, while for higher momentum a dominates.

$$b = R_{int} \frac{13.6 MeV/c}{\beta c} \cdot Z \cdot \sqrt{\frac{x}{X_0}} \left[1 + 0.036 \cdot \ln\left(\frac{x}{X_0 \sin\theta} \right) \right]. \tag{5.3}$$

For the ILC purpose, the ILD-VXD should reach an impact parameter resolution better than 5 μm and a b parameter better than 10 μm GeV/c.

This precision on these parameters were never obtained before in other experiments. As a comparison, typical parameter values for LHC experiments are: $a = 12\ \mu$m and $b = 70\ \mu$m GeV/c.

5.1.2 Layout of the vertex detector

The VXD will be made of 12 cm long ladders arranged cylindrically in concentric layers to form long-barrels surrounding the IP, contrary to the SiD vertex detector with a design based on a 5 layers barrel, four endcap disks and three additional forward pixel disks [9]. Two different geometries are under consideration for the ILC-ILD, nevertheless, they are both based on long ladders. The first option is based on five single-sided layers with a material budget not exceeding 0.11 % of X_0 per layer. The five layers are in a radius range varying from 15 mm for the first layer to 60 mm for the last one. The second option is based on three double-sided layers. The material budget should be less than 0.16 % X_0 for one detecting face. The mechanical structure, which holds the two layers, is 2 mm thick and will be in a radius range varying from 15 to 60 mm.

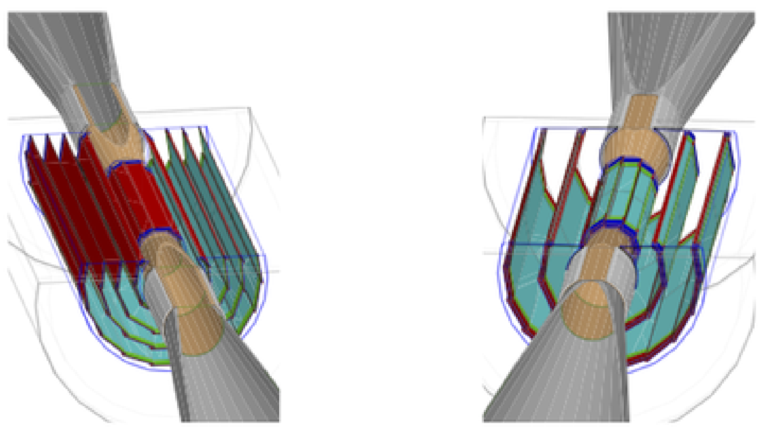

Figure 5.1 – Overview of the two vertex detector option for the ILC. On the left, it is made of five single sided layers, whereas the right one represents three double-sided layers.

Both geometry designs are based on pixel sensors instead of strips detectors. The currently considered technologies are presented below:

FPCCD

The Fine Pixels Charged Coupled-Device (FPCCD) [11] is based on the Charged Coupled-Device (CCD) processes. The sensor is using small pixels size (approximately $\sim 5\ \mu$m) to provide a sub-micron spatial resolution and an excellent capability to separate two nearby tracks. Its thickness is 50 μm and the epitaxial layer (15 μm thick) is completely depleted to limit the charge spreading around pixels and to reduce the number of hits per pixel. However, the CCD architecture provides slow readout and the matrix will be read between consecutive bunch trains, helping to reduce the power consumption and avoiding beam induced RF noise. The requirements for the radiation tolerance imposes the FPCCD to be operated at -40°C.

DEPFET

The Depleted P- Channel Field Effect Transistor (DEPFET) [64] is an Active Pixel Sensor (APS) in which field effect transistors are incorporated into each pixel. The single point resolution is $\sim 3\ \mu$m for pixels with a size of 20 μm. The silicon itself is used as sensitive part but also as a mechanical structure, minimising the support and services. The sensor is completely depleted of free charged carries thanks to a voltage applied to the thickness. The rolling-shutter approach is used for reading each row and the column readout is done by two auxiliary Application-Specified Integrated Circuits (ASICs).

The DEPFET technology is the one chosen to build the vertex detector of the BELLE-II experiment [18].

CMOS

Different options for CMOS pixel sensors are studied, such as the 3D integrated CMOS, but due to the context of this thesis, the work will focus on the CMOS sensors based on the Minimum Ionizing MOS Active pixel sensor (MIMOSA) architecture developed by the Institut Pluridisciplinaire Hubert Curien (IPHC) of Strasbourg. This technology is described in section 5.3.

For all the technologies, the sensors' power consumption has to be minimised in a way to reduce the cooling system and in the same time the added material budget in the sensitive detector volume. As it was shown on figure 3.2 of chapter 3, the bunch train will last less than 1 ms for a dead time of 200 ms. Two possibilities are envisaged to benefit from the beam structure. The first one consists to store the hits information thanks to a time stamp during the bunch crossing and to read out the data after the last collision.

This method might be used by the FPCCD technology due to the slow integration time of the CCD. Another solution is to use power-pulsing. Right after the last collision, the sensors are switched off or the power consumption is reduced as mush as possible, and before the first collision, the sensors is switch on again. This pulsing method is studied by different collaborations.

Another aspect not discussed yet is the radiation tolerance of the detector, which is directly related to the beam background. The first layer is the most affected by the background and it should have a high radiation tolerance. The required radiation tolerance is about 1 kGy for the total ionising dose and a fluence of $10^{11}\mathrm{n_{eq}}.\mathrm{cm}^{-2}$ [8].

The efficiency of the VXD has also to be excellent in order to maximise the tracking performances. The efficiency is defined here as the ratio of detected particles over all the particles crossing the detector. If one layer of the vertex detector misses a hit, the track reconstruction will be less accurate

Cooling system, integration time, radiation tolerance, electromagnetic interference

To summarise, the expected parameters for the ILC are:

- An excellent impact parameter resolution: $a \sim 5$ μm and $b \sim 10$ μm,
- A material budget not exceeding 0.1 % X_0 per layer for the single-sided option (0.16 % X_0 for the double one),
- Radius of the first layer $\sim$ 15/16 mm.

5.2 PLUME

The Pixelated Ladder with Ultra-low Material Embedding (PLUME) project aims to produce double-sided ladder prototypes driven by ILC requirements [61]. Three labs in Europe are involved: the IPHC-Physics with Integrated Cmos Sensors and ELectron machines (PICSEL) in Strasbourg, the University of Bristol and DESY in Hamburg. The collaboration is studying the feasibility to build such elements of vertex detector using MAPS thinned down to 50 μm and is exploring the benefits of this design. Strasbourg is in charge to develop and mount the sensors on the modules, to take care of the readout and the Data AcQuisition (DAQ), and to provide a cooling system. The mechanical design, stability measurements and building the ladders are done by the University of Bristol, while DESY has studied the ladder mock-up, performed power-pulsing tests and is now characterising and validating the modules in the lab. In 2016, DESY has provided the opportunity to test the ladder in real conditions thanks to the test beam facility and the possibility to use the DAQ software developed at DESY: EUDAQ [28].

5.2.1 Design and goals

Figure 5.3 illustrates the design of a PLUME ladder. The ladder structure is defined by the sensors arrangement on the mechanical support (positioned next to each other). In this design, the stiffener is a 2 mm thick Silicon Carbide (SiC) foam which has a density varying between 8 % and 4 % (depending on the ladder version) and could be reduced to only 2 or 3 %. The choice of this foam results a good compromise between the stiffness and the thickness compare to other materials [46]. Figure 5.2 represents the Young Modulus as a function of the radiation length for different materials. The structure of the SiC foam is shown on figure 5.4. It is macroscopically uniform and has the advantage to be easily machinable. Nevertheless, it has a low thermal conductivity (50 $W.m^{-1}.K^{-1}$) and cannot be used to dissipate the heat though contact. On each side, a low mass flex-cable is glued, which is used to connect the sensors for powering and managing them. It is made of copper traces coated in Kapton, but new prototypes using aluminum traces are developed and currently tested in order to reduce the material budget. The ladder embeds twelve sensors, six on each face, that are glued and wire-bonded to the flex cable. On each flex-cable, a Zero Insertion Force (ZIF) connector is used for linking the modules to two external servicing boards, using a jumper cable. For the moment, the design is dedicated to the MIMOSA-26 sensors thinned down to 50 μm but it can be adapted to any kind of MAPS sensors having the same thickness. The main issues for the integration of MIMOSA-16 comes the power pulsing ability, as well as the power dissipation of these sensors. This issues will be discussed in the next section (see 5.2.2).

The aims of the collaboration are to build ladders with a material budget better than 0.35 % X_0 for a spatial resolution better than 3 μm, and thus to evaluate the benefits of a double-sided measurement.

5.2.2 Prototypes

Since 2009, the collaboration is studying the design, the production, the impact of the mechanical structure on the ladder's performances, but also how to power and control the sensors together. The first ladder prototype, called version-0 (V-0) was developed and tested in 2009. The purpose of this prototype was to settle the fabrication and the test beam procedures,

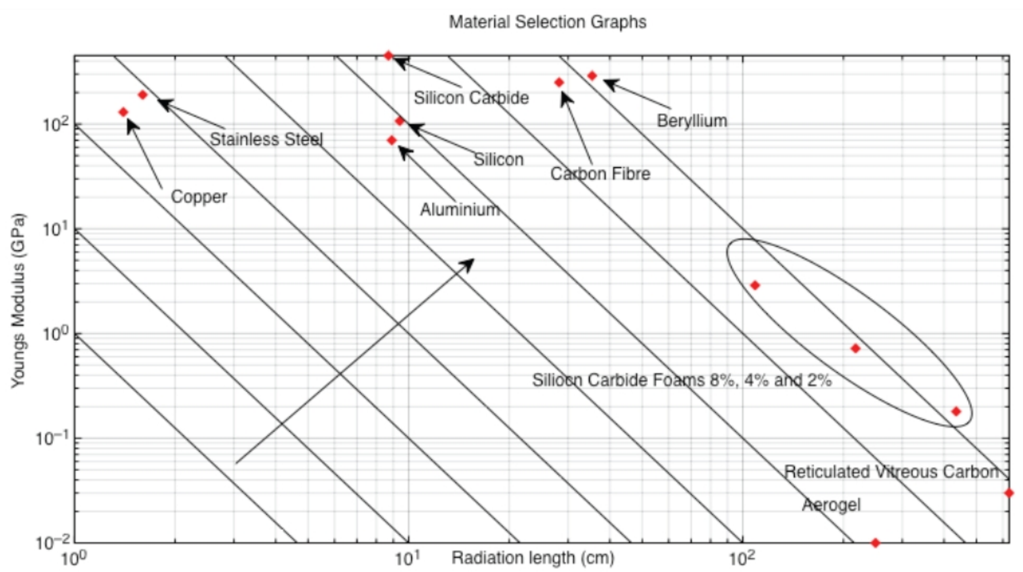

Figure 5.2 – Graph of the Young modulus in GPa as a function of the radiation length in cm for different materials.

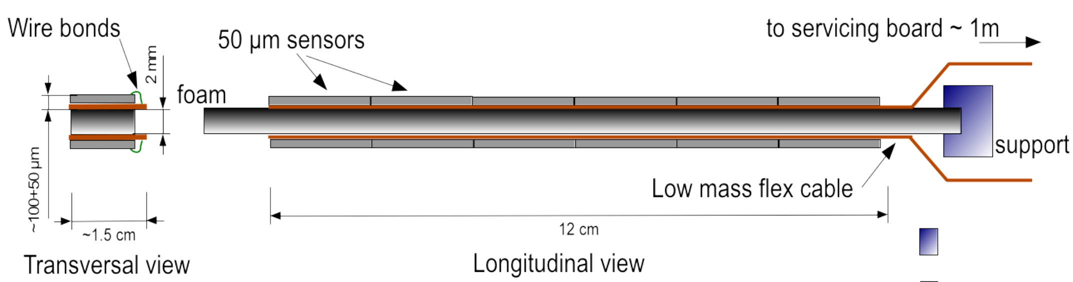

Figure 5.3 – Side view (transversal and longitudinal) of the PLUME mechanical structure.

without trying to reach the desired material budget goal. Two MIMOSA-20 analog output sensors were mounted on each side of a stiffener, providing a 1×4 cm^2 sensitive area. The prototype was tested in 120 GeV pion beam at the CERN-SPS and the results have demonstrated the benefits of the double-sided measurement on the spatial resolution, which is improved by about a $1/\sqrt{2}$ factor [59].

Then in 2010, a second prototype featuring the wanted sensitive surface,

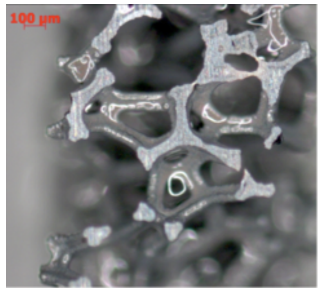

Figure 5.4 – Microscopical view of the silicon carbide foam structure.

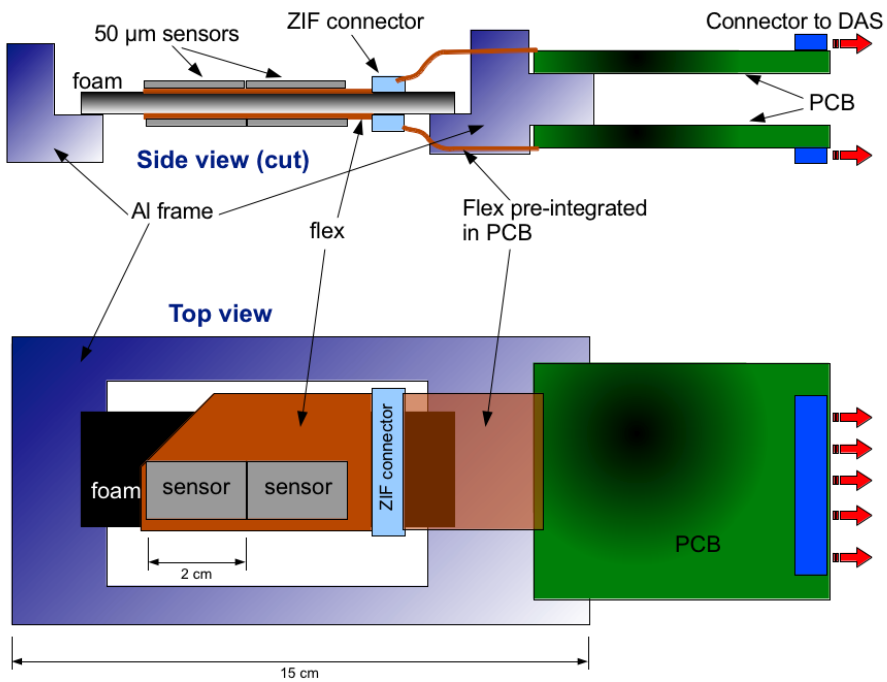

Figure 5.5 – Side and top view of the first PLUME prototype built in 2009.

called version-1 (V-1), was developed. Each module of the ladder was made of Kapton flex-cable with a thickness of 0.14 mm, using copper traces. They are denoted Optiprint-Kapton-Flex-cable (OKF), where Optiprint is the vendor of these flex-cable. It is the first version to embed six MIMOSA-26 binary output sensors working simultaneously on each side of the stiffener. The material budget is estimated to be 0.65 % of X_0 in the sensor's sensitive area. The aim of this prototype was to validate the operation of multiple sensors in a chain. Two ladders were tested in real conditions. The first one was tested with 120 GeV pions at CERN-SPS in 2011, while the second ladder was tested in April 2016 with up to 5 GeV positrons at DESY in Hamburg. The DESY test beam results are presented in chapter 8, while a specific study of the sensor's deformation observed at CERN is discussed in chapter 7.

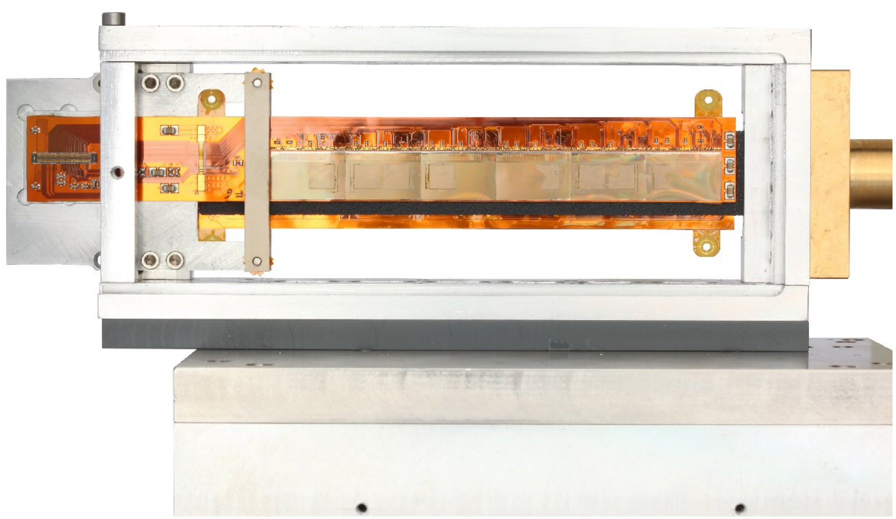

Figure 5.6 – Front view of the ladder version-1 made in 2010 in its holding box. On the left, there is the connector to the output board servicing, on the right a connection to blow air on the module. As this version was not made with a mirrored design, the flexible cables are not entirely overlapping and the SiC foam can be seen (in black here).

At the beginning of 2016, the third prototype versions were mounted but have not yet been completely tested. In fact, this new version is divided into two sub-versions: one using copper traces and the other one aluminum traces. Nevertheless, both sub-versions have a new design featuring reduced traces thickness to have a narrower flex-cable (18 mm width) adjusted to the sensors width in order to minimise the dead areas. The flex-design has slightly changed to have a mirrored geometry (figure 5.7) and a straight geometry in order to minimize the dead area too and have a better alignment

Layer	budget (% X_0)		
	V-0	V-1	Goal
Sensor	0.053	0.053	0.053
Flex-cable	0.524	0.150	0.034
Passive components	0	0.033	0.033
Stiffener (foam)	0.764	0.175	0.087
Total	1.926	0.654	0.334

Table 5.1 – Estimation of the material budget for the different prototypes of the PLUME ladder.

solution. The stiffener is made of a lower density SiC foam reducing the global material budget.

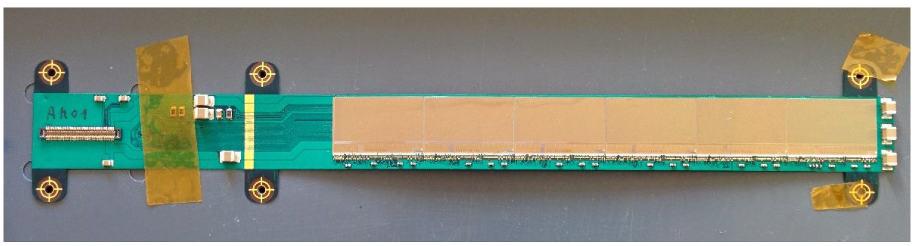

Figure 5.7 – Picture of the first mirrored module made with aluminum traces. The cable width is adjusted to the size of the sensor.

Table 5.1 summarises the material budget reached by the different prototypes.

5.2.3 Perspectives

Although the collaboration has shown their expertise to build light mechanical structures, more tests and optimisations have to be done. MIMOSA-26 sensors are not designed to match the ILC specs. The integration time of this sensor is 115.2 μs, whereas the bunch train last only 0.95 ms (bunch crossing spaced out by 337 ns), a new CPS with a faster integration time has to be integrated. Another problem of the MIMOSA-26 sensors is that they are not suited for a power pulsing. As a reminder, the principle of the power pulsing is to reduce the consumption of the sensor during the 200 ms dead time. Nevertheless, a power-pulsing study on a single Mi-26 sensor has been done and the results have shown that the nominal supply voltage of the

MIMOSA-26 can be lowered from 3.3 V to 1.85 V without losing the sensor's registers. The fake hit rate measured was close to the one obtained in normal conditions after the sensor reaches a stable operation. Moreover, the power consumption was reduced by a factor 6.3 [49].

A complete power-pulsing study of the whole ladder in the lab has to be done in order to make sure that the sensors are still behaving correctly. If the first results are comforting, the power-pulsing will be tested under real conditions with a high magnetic field. The impact of the Lorentz forces due to the coupling of the power-pulsing and the magnetic field is going to be studied, especially is this structure will induce unwanted deformations or vibrations.

The collaboration is considering to embed the sensors directly inside the multi-layer micro-cable [7]. The chips are glued on the first polyimide substrate layer, then the metal layer is deposited on top of it and the metal traces are directly connected to the chips pads. Then an insulator is added to the module. The advantages of this technique are, firstly, the direct connection of metal traces to the pads that avoid wire-bonding and can reduce, at the same time, the width of the module. And secondly, this structure has the advantage to apply the mechanical stress on the polymer wrapping, thus reducing it on the sensor.

A closer perspective for the collaboration is to integrate two ladders in the physics commissioning of the Beam Exorcism for A Stable experiment (BEAST) experiment at KEK.

5.3 Integration of CMOS sensors

The PICSEL group of the IPHC at Strasbourg is developing since 1999 CMOS sensors called MIMOSA for *Minimum Ionizing MOS Active pixel sensor*. They are semi-conducting pixel sensors based on the APS, an alternative to the CCD developed at the beginning of the 1990's by the imaging industry and widely used in nowadays commercial applications like smartphone's cameras. One particularity of the sensors developed by Strasbourg is that the various functionalities, such the sensitive area and the electronic layer where the signal is processed, are made of the same material. This device is called then Monolithic Active Pixel Sensor (MAPS) and the different layers are:

- A substrate providing a mechanical stability;
- An epitaxial layer which is the sensitive volume of the sensor;

- An electronic layer where are located the diodes collecting the charges and the micro-circuits processing the signal.

The motivation to use this technology or any other silicon sensor in particle physics is due to the minimum energy needed to create an electron/hole pair by a traversing particle. In silicon, this minimum energy is only 3.6 eV, while for a gaseous detector, it is close to 30 eV.

5.3.1 Charges creation and signal collection

The CMOS sensor can detect impinging particles thanks to their structure, but also to the interaction of particles with matter. When a charged particle is traversing a layer of matter, it loses energy via ionisations due to electromagnetic interactions with electrons and nuclei. Due to the size of a MAPS, it loses only a small fraction of its energy, and the distribution of the energy loss can be described by a Landau. A Minimum Ionizing Particle (MIP) creates 80 electrons per microns inside the silicon.

At the beginning, the microelectronic industry has insulated the transistors from the substrate using a high resistivity layer, called the epitaxial layer. The development of CMOS sensors was accelerated due to the properties offered by these semiconductors.

The CMOS sensors developed by the IPHC at Strasbourg are called monolithic MAPS sensors because the different layers of the sensor are made in one block of the same material, but with different doping. The structure of the sensor is a highly doped P+ substrate made of a moderate quality silicon. The crystal structure contains a lot of defects, hence the recombination rate of charge carriers is high. Above the bulk, a low-doped P- layer is grown. The silicon used has a good quality, thus the charge carriers have less chance to recombine. It is the sensitive part of the sensor and is called the epitaxial layer. On top of it, an N-well implant has the role of the charge collection. The interface between the N-wells and the epitaxial layer forms a P-N junction called a collection diode. A depleted area is created by this junction, on which the charge carriers are attracted. Nevertheless, this P-N junction is only one part of the pixel. Next to the N-well implants are sitting highly doped P-well in charge to reflect the charge carriers to the implants. The difference of doping between the bulk and the epitaxial layer is also used to reflect the charge carriers to the collection diode.

The typical doping concentration are 10^{15} at.cm^{-3} for the epitaxial layer, 10^{19} at.cm^{-3} in the substrate and 10^{17} at.cm^{-3} for the other layers. The doping concentration defines the size of the depleted region. For this doping concentrations, only a small region around the P-N junction is depleted, while the epitaxial layer is mainly undepleted. As no external voltage is applied to the sensor to increase the depleted region, the charge carriers created by crossing particles are thermally diffused into the epitaxial layer to the diode. Nevertheless, the different doping levels produce a built-in voltage defined as:

$$V_b = \frac{kT}{q} ln \left(\frac{N_{p+}}{N_{p-}} \right) i. \tag{5.4}$$

The built-in voltage depends on the Boltzmann constant k, the temperature T, the elementary charge q and the different concentrations doping $N_{p\pm}$ of the interface. Due to the different doping levels, the electrons are restricted to diffuse inside the sensitive volume, to be then guided towards a collection diode. One effect of the thermal diffusion is that the average path of the electrons in the epitaxial layer is longer than the one they would have in a fully-depleted sensor. Hence, the probability of recombination between an electron and a hole is increasing. Also, the charges tend to spread more around neighboring n-well. Therefore, the charge collection efficiency is lower than the fully-depleted sensor.

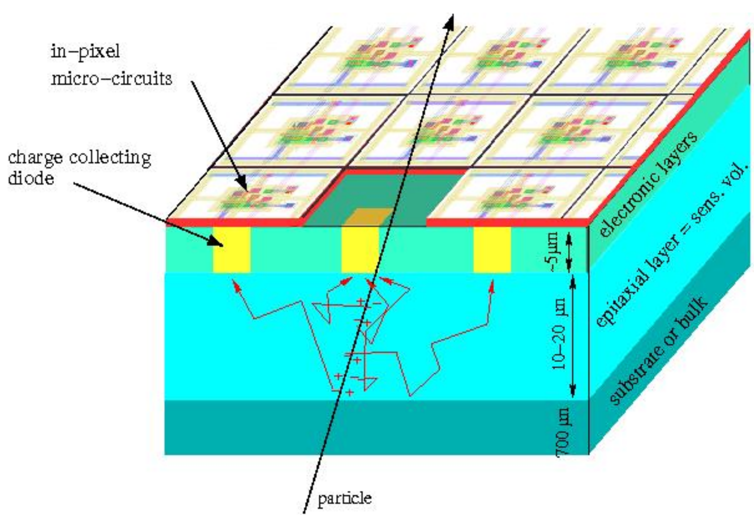

Figure 5.8 – Drawing of MAPS structure representing the different layers of the sensor and the path of charge carriers in the epitaxial layer.

5.3.2 Pros and cons of the technology

The CMOS sensors have several interesting properties. First of all, the fabrication cost is lower than other pixel technologies due to the industrial processes used to build the sensors. Therefore, many prototypes and bigger matrices can be built, while benefiting from the industrial experience. For example, the imaging industry has developed smaller and smaller grid size and a pitch size of ten microns can be achieved.

Secondly, due to the size of the depleted area, the charge carriers tend to spread more over neighboring pixels. On the one hand, the signal collected per pixel is smaller, but on the other hand, the reconstruction of the hit position with a centre of gravity algorithm is improving the spatial resolution. To give an idea, a binary output sensor with a pitch of 18.4 μm can achieve a spatial resolution better than 3 μm.

Thirdly, the distinct doping of the different layers is responsible for the reflection of the charge carriers to the collection diodes. However, only the interface between two different doped regions is responsible for this reflection. Figure 5.9 represents the principle of the charge collection at the interface between the substrate and the epitaxial layer. Thus, the substrate can be thinned down to few microns leading to a sensor with a thickness of 50 μm, while keeping the possibility to manipulate them. In this way, the material budget can be reduced down to 0.053 % X_0.

Nevertheless, the thickness of the epitaxial layer (usually between 10 and 15 μm) and the small depleted region (in the order of 1 to 5 μm) are responsible for a small charge collection. As a matter of fact, a MIP is creating 80 electron/hole pairs per microns, so the number of charges collecting by the diode is of the order of a thousand electrons. Hence, the signal created is only a few millivolts and low noise electronics have to be used for processing the signal.

CMOS sensors are sensitive to ionizing and non-ionizing radiations that degrade the sensor properties. The non-ionizing radiations are damaging the crystal structure of the epitaxial layers, creating defaults in the lattice. The recombination rate is increasing and reduces the signal collected. To avoid this effect, two solutions are possible. The first one is to reduce the size of the pixels in order to decrease the path of the particles from the epitaxial layer to the collection diodes. Nevertheless, a smaller pitch size induces a slower readout and the cost to build such sensor is increasing. The second solution is to increase the resistivity of the epitaxial layer to expand the depleted area.

The ionizing radiations are responsible for charges accumulation in oxides at the interface with silicon layers. The leakage current is increasing in the

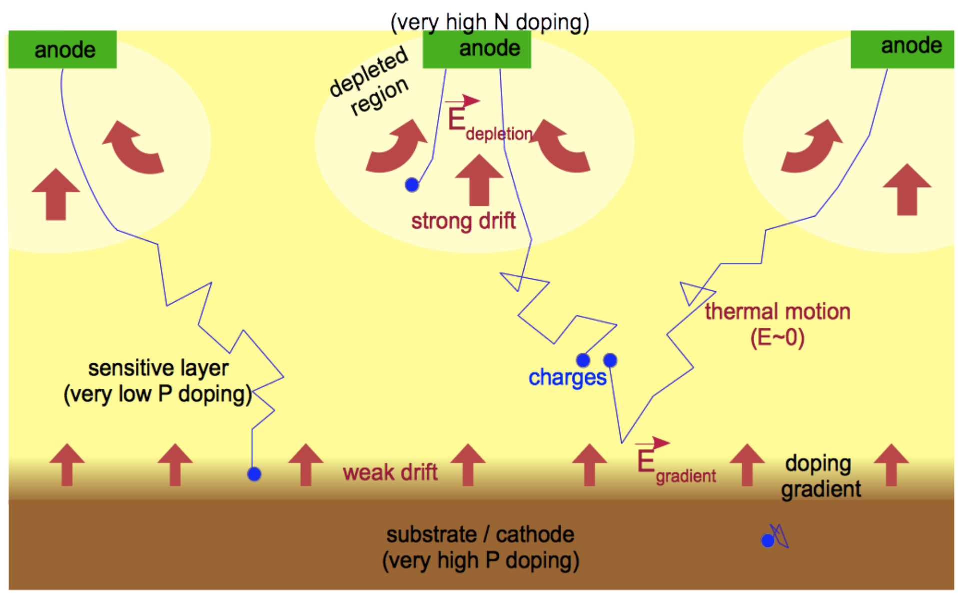

Figure 5.9 – Principle of charge collection in a MAPS. The difference of doping between the substrate and the epitaxial layers create a reflection region.

pixel and diode collection. To reduce the leakage current, smaller diodes can be used to reduce the impact of the leakage current but as it was explained before, the cost of fabrication is increasing.

5.3.3 Signal processing

If no charge is collected by the pixel, the voltage at the equivalent capacitor of the diode is evolving because of the leakage current inherent in the junction. The pixel reading can be done in two different ways, depending on the method used to minimise the leakage current effect. Currently, two pixel's architectures are used to compensate the diode's leakage current: the *3 Transistors pixel design*, mainly used in imaging, and the *self-biased pixel design*. The circuit diagram which is shown on figure 5.10 represents the two methods to design pixel.

The first one, presented on figure 5.10a, consists reinitialising the collection diode's voltage to a reference voltage thanks to a *reset* transistor, denoted M1 on the diagram. This method works in two steps. Firstly, the M1 transistor is closed and the charge of the equivalent capacitor C_d associated to the junction P-N, represented by a diode on the diagram, is slowly decreasing because of the diode's leakage current. During this phase, the pixel is sensitive and is read. After a time interval equivalent to the integration time of the sensor, the transistor M1 is opened to recharge C_d to its initial voltage. During this time, the pixel is not sensitive. While M1 is used for the reset, M2 is used as a pre-amplifier of the signal created by the diode and M3 link up the voltage to the output of the circuit. Although this compensation method is fast, it generates a dead time for detection between two readings.

Figure 5.10b depicts the *self-biased pixel design* method [25]. It is using a P-N junction (symbolised here by a diode mounted on the other side) coupled to the N-well implant to absorb the leakage current. The inverted diode is continuously compensated the diode's leakage current, thus the dead time vanishes. While no particle is crossing the sensor, an equilibrium appears between the leakage and recharge current. A particle going through the sensor disrupts this equilibrium. The charges collected by the pixel lead to a discharge of the diode's capacitor C_d, followed by a recharge of this capacitor thanks to the second diode to reach again the equilibrium. Nevertheless, if the recharge procedure is too fast compare to the integration time, the physics signal is masked and the passage of the particle is never notified. Even if the time interval to recharge the capacitor C_d is set properly, an important charge collection per pixel could disturb the recharge phase and the pixel will reach a stable level again only a long time interval of the order of 10 ms.

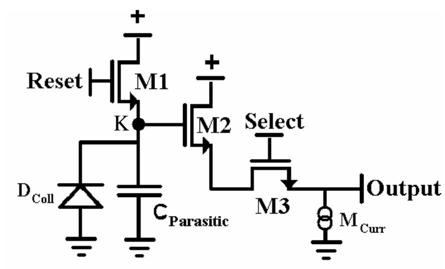

(a) Three transistors (3T) pixel design.

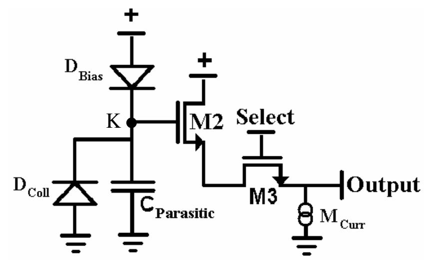

(b) Self-biased pixel design.

Figure 5.10 – Two different architectures of pixel.

Integration time and readout

For a non-depleted epitaxial layer, the charge carriers are mostly thermally diffused to the collection diodes. The time to collect these charges in a pixel is $\sim$ 100 ns, setting a maximal limit to read the signal. This integration time is not reachable due to other factors, like the pixel occupancy or the time needed to obtain the information of all the pixels. Also, a compromise to reach fast integration time has to be done. Faster is the sensor, more important is the power consumption in the electronic. Moreover, to reduce the integration time, a solution consists in increasing the size of the pixels. In consequence, the pointing resolution of the device is impacted. For the case of the ILC, the integration time is dictated by the pixel occupancy that should not be bigger than a percent, to stay in the using sensor's range and to be able to use the pattern recognition for tracking.

The first sensors developed were using an analog output. With this approach, the pixels were addressed sequentially and their output was multiplexing in one bus line. The advantage of such method is that the discrimination can be adjusted offline for each pixel, thus compensating the nonuniform response. Nevertheless, the integration time is depending on the operational frequency of the bus (usually 50 MHz) and the number of pixels contained in a matrix. For a sensor having millions of pixels, the integration time is then of the order of the millisecond. An analog output is then too slow for a ILC purpose.

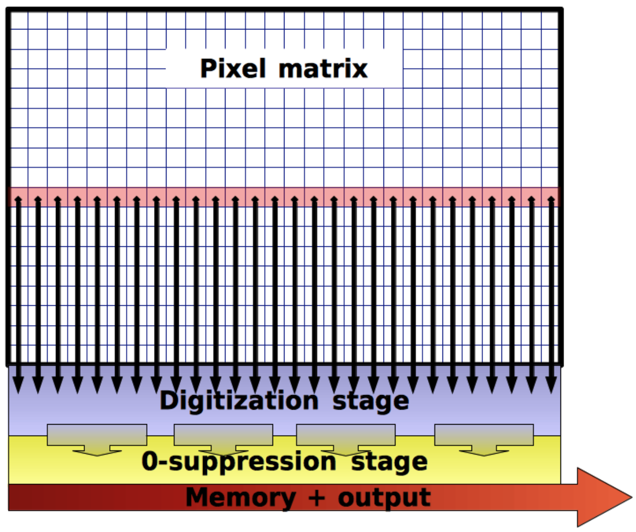

Figure 5.11 – Schematic operation of the parallel column readout.

To overcome this problem, an approach is to group the pixels in columns and to read them in parallel. Figure 5.11 depicts the principle of this method called *column parallel readout* or *rolling-shutter*. Instead of having one bus line for the whole matrix, each column has its own bus and a data sparsification logic is integrated on the periphery of the sensor. One row is read out between 100 ns and 200 ns, independently to the number of pixels contained in it. In consequence, a matrix containing thousands of rows has an integration time of $\mathcal{O}(100\ \mu\mathrm{s})$. Moreover, to increase the integration time an output memory is duplicated at the periphery of the sensor. Hence, when one line is read, the precedent one is processed by the micro-circuits at the end of each bus line of each column. To minimise the data bandwidth, only the pixels above certain thresholds are read thanks to discriminators coupling to a zero suppression logic, called Suppression de zéro (SUZE) [39]. In this way, only the address of the first pixel hit in a row and the number of the adjacent fired ones are stored. This memory is duplicated to be able to process one row, while the previous one is read out by the outside world. In order to increase the readout speed, two techniques are conceivable [73]. The first one provides elongated pixels in the vertical direction in order to reduce the number of rows, thus degrading the spatial resolution in the same direction. The second one consists of dividing the columns into two distinct parts, which have its dedicated output.

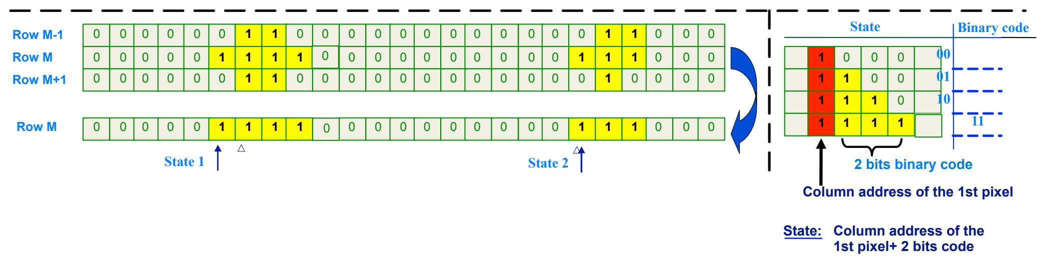

Figure 5.12 – Principle of the zero suppression logic.

Noise

An important figure of merits is the effective noise equivalent for one pixel. Many factors are driving this noise value and the different kind of noise is divided into two categories: the Fixed Pattern Noise (FPN) and the Temporal Noise (TN). The non-uniformity responses of the pixel in a sub-array is responsible for the FPN and is regarded as an offset between the pixel pedestals, which is subtracted from the pixel response to reduce the impact of this noise. The TN has different origins, as the shot noise, the pink noise or the thermal noise. The different operational phases to read the signal are contributing to the noise.

One contribution to the TN appears in the *3T pixel design* only during the reset phase. This noise arises when the transistor is open restoring the charge of the capacitor associated with the collection diode. It is dependent on the temperature and the diode's capacitance.

The second one is the noise during integration and is caused by statistical fluctuations of the leakage current (shot noise). Faster is the integration time, smaller is the shot noise contribution.

Finally, the third one arises from the readout, while the column switch and the source follower capacitors are working. This noise depends on the contribution of each capacitor.

To remove the FPN and the reset noise, a Correlated Double Sampling (CDS) is performed inside the pixel or at the bottom of the column. It consists to acquire two frames and to subtract the first one to the second one

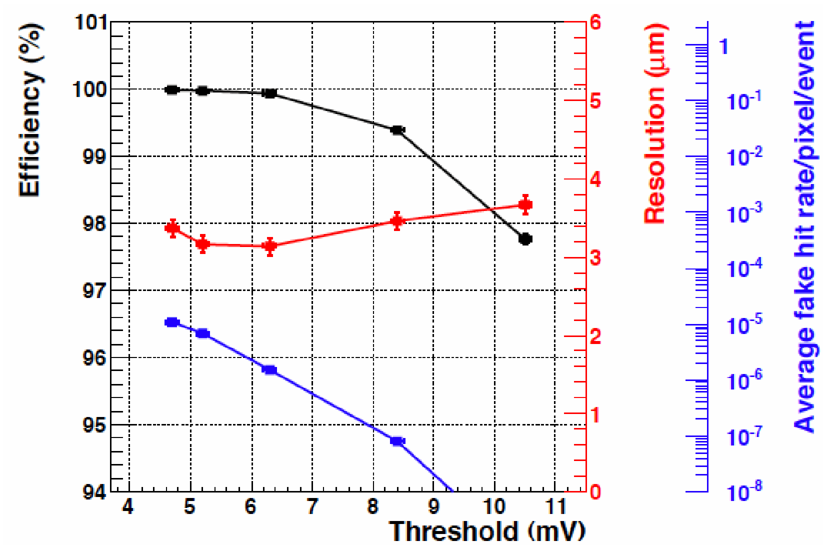

Figure 5.13 – Plots representing the efficiency, the fake hit rate per pixel and the spatial resolution as a function of the discriminator threshold. This results were obtained with minimum ionizing particles (pions of 120 GeV).

to search for possible signals. Chapter 6 describes the steps to characterise the FPN and TN and to select an appropriate Signal to Noise ratio (SNR) in order to minimise the noise contribution, and to find a range on which the sensor is working properly.

5.3.4 State of the art in high energy physics

The first full-scale digital sensor developed by the PICSEL group was the MIMOSA-26. They were designed to equip the reference planes of the EUDET beam telescope and are used since 2010 to build the PLUME prototypes. It is fabricated in the AMS 0.35 μm technology, and has a matrix containing approximately 6.6×10^5 pixels, distributed in 1152 columns and 576 rows. The pixel pitch is 18.4 μm and the sensitive area represents 21.2×10.6 cm^2. The readout of the matrix is ensured by a rolling-shutter working at 80 MHz frequency, hence the integration time is 115.2 μs. The signal produce by the charge collection inside the pixel is firstly amplified. Then, the CDS technique is used to subtract successive frames before to send the signal at the bottom of the pixel array, where the signal processing circuitry is placed. Analog to digital conversion is done, coupled to a second double sampling, in order to reduce the FPN. The output of the discriminators is then connected to a zero suppression logic, in which an output memory is duplicated to ensure a continuous readout. The signal is finally transmitted to the outside world. The architecture of the MIMOSA-26 is represented by a block-diagram on figure 5.14b. The power consumption is 1.1 μW/pixel and the sensor is thinned down to 50 μm in order to minimise the multiple scattering inside the volume. The performances obtained with a MIMOSA-26 are shown on figure 5.13.

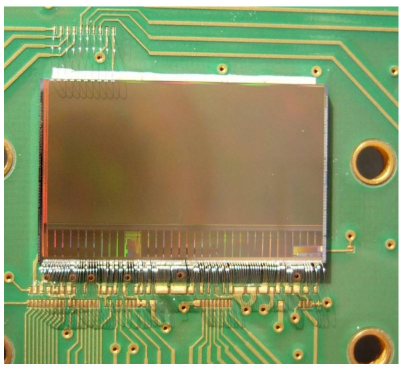

(a) Picture of a MIMOSA-26 mounted on a PCB.

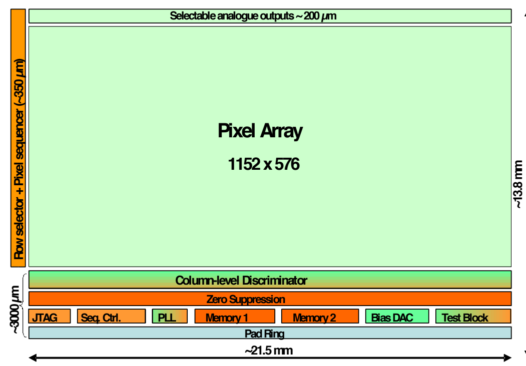

(b) Layout of the MIMOSA-26 matrix.

Figure 5.14 – Block-diagram and a picture of the MIMOSA-26

The PICSEL group has then developed digital output sensors for the pixel vertex detector at the STAR experiment at Brookhaven National Laboratory [71][19]. Figure 5.15 is showing a half-section of the STAR vertex detector (figure 5.15a) and a MIMOSA-28 bounded on a PCB (figure 5.15b). They are based on the architecture of MIMOSA-26 with some modifications. The matrix contains 960 columns and 928 rows for a pitch of 20.7×20.7 μm^2. The sensitive area is 19.7×19.2 cm^2, for an integration time of less than 200 μs. The sensor can reach a particle detection rate of 10^6 partices.cm^{-2}.s^{-1}. Finally, their power consumption is lower or equal to 150 mW.cm^{-2}. The spatial resolution obtained for ULTIMATE is less than 4 μm.

This chapter has depicted the purpose of the vertex detector for the ILD. Different technologies were introduced, to focus specifically on the CMOS sensors and their use in high-energy physics. The PLUME collaboration aims to integrate MAPS onto light double-sided ladders, in order to reach the requirements of the ILC. The collaboration has reach different steps to produce the first full-scale ladder, which have only a material budget of only 0.35 % X_0 and a spatial resolution better than 4 μm. The principle of

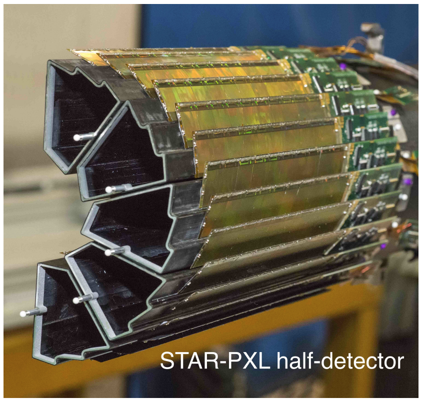

(a) Half part picture of the pixel vertex detector at STAR.

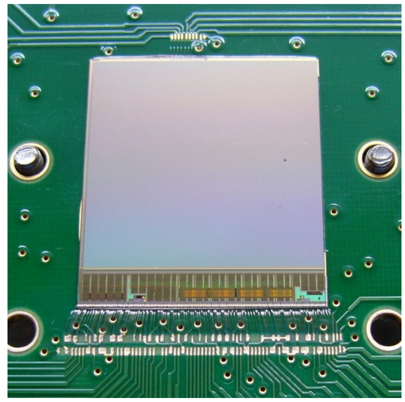

(b) ULTIMATE chip mounted on a PCB.

Figure 5.15 – Pictures of the STAR vertex detector and an ULTIMATE chip

the CMOS technology was presented. The next chapter is focusing on the electrical validation of this sensors mounted onto a PLUME ladder.

Chapter 6

Basic assessments

In chapter 5, an overview of the PLUME project was presented. Since 2010, the collaboration is building fully functionnal ladders and is trying to reduce the material budget down to 0.35 % X_0. Due to the six sensors working together and the huge amount of electrical lines to control and read the different sensors on a module, the ladders have to be carefully tested and validated in the lab before performing tests under real conditions at CERN or DESY test beam facilities. This chapter is introducing the different steps from the assembly procedure performed at Strasbourg (for the module) and Bristol (for a complete ladder), to the final tests to study the sensors response, and include electrical functionality tests at Hamburg.

Contents

6.1 PLUME assembly procedures

The ladders are built in two steps. Firstly, two independent modules are assembled at Strasbourg, then tested at DESY, afterward, they are shipped to Bristol where the modules are glued together on a SiC foam to form a PLUME ladder. The assembly procedures are introduced below, as well as the visual inspection between the mounting steps.

6.1.1 Module and ladder assembly

Module assembly

The module assembly is performed at the IPHC by the microelectronics group and is done in three steps. First of all, the passive components are soldered onto a flex-cable. Then, an epoxy layer with a thickness of 300 μm is applied under the connector side. Due to the force applied by pulling and pushing the jumper cable on the ZIF connector, the epoxy layer has the role to reinforce this area and to avoid the flex-cable to be damaged. The module is then placed on a metal jig to ensure its flatness using a vacuum suction. The next step consists of gluing the six sensors onto the flex. The positioning of the chips was used to be done manually, but a programmable robot which has a maximum mismatch alignment reaching approximately 20 μm is now used for this procedure. As the sensors are thin and fragile pieces, their are manipulated with a vacuum sucker. Few drops of glue are dispensed on the flex and then, the sensors are gently pressed one by one on top of it to be glued. Afterward, the glue is cured in an oven and the chips cannot be removed anymore. If a sensor is not working properly, it can not be replaced by a new one because the force needed to remove it might break the fragile flex-cable. On the worse case scenario, a new sensor can be glued on top of it, but this solution cannot be envisaged for a real ladder as it increases the material budget locally.

In order to avoid this situation, the sensors are probe-tested at the IK in Frankfurt, to select only the good ones before the module assembly. The final step consists of soldering the 540 wire-bonds (a single MIMOSA-26 requires 90 wire-bonds) using a semi-automatic machine. The wire-bonds can be protected by applying a glob-top epoxy. It has the advantage to offer a protection against moisture or contaminants, an electrically insulation and prohibits their movement during other manipulations (see section 6.1.2 for the utility of the glob-top epoxy). Nevertheless, it increases the material budget locally and if an electrical problem occurs, the wire-bonds can't be

Citation to a glob-top paper

disconnected. When the module is assembled, it is finally transferred onto a plastic sole, which has alignment pins. This sole helps to manipulate the modules, but also reduces the stress on the flex-cable, by holding it as flat as possible. During shipping, a plastic cover is screwed on top of the sole to protect completely the module.

Ladder assembly

The ladder assembly is performed by the Bristol team. It consists of two modules together on a spacer (SiC) and a bate (an aluminum plate). The operation is done entirely by hands. Each module is placed on a separate jig containing grooves and alignment pins to ensure the positioning, as presented on figure 6.1a. The sensitive side of the module is facing the jig to have an access to the rear of the flex-cable for the gluing procedure. Then, the foam is placed on one module below the sensors, while the bate is glued below the connector with an overlap on the foam (see figure 6.1b) The second module receives some glue on the backside before the jigs are assembled together. The glue is then cured for one day. The amount of glue needed for the assembly was studied carefully. The surface of the foam is irregular, so if not enough glue is used, the foam will not be glued on the module. On the other hand, using too much glue might stick the jigs together. When the ladder is finally ready, it is placed into an aluminum box used for shipping but also testing.

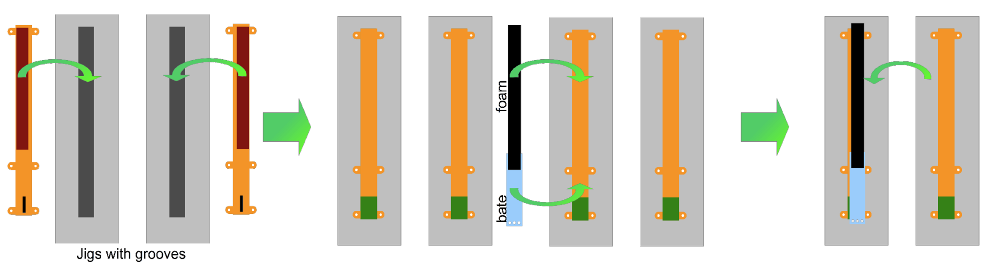

(a) **(b)**

Figure 6.1 – Drawing of the ladder assembly. The modules are first placed on the jigs, sensors facing the grooves 6.1a, then the foam and the bate are glued between the two modules 6.1b.

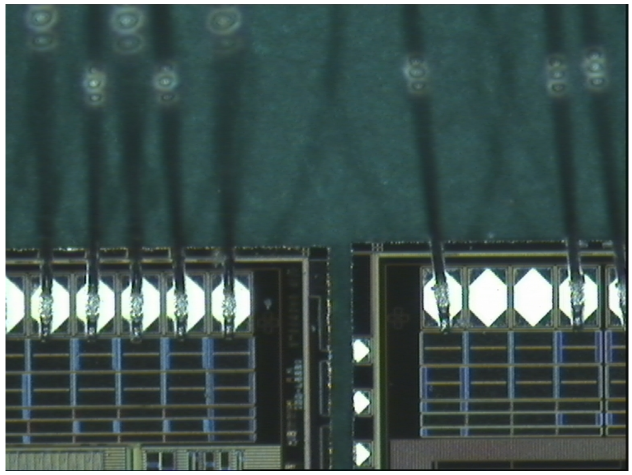

Figure 6.2 – Visualisation of the alignment. The distance between the two edges is $\sim 51\ \mu$m.

6.1.2 Visual inspections

As explain in section 6.1.1, the sensors positioning was performed firstly manually and later was switched to an automatic procedure. To tune properly the robot which is in charge of gluing the sensors on the flex-cable, the microelectronic group needs a position feedback. The modules are then inspected under a microscope to measure the gap between two sensors, and their position relatively to each other. The distance between the last pixel of a sensor to the neighboring one should be less than 500 μm, taking into account the 20 μm robot's mismatch. Figure 6.2 is a picture taken with a microscope showing the relative position of two sensors on the bottom of the matrix for an aluminum straight module. The gap between the two edges is $\sim 51\ \mu$m.

The visual inspection is also needed to check if the wire-bonds are correctly connected to the right sensor's pad, to verify that the gluing of the sensors on the flex-cable did not break the matrix due to some dust and also to control that the shipping of the module between the labs (for example between Strasbourg and DESY) did not damage it. The modules are fragile objects that have to be manipulated with care. Any wrong manipulation can damage severely the vital functionality. For example, figure 6.3 shows a picture taken with a microscope of crushed wire-bonds due to a falling cable on it. The sensitive part and the electronics were not damaged, but some wires were touching leading to a shortcut. Fortunately, the microelectronic group at Strasbourg was able to unbend the wires and repair the most damaged one. This module is fully operational and working correctly.

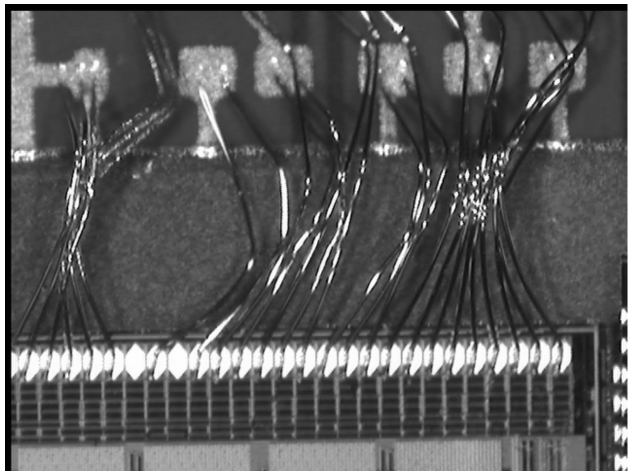

Figure 6.3 – Picture taken with a microscope showing crushed wire-bonds due to a falling cable. Some of the wire-bonds are in contact leading to a shortcut and a non-functional module.

6.2 Electrical validation

The electrical validation of a PLUME module or ladder is performed in two steps. The first one consists of checking that all the system controlling and powering the module is working. Then, the module is connected and its consumption, as well as the communication, are checked.

6.2.1 Auxiliary board

A module or a PLUME ladder is connected to the outside world by plugging a jumper cable on a ZIF connector at one edge of the module. This jumper cable is linked to an auxiliary board which powers the sensors of the module, but also pilots them and to transfer the data to the data acquisition system. This auxiliary card is connected to a power supply board which provides the nominal voltages needed by the sensors. The power supply board delivers the digital and analog voltages (V_{DD_D} and V_{DD_A} are set to 3.3 V using two independent potentiometers), the buffers voltage V_{CC} fixed to 3.3 V, as well for the temperature measurement diodes, a ± 5 V for trigger and a power pulsing signal. For the lab tests to validate the module, the power pulsing is deactivated by connecting this pin to the $+5$ V pin of the trigger. The clamping voltage V_{clp} used for the polarisation of the pixel has to be in the range $[2, 2.2]$ V. On the first version of the auxiliary board, it was provided by an external power supply, but the new version delivers the 2.1 V needed by using an I2C chips or a potentiometer (the user can select which methods to use thanks to a jumper). The auxiliary board is also connected to a computer in charge of the sensors' slow control. Two RJ45 are providing the Joint Test Action Group (JTAG) registers, as well as the start and reset signal. For a complete ladder, the two modules have to be synchronised and the clock can be injected by a clock distribution board. One RJ45 connector is dedicated to the JTAG slow control and the signals delivered are:

- **Test Data In (TDI)**: received the serial data input feed to the test data registers or instruction register
- **Test Mode Select (TMS)**: controls operation of test logic (for example, by selecting the register)
- **Test Clock (TCK)**: uses to load test mode data from TMS pin and test data on TDI pin at the rising edge, while at the falling edge, it is used to output the test data on the TDO pin.
- **Test Data Out (TDO)**: the output data feed the input data of the next sensor and the last sensor sends the information back to the computer

The second RJ45 connector is providing signal coming from the DAQ:

- **Clock**: has a rate of 80 MHz and is provided by the clock distribution board to synchronise two modules together
- **Start**: signal provided by the DAQ software to start and synchronise multiple sensors (the JTAG start works only for one sensor).
- **Reset**: reset the registers to default value.

The principle of the connection between the auxiliary board and the different components to operate one module is depicted on figure 6.4.

Before connecting a PLUME module to the auxiliary board, the voltages have to be set and the JTAG communication has to be checked on the auxiliary card. Two external power supplies are delivering 8 V D.C. to the power supply board and are giving an information on the consumption of the whole system. The empty auxiliary board has a current consumption about 350 mA. Then, the V_{CC}, V_{DD_d} and V_{DD_a} should be at 3.3 V, but only the two last voltages can be adjusted thanks to two potentiometers on the power supply board. The V$_{clp}$ is set to 2.1 V and should not be outside the range $[2, 2.2]$ V. The JTAG communication is verified thanks to a probe linked to an oscilloscope. The observed signals should be:

TDI:

TDO:

TMS: by default is fixed to 1 and change to 0 at every register selection

TCK: this clock is slower (30 kHz) than the 80 MHz needed by the sensors and is only dedicated for the slow control

Reset: by default is fixed to 1 and should change to 0 every time the reset is called by the JTAG software

Start:

Clock: Independently of the method used, the 80 MHz clock has to be correctly distributed along the auxiliary card

6.2.2 Smoke test

After the validation of the auxiliary board (and the power supplies switched off), the module can be linked to it via a jumper cable. The voltages applied to the device have to be adjusted again due to the dissipation inside the flex-cable and the jumper cable. The V_{DD_D}, V_{DD_A} and V_{clp} can be measured on different pads of the ladder: three pads are closed to the connector, while the three others are at the edge of the flex-cable, as seen on figure 6.5

Two versions of the jumper cable were produced, one very flexible with a high resistivity and the second one stiff with a low resistivity. The most flexible cable was not used because of an important voltage drop between the auxiliary board and the module, but also because of a wrong fabrication. After setting the voltages to the nominal value and plug in the module, a short-circuit happened. The auxiliary board tests were correct and were proofed one more time without the module. Then, a thermal camera was used to find if a sensor was responsible for the short-circuit. One sensor was hotter than the others, nevertheless, the wire-bonds were correctly assigned. The problem was coming from a short-circuit between the V_{DD_D} and the V_{clp}. By passing this two lines on the jumper cable and by connecting them directly to the module, the short was gone. Instead of this flexible jumper

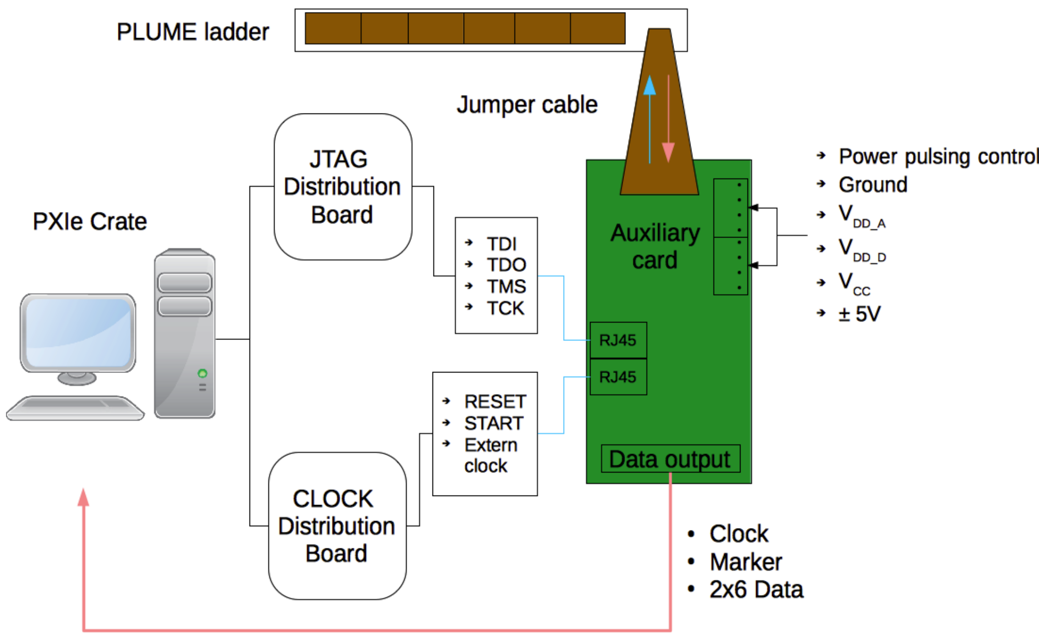

Figure 6.4 – Sketch of the PLUME connection.

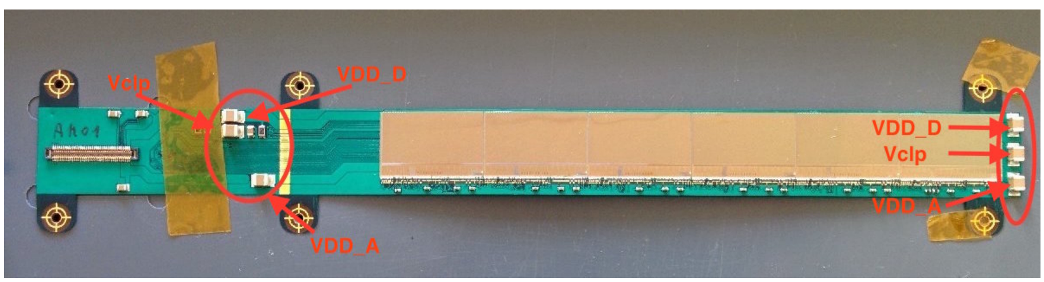

Figure 6.5 – Picture of a aluminum mirrored module with the points of measurement for V_{DD_D}, V_{DD_A} and V_{clp}.

cable, a stiffer one was used. Nonetheless, any movement of the auxiliary board causes a too important stress on the connector and on the flex-cable. To avoid any damage, a support was built to hold the auxiliary board and the module on the same frame, thus reducing the risk to break anything.

The module consumption is checked at every JTAG steps to make sure that no short-circuit occurs. Right after powering-on the system, the six sensors are starting in a random state and the consumption at this stage can not point out any electrical problem. After the reset of the registers, the total consumption should be around 33 mA. Then, the registers are loaded and the consumption should be around 750 mA. They are read-back by the JTAG software, which indicates if errors occur. If during the reading step no error was discovered, the sensors can be operated and their consumption should be around 1300 mA.

An inspection of the output with an oscilloscope is performed to check the slow control and to estimate the response of the sensor. For the normal mode data format with SUZE enable, the output data of the last frame is sparsified and transmitted during the acquisition of the current one. The information provided by the MIMOSA-26 is contained in four output lines. The first output line corresponds to the *clock* which is always running even if the data transmission is finished. Its rate depends on the clock rate register. For the normal output mode, it is 80 MHz. The second output line is the *marker*, which is available in all mode. It is set during four clock's rising edge cycle and might be used to detect the beginning of the data transmission. Then, the two last output lines are dedicated to the data. They contain multiple information. First of all, the beginning and the ending of the data transmission is determined by the *header* and *trailer*. They can be used to detect a loss of synchronisation. They corresponds to 2×16 bits (*header0-header1* and *trailer0-trailer1*) and are totally configurable through the JTAG software. The *header* is followed by the *frame counter* which corresponds to the number of frames since the chip was reset. The information is separated into two words (*FrameCounter0* corresponding to the least significant bit and *FrameCounter1* corresponding to the most significant bit). Then, the *data length* gives the number of 16 bits words of the useful data. The useful data is split into *states/line*, which contains the address of the line which has a hit and an overflow flag if the number of states is bigger than the memory limitation. It is followed by the *state* giving the number of consecutive hits and the address of the first column. Finally, the *trailer* is ending the data transmission followed by 32 bits of zero. Figure 6.6 is a picture of an oscilloscope output of a MIMOSA-26 data output. From the top to the bottom, it shows the 80 MHz *clock*, the four clock's cycle *marker*, the *data0* and *data1* with the *header* and the *frame counter*. More information about the MIMOSA-26 can be found in the MIMOSA-26 user manual [43].

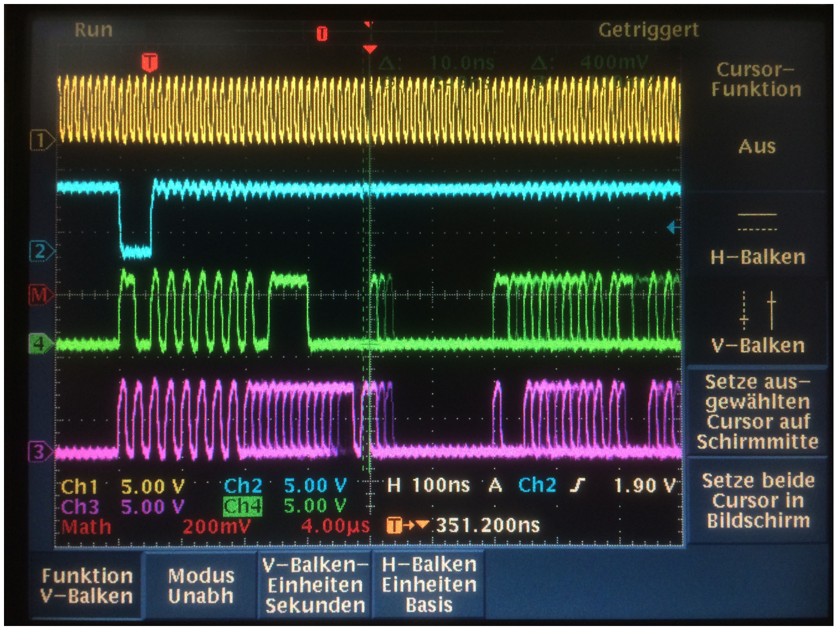

Figure 6.6 – MIMOSA-26 output from oscilloscope. The top yellow line corresponds to the clock, the blue line below to the marker (which last 4 clock cycles), and the green and purple line are the data output containing the hit information

6.2.3 JTAG communication

After adjusting the voltages and looking for any short-circuits, the next step is to control the JTAG communication for every sensor. As in the PLUME module, all the sensors are synchronised, only the *clock* and *marker* from one sensor is read back. On the oscilloscope, the trigger is set on the *marker*. The sensors are configured in the normal mode data format (80 MHz with zero suppression output) and the output is checked in three steps. First of all, the sensor is reset, the registers are loaded and read back and then the start signal is sent. Through the JTAG software, the *header* and *trailer* are modified several times and are checked thanks to the oscilloscope. Then, the discriminators' response is visualised, specifically to find pixels always sending data even if the discriminators are closed. The number of defective pixels and their position is then estimated. After that, an estimation of the threshold discriminator values to get few hits are determined and the response is then checked. Nevertheless, using light to estimate the response of the sensor can impact the pixels' baseline and modify the normal behavior of the matrix. For example, instead of sending more information, the pixels are less responsive. Thus, using a radiation source is a better solution.

6.3 Noise measurements

In chapter 5, the principle of the CMOS sensors is described and the noise of this technology is discussed. As a reminder, the two noise contributions are the Temporal Noise (TN) and the Fixed Pattern Noise (FPN). The FPN is determined as an offset to subtract from the pixel response to reduce its non-uniformity response, while the TN is coming from the contribution of different noises during the reset, the integration and the readout of the pixel. These noises have to be measured in the lab in order to find the optimum configuration to detect physics signal and reduce the noise impact on the measurement.

6.3.1 Characterisation bench

The noise is estimated with a bench of characterisation composed of a National Instrument PXIe crate equipped with a 6562 digital card, two power supplies, a power distribution board, an auxiliary and a JTAG card, as well as the module to test. The procedure described here is applied to a single MIMOSA-26, or a PLUME module, as well as an MIMOSA-28 sensor. Nevertheless, the data acquisition software used during the characterisation is slightly different to match the clock speed, depending on the sensor technology. The four data outputs are connected from the pins on the auxiliary board to the digital card thanks to a National Instrument spider cable. Firstly, a test pattern, which loads automatically a JTAG file for this test, is done to read the *header* and *trailer* during several frames with a determined data length. It has been observed that the *clock* output cable has to be 80 cm longer than the three other cables to ensure the synchronisation on the rising edge. If this is not done or if one of the cables has a wrong polarity, the software is not able to read the *header* and *trailer* and the characterisation can't be done.

Then, the sensors are configured in the discriminator output mode. The zero suppression mode is bypassed, pixels and discriminators are in normal mode (the whole matrix read in 115 μs), but the readout frequency is lower (10 MHz) via two LVDS output pads. The control of the discriminators is divided into four sub-matrices, each containing 288 columns. Thus, for one sub-matrix a threshold value in DAC units in the JTAG software is driving all the discriminators, depending on a baseline value. For one line, usually one located in the middle of the matrix, its baseline response is studied to find the "middle-points" by looking for the threshold of each sub-matrix, in which the discriminators are reaching a half activation. When this "middle-points" are determined, the homogeneity of the matrix is checked, as shown on figure 6.7. Due to the structure of the sensor, the homogeneity is not perfect and some dispersions in the discriminator response are observed between the beginning and the end of a sub-matrix. Moreover, to reduce this dispersion, the reference baseline, and the clamping voltage have to be adjusted.

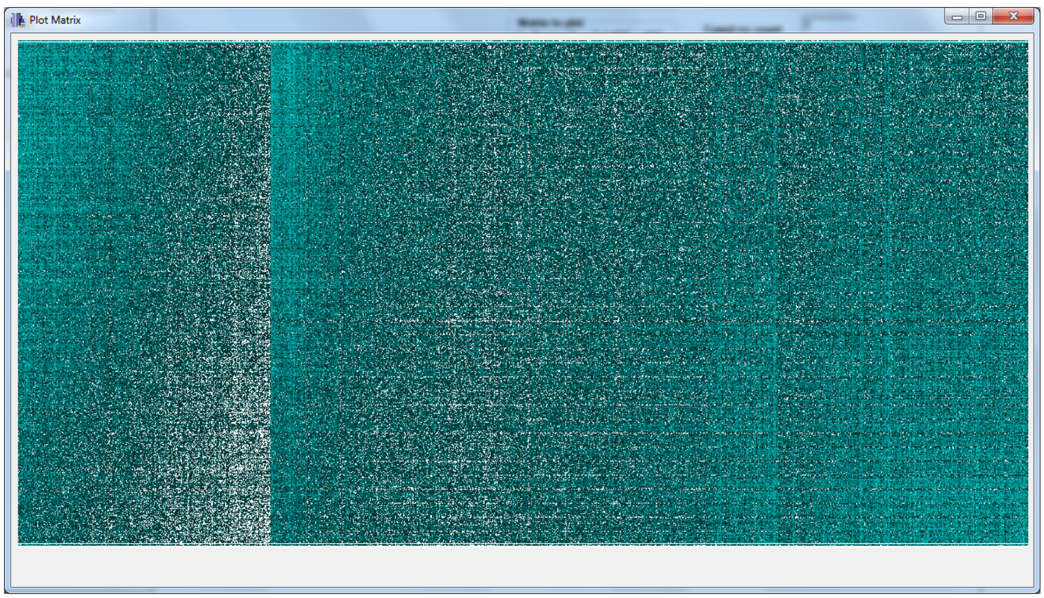

Figure 6.7 – Matrix response for the discriminators half activated.

Afterward, the thresholds are set to the lowest and highest value to look for defect pixels in the matrix. On the one hand, few pixels can be always activated even if the discriminators were closed. Figure 6.8 depicts the matrix output for all the discriminators closed. Therefore, a line is always activated, as well as few pixels in a column and they are increasing the fake hit rate of the matrix. A solution exists to disconnect some discriminators in order to reduce the noise of defect columns thanks to the JTAG program, nevertheless, no solution during the sensor programming exists to remove the defect lines. On the other hand, few pixels can be always deactivated even if the discriminators are completely opened, thus, they are not able to detect any physics signal. This behavior is represented on figure 6.9 and no solution exists to make them working properly.

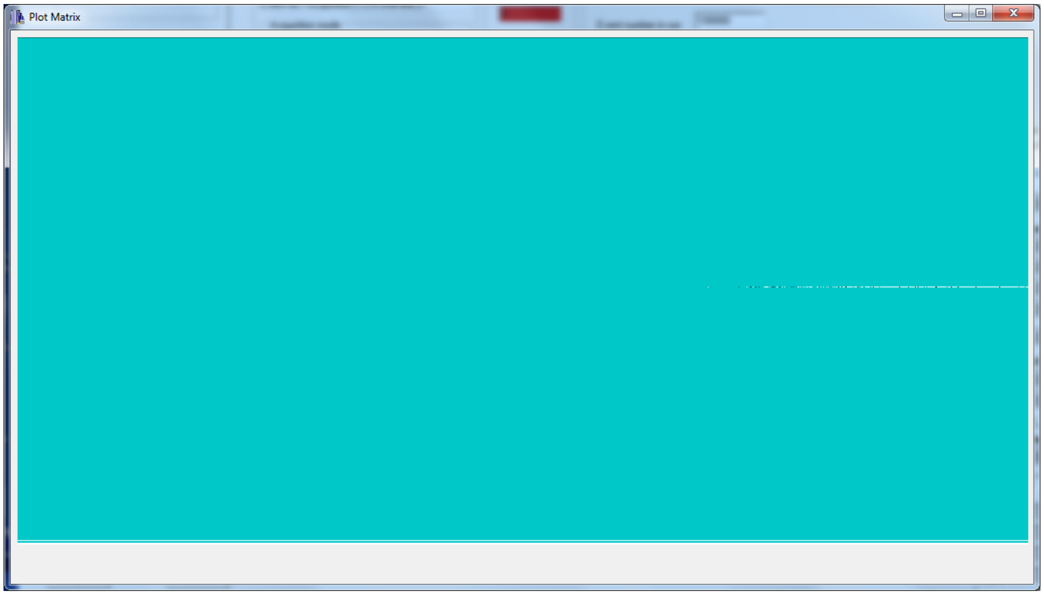

Figure 6.8 – Matrix response in discriminator mode, where all the discriminators are opened. On the right of the matrix, one line is not working correctly and some pixels are never activated

6.3.2 Threshold scan

The noise performance of the sensor is determined through a threshold scan around the "middle-point" found before. This consists to record the normalise response of the discriminators or the discriminators and the pixels for different threshold values. For the first possibility, an external voltage is injected into the discriminators, while the matrix output is disconnected. Only the noise contribution coming from the discriminator is thus determined. In this work, the noise performance results presented were done without injected an external voltage, but rather with the sensitive system connected to the discriminators. Usually, 29 runs containing between 50 to 1000 are stored. The files created are used to firstly, build a configuration file containing the DAC values of each sub-matrix for the different thresholds applied. The threshold is here defined has the voltage applied to the discriminators. Afterward, this file is analysed and converted to create an output file containing a hit average picture of each sub-matrix for each step. Then, a macro based on C++

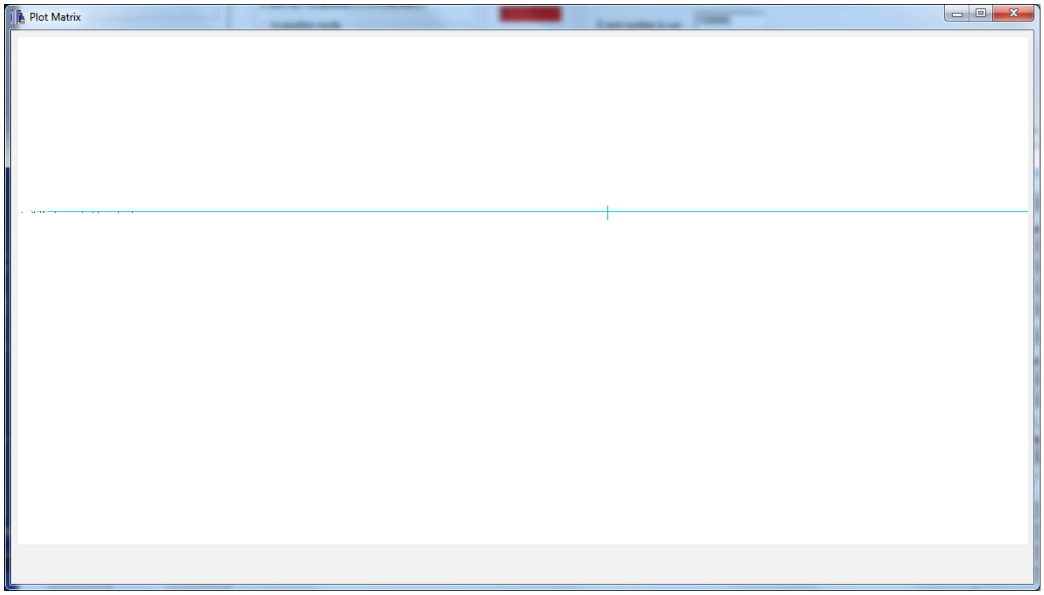

Figure 6.9 – Matrix response in discriminator mode, where all the discriminators are closed. One line of pixels is always activated, as well as few pixels in the same column. This will increase the fake hit rate of the sensor.

and ROOT framework is reading the hit average picture to plot the transfer function, also called "S" curve, as represented on figure 6.10. It shows the normalised response of the 288 discriminators and the pixels contained in this sub-matrix as a function of the threshold applied in millivolts. The temporal noise of each pixel is calculated from the derivative of the "S" curve and is represented here in the left plot of figure 6.11. The mean value of the distribution obtained the mid-point threshold of a pixel. The dispersion of the mid-point threshold corresponds to the fixed pattern noise, represented on the right plot of figure 6.11.

The plot on the left in figure 6.11 represents the temporal noise, while the right one represents the fixed pattern noise. The systematic offset of the discriminator is extracted from this measurements (the mean value of the temporal noise, the mean value and the sigma value of the fixed pattern noise). To calculate the discriminator thresholds of each sub-matrix for a given SNR, the total noise is determined as:

$$\text{Total noise} = \sqrt{<\text{TN}>^2 + <\text{FPN}>^2}. \tag{6.1}$$

For a given S/N cut σ, the thresholds are determined by:

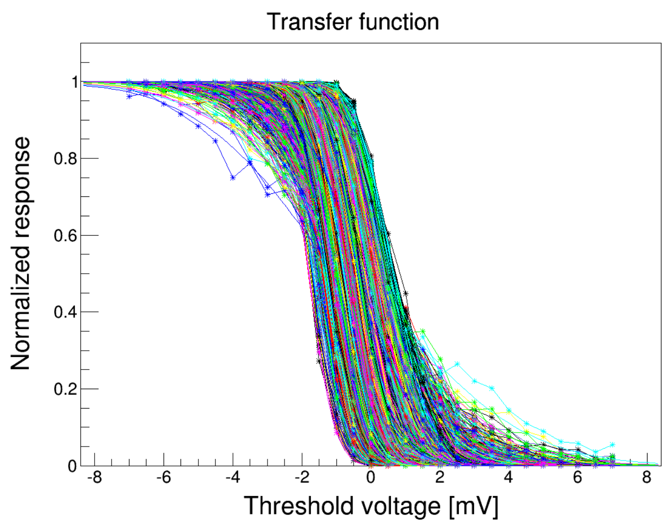

Figure 6.10 – Pixels response of a threshold scan around the middle-point of discriminators for a sub-matrix.

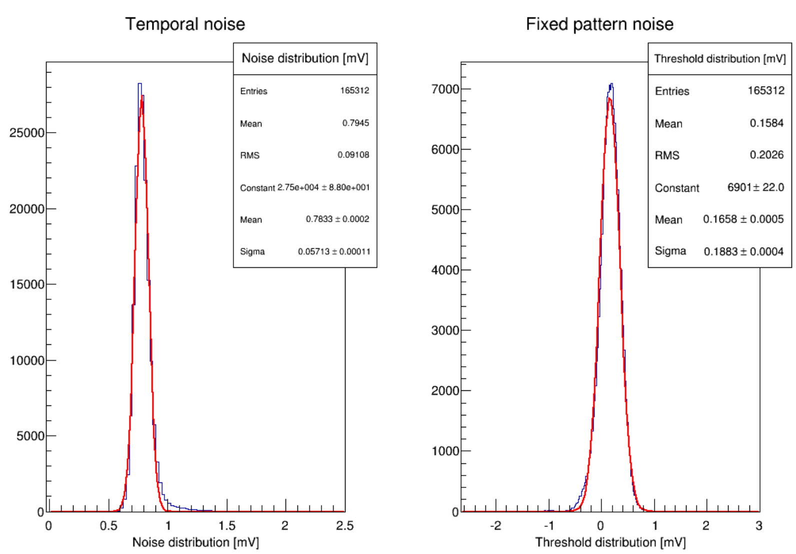

Figure 6.11 – Noise performances of a sub-matrix for the discriminators and the pixel array output. The temporal noise is plotted on the left plot, whereas the fixed pattern noise is represented on the right plot.

$$\text{Threshold (mV)} = \text{Total Noise} \times \sigma + \text{offset}. \tag{6.2}$$

This is converted into the DAC values by taking into account the DAC offset and the DAC slope, which is assumed to be 0.25 mV:

$$\text{Threshold (DAC)} = \frac{\text{Threshold (mV)} - \text{DAC}_{\text{offset}}}{\text{DAC}_{\text{slope}}}. \tag{6.3}$$

6.3.3 Noise measurements

Once the thresholds are defined for the different cuts, the fake hit rate of the matrix, as well as the detection homogeneity is determined. A quick step consists of using the DAQ software and acquiring ten-thousands events in the dark to determine the noise qualitatively. The fake hit rate per event per pixel is then considered as:

$$\text{F.H.R} = \frac{\text{Number of hits}}{\text{Number of events} \times \text{Number of pixels}}. \tag{6.4}$$

Figure 6.12 is representing the accumulation in the dark of ten thousand events for a threshold five times bigger than the noise. The measured fake hit rate was below 10^{-4} hits/pixel/events.

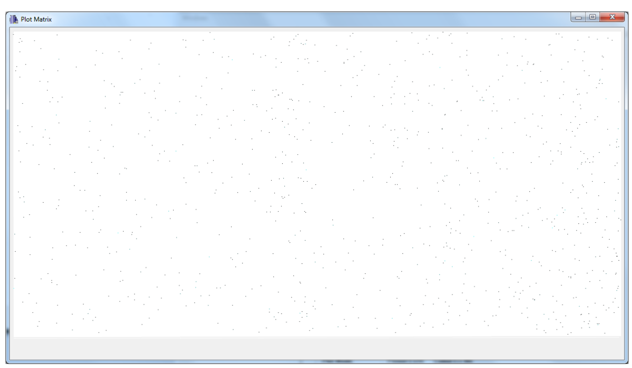

Figure 6.12 – Accumulation of 10k events at a thresholds of 5 times the noise acquired in the dark.

Then, an iron 55 source is used to control the homogeneity of the thresholds determined before. Figure 6.13 represents the accumulation of ten thousand events for a threshold five time bigger than the noise with an iron source on top of the sensor.

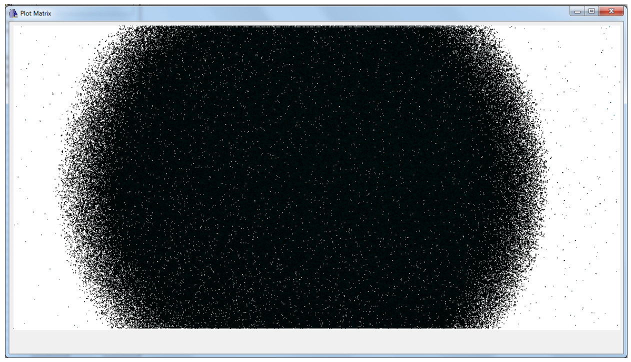

Figure 6.13 – Accumulation of 10k events at a thresholds of 5 times the noise with ^{55}Fe radiation source.

Finally, in order to validate the sensor, the acquisition system used during the test beam is used to calculate quantitatively the fake hit rate. The auxiliary board is connected to a Flex RIO board instead of the digital card. The test beam DAQ software developed by the IPHC is using a LabVIEW interface for the run control. It provides several useful information, such as the number of events acquired, the *header*, the *trailer* and the *frame counter* of the sensor. This helps the user to know if the acquisition is running properly. If the *frame counter* is different for each sensor, this points out a loss of synchronisation during the acquisition. Also, a different *header* or *trailer* such as the ones set in the JTAG software might point out a wrong connection. A second software is used to store the data into three files: a parameter file containing the run number, the event number, an index file and a binary file containing the raw data. Two acquisition modes are available. The first one, used in test beam, acquires data only when a trigger is sent. The second one, stores all frames regardless the trigger status. This acquisition is the one used in the lab, as only the noise of the sensor is measured.

Several runs containing each one million events are acquired for different thresholds. The data stored are analysed with a software developed by the IPHC and is called TAPI Analysis Framework (TAF) [45]. It is based on C++ and the ROOT framework. The software reads the information of the hit pixels, reconstructs the clusters of hit pixels and in the case of a test beam is able to reconstruct tracks from the hit information.

A method is used to determine the fake hit rate with respect to the number of pixels hit per event. From the distribution shown on figure 6.14, which represents the number of pixels fired per event, the average fake hit

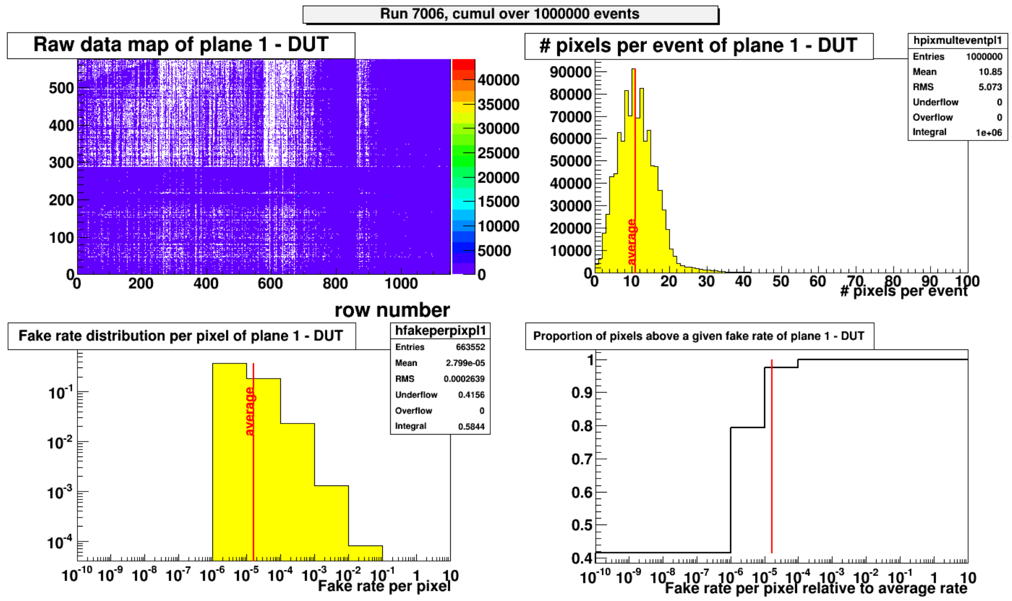

Figure 6.14 – Results of the fake hit rate measurement for a threshold three times bigger than the noise. The top left plot represents a raw picture of the million events accumulated over the whole matrix. The top right one is the distribution of the number of pixels hit per event. The bottom left plot is the fake hit rate per pixel distribution, while the bottom right one is the fake hit rate relative to the average rate distribution.

rate is calculated as the mean of this distribution divided by the total number of pixels contained in the matrix. The error on the measurement is then the root mean squared of the distribution divided by the number of entries and the number of pixels inside the matrix. This calculation is done for different thresholds and figure 6.15 represents the average fake hit rate per pixel per event as a function of the threshold for one sensor of an aluminum module. The results are matching the expected behavior for a standalone MIMOSA-26 sensor as shown in figure 5.13.

6.4 Conclusions

The assembly procedures and the tests performed in the laboratory were introduced along this chapter. Only the results for one sensor were presented. Nonetheless, all the modules have a same behavior as the one expected for one single MIMOSA-26. So far, for the new PLUME versions which have

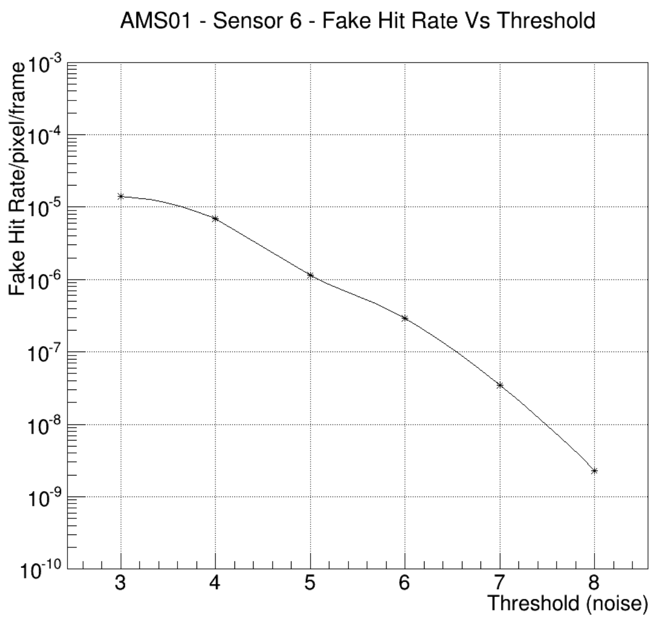

Figure 6.15 – Distribution of the fake hit rate per pixel.

a narrower flex-cable and which should embed only 0.35 % of the radiation length, different prototypes were built. The first ladder using copper module was assembled in January 2016. New ladders are currently being built and the collaboration is expecting to test them in the DESY test beam facility in November. Nevertheless, the aluminum ladder seems to be more challenging to build. The three first mirrored versions produced have a connector problem, that could have been damaged by plugging and unplugging the jumper cable. This problem did not occur with the copper mirrored versions and this might come from a more fragile flex-cable. Ideally, each module should have is own jumper cable and this should not be disconnected. Nevertheless, for shipping them, there is no other solution. The collaboration is thinking of a tool which will reduce the stress applied to the connector.

The next chapter deals with the tests performed in real condition at the CERN-SPS facility with the PLUME-V1 prototype in 2011.

Chapter 7

Deformation studies of a ladder under the test beam

The first full-scale prototype which embeds twelve sensors glued on a copper flex-cable and a 8 % density SiC foam was tested in November 2011 at CERN-SPS facility with a pions beam of 120 GeV. The motivations to perform such a test in real conditions are first, to make sure that the ladder is working properly. Secondly, to verify the response homogeneity of each sensor. Finally, it has to prove the benefits of a double sided measurement. This chapter does not aim to present fully the test beam campaign and all the results but to focus on a specific study of the ladder's deformation observed during the alignment procedure. More results about this test beam are presented in Loic COUSIN's thesis [54]. This chapter will present the test beam facility, as well as the experimental set-up. The alignment procedure is explained and some results for the ladder positioned in a normal incidence, as well as the ladder tilted in one direction, are discussed. The second part of the chapter will focus on the deviation observed during the alignment and will discuss a method to overcome these deformations. Finally, the benefits of double-sided measurements will be introduced.

Contents

7.1 Test beam of the full complete PLUME ladder at CERN

7.1.1 Test beam facility and beam test set-up

The test beam was performed at CERN-SPS in the North hall on the H6 beam line [12]. Negative pions with an energy of 120 GeV were used. The spill structure was 9.6 s with a dead time of 45.6 s. The bench set-up is composed of a telescope equipped with four standard MIMOSA-26 sensors, thinned down to 120 μm and used as reference planes. It is made of two arms and the distance between two sensors of the same arm is 5 mm. The reference planes are stabilised to a temperature of 15°C and a 8 sigma S/N threshold cut was applied. The PLUME ladder is positioned between the two telescope arms for the tests. For the rest of the chapter, the ladder is called the Device Under Test (DUT). The bench has also 7×7 scintillators used for triggering the data. Most of the runs were taken with a trigger frequency between 2 and 8 kHz, except for two days where the frequency was oscillating between 1 and 1.3 kHz. The acquisition system is limited to eight inputs and four of them are used by the telescope. Thus, only four sensors of the DUT were connected to the acquisition, two on each side. The temperature of the DUT was stabilised thanks to an air flow cooling system, provided by a fan.

7.1.2 Cartesian coordinate systems

Although the sensors have their own ID to distinguish them during the analysis, the position of each plane has to be known exactly. Two Cartesian coordinate systems are then defined. The first one is the global one and is determined by the position of each sensor of the telescope. The notation used for this coordinate system is (x, y, z). The x-axis corresponds to the horizontal direction, the y-axis is the vertical one and the z-axis is along the beam direction. The origin $(0,0,0)$ of the system is usually defined by the position of the first plane hit. The second coordinate system is the local one and is determined by a single sensor. To differentiate this reference system to the other one, the (u,v,w) notation is used. The u-axis corresponds to the pixel rows, the v-axis is along the pixel columns and the w-axis is perpendicular to the matrix. The origin of the local system is the center of the pixel matrix. Figure 7.1 summarises the definition of the two coordinate systems.

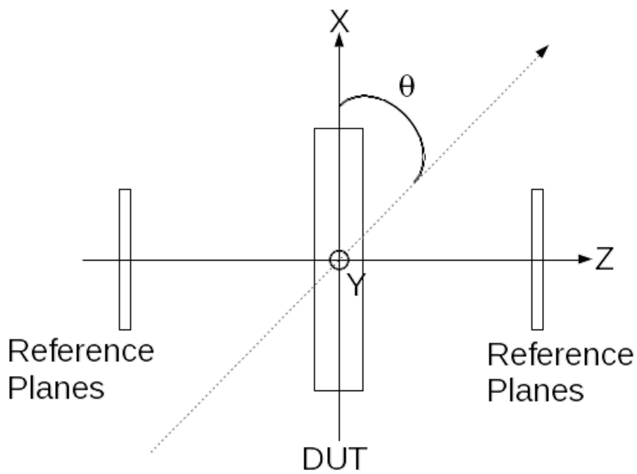

Figure 7.1 – Drawing of the laboratory coordinates.

7.1.3 Measurements

The prototype validation was done under several conditions and with three different geometrical configurations. On the first one presented on figure 7.2a, the DUT is parallel to the telescope planes and the beam is hitting the device in a normal incidence. The ladder is placed in between the two arms. The middle of the foam is at equal distance from both inner telescope planes. For the second configuration, as shown on figure 7.2b, the distance between the telescope planes are the same, but the DUT is tilted between 28 and 40° along the y-axis. Runs with a larger angle (60°) were done. Due to the PLUME box's size, the cabling for the acquisition, the air cooling system and the design of the telescope stage, limiting the spacing between the two arms, the DUT was placed behind the two arms, as presented on figure 7.2c. For both configurations, different parameters were modified. The thresholds were set to 5 and 6 mV, different sensors were aimed and the air flow speed was set to 3 $m.s^{-1}$ and 6 $m.s^{-1}$.

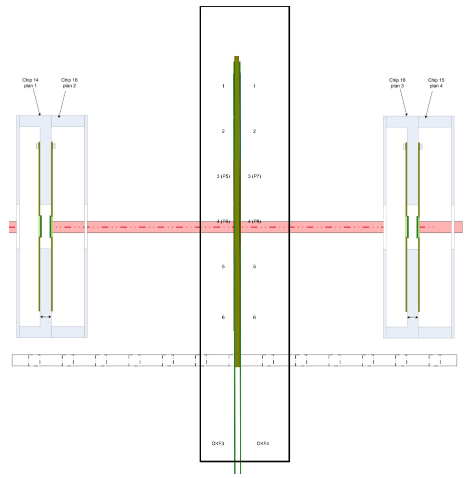

(a) Configuration for normal incidence with respect to the beam direction.

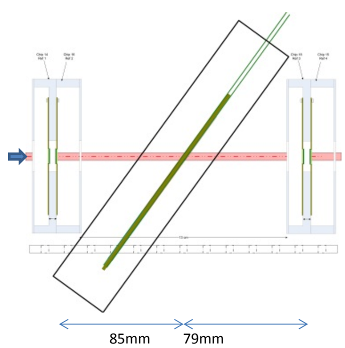

(b) Configuration for an angle between 28 and 40°.

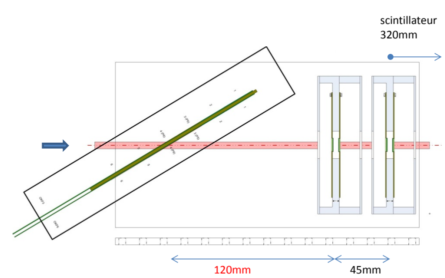

(c) Configuration for an angle of 60°.

Figure 7.2 – Top view sketches of the test beam configuration for different ladder positions: 7.2a is for normal incidence, 7.2b and 7.2c are for tilted ladder.

The analysis and the results shown in the following sections were performed with TAF, the analysis software developed by the IPHC and presented in chapter 6.

7.2 Spatial resolution studies

One of the measurements performed during the analysis is to determine the pointing resolution of the sensors on each side of the ladder. As the sensors used are well-known, the performance of the ladder should be similar to the one expected. Any deviations on the pointing resolution or the efficiency might point out an unexpected impact of the mechanical structure or the flex-cable design over the whole system. The alignment steps to obtained the pointing resolution of the ladders are explained below for different run configurations.

7.2.1 Normal incidence track

For each event, the acquisition is recording the position of the pixels hit, the frame number, as well as the sensor ID. The binary file created contains no information about the relative position of each sensor. To perform an analysis, the telescope planes have to be aligned each other. The hits information of every plane is combined in order to create tracks. A track corresponds to the path of a particle through the system. Thanks to this information, the tracks are then compared to the hits position on the DUT to give some information, such as the detection efficiency (the ratio of tracks matched to the hits on the DUT) or the spatial resolution (minimum distance to distinguish two incoming tracks).

The alignment procedure is done in two steps: firstly the telescope planes are aligned to minimise the mismatch of particles' tracks and to improve the tracking resolution. Afterward, the DUT is aligned with respect to the information provided by the reference planes and then, the analysis itself is performed. Although the position of each sensor is measured during the test beam with a precision of the millimeter, for the analysis, a precision of the micron level has to be achieved. Three degrees of freedom were taken into account for the alignment here: two translations for the x and y-axes and one rotation around the z-axis. The z position is determined by the position measured during the test beam campaign and is not considered as a free parameter due to the beam used.

Alignment procedure and telescope alignment

Firstly, the data acquired during the test beam are processed to extract the signal and the hit information. For each frame, the position of the pixel(s) having a signal above the discriminator threshold is stored and assigned to an ID corresponding to a sensor. The analysis software is in charge to assign correctly the hit to the sensors and then to group the pixel fired into clusters. As the sensors used during the test beam have a binary output, no information on the seed pixel is available. Thus, the hit position is obtained from a centre-of-gravity calculation.

Secondly, with the analysis software, one plane is considered as the origin of the telescope coordinate system and is used as a reference for the alignment. Usually, the first sensor hit by the beam is the main reference. The alignment means to correct the offset for the view angles and the hit position of the telescope planes and the DUT. These offsets are found thanks to scattering plots where the residuals are represented as a function of predicted hit position. An alignment is considered as a good one when the residuals are not correlated to the predicted hit position. If it is not centered around zero, an offset has to be applied in this direction, whereas a slope indicates that a tilt has to be applied. First off, the hit positions of the first plane are extrapolated to the next planes in order to perform the alignment. These tracks extrapolated are straight lines perpendicular to the hits position. Thus, the hit position of the last telescope plane is adjusted to match the hit position of the first plane. The alignment is an iterative procedure which consists to minimise the residual. It corresponds to the distance between the extrapolated track to the closest hit on the sensor. Afterward, the track candidates are built by matching a hit on the first plane to a hit on the last one. The second and third telescope planes are aligned with respect to the information provided by the extrapolated tracks. For example, figure 7.3a and 7.3b show the residual distributions of the second and third planes in the u and v direction with respect to the tracks built by the first and the last planes.

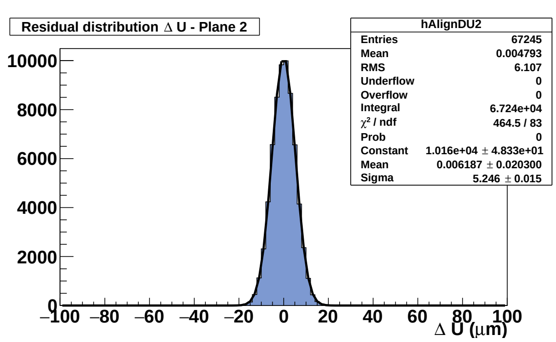

(a) Along u direction.

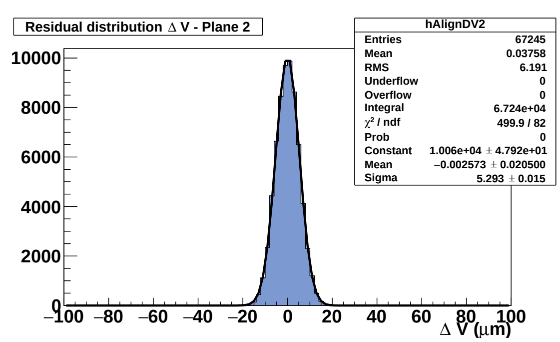

(b) Along v direction.

Figure 7.3 – Residual distributions in the u and v directions for the middle telescope planes.

As already explained, the alignment is an iterative procedure. At the beginning, a region of interest of 1000×1000 μm around the extrapolated is used to find a matching hit. Step by step, this region of interest is restricted to achieve a region of six times the pitch of the sensor.

After aligning the telescope, a candidate track is dismissed if it is made of less than four hits or if the χ^2 fit is greater than a fixed value determined by the user. Two assumptions are used during the alignment. The telescope planes are parallel each other. Thus the alignment consists of a translation along x and y and a rotation around the z-axis. As the test beam was performed without a magnetic field and pions of 120 GeV were used, the Coulomb multiple scattering is neglected. So, the tracks are perpendicular to the detectors and the alignment is not sensitive to the z position. A precision of the millimeter level for the position does not have a huge impact on the alignment.

Alignment of the DUT

When the telescope alignment is done, the reference tracks reconstructed by the reference planes are used to align the DUT. Its z position is fixed, nonetheless, two degrees of freedom are added to the three degrees defined above: the rotations along the x and y-axes. To assist the user in the alignment steps, several scatter plots are produced (see figure 7.4). For examples, figures 7.4a and 7.4b help to indicate a tilt in the z-direction, whereas figures 7.4c and 7.4d help to find shift and/or tilt in the respective u and v-directions. Figures 7.4e and 7.4f show the residuals distribution in both direction for one sensor of the DUT. The width of these distributions, called spatial residual σ_{res}, is approximately 4.1 m and is a combination of the telescope resolution σ_{tel}, the multiple scattering $\sigma_{\text{M.S.}}$ and the pointing resolution or spatial resolution of the sensor σ_{DUT}, as described in equation 7.1.

$$\sigma_{\text{res}}^2 = \sigma_{\text{tel}}^2 + \sigma_{\text{DUT}}^2 + \sigma_{\text{M.S.}}^2. \tag{7.1}$$

With 120 GeV pions, the effects of the Coulomb multiple scattering are neglected, thus the pointing resolution of the sensor is:

$$\sigma_{\text{DUT}} = \sqrt{\sigma_{\text{res}}^2 - \sigma_{\text{tel}}^2}. \tag{7.2}$$

For the configuration of the telescope used, the spatial resolution of the whole system measured is $\sigma_{\text{tel}} \simeq 1.8$ μm, thus the sensor studied here has a pointing resolution $\sigma_{\text{DUT}} \simeq 3.7$ μm for a threshold of 6 mV. This result is corroborating the pointing resolution of a single MIMOSA-26, as shown on figure 5.13 in chapter 5.

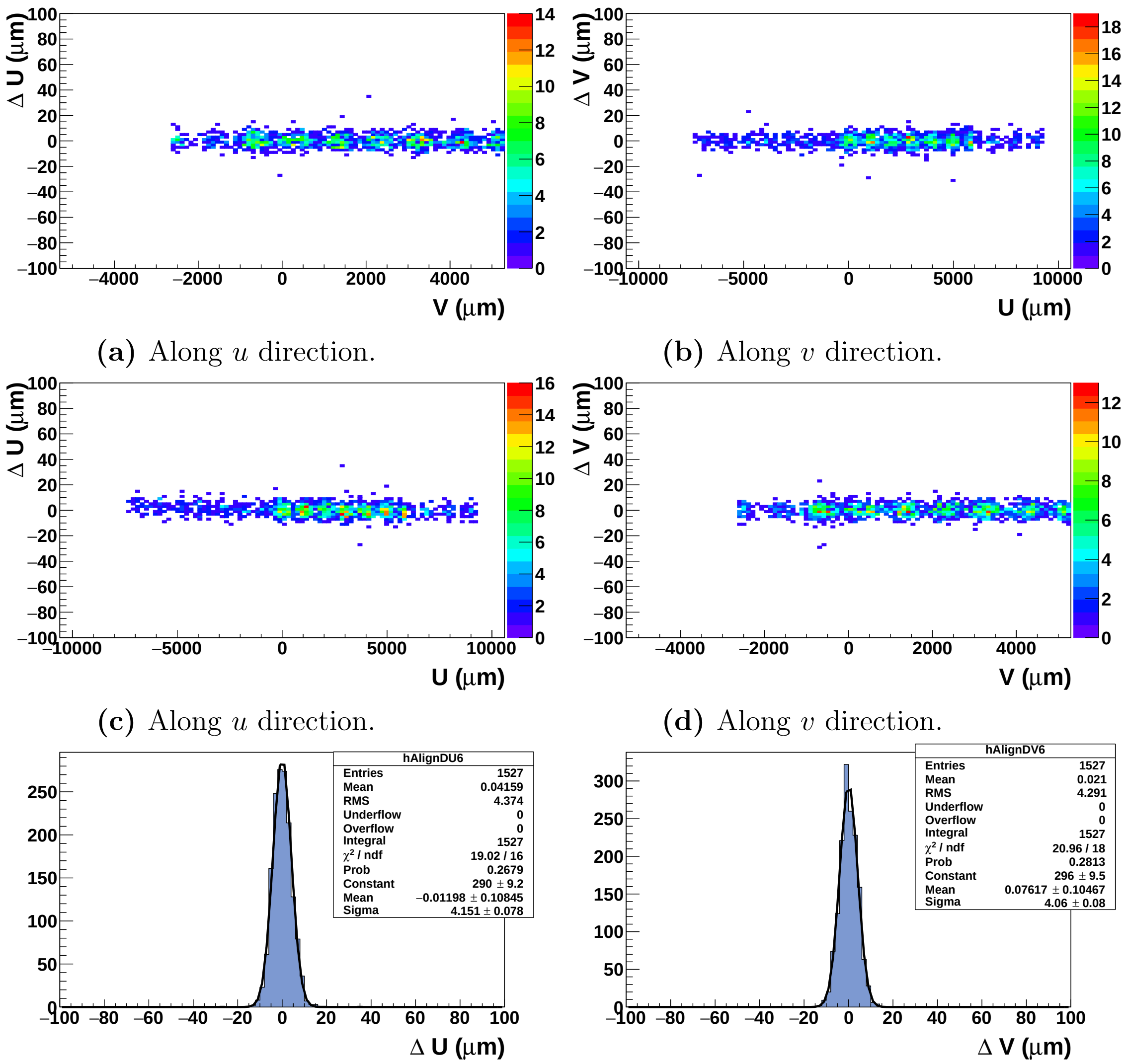

(a) Along u direction.

(b) Along v direction.

(c) Along u direction.

(d) Along v direction.

(e) Along u direction.

(f) Along v direction.

Figure 7.4 – Results of the DUT alignment: 7.4a is the residual ΔU as a function of the hit position on the v-direction, 7.4b is the residual ΔV as a function of the hit position on the u-direction, 7.4c is the residual ΔU as a function of the hit position on the same direction, 7.4d is the same plot for the other direction, 7.4e and 7.4f are the residuals distributions in the two directions.

7.2.2 Ladder tilted in one direction

The performances of the DUT are also studied for tilted tracks by rotating the ladder with respect to the beam axis along the v-direction. Three different angles were tested (28°, 36° and 60°), as well as different threshold cuts and air flow speed. The results presented below are for a run with a 36° tilt, a threshold sets to 5 mV and an air flow speed of 3 m.s^{-1}. The same alignment procedure as presented in the subsection above is used, nevertheless, the alignment of the plane along the u-direction is more complicated than the other direction. The scatter plot in the v-direction for the front plane which is shown on figure 7.5d represents a good alignment and the spatial residual (see figure 7.5f) is comparable to the one find for normal incidence tracks. But, the scatter plot $\Delta u = f(u_{\text{hit}})$ as presented on figure 7.5c shows a banana shape that can not be flatten with a traditional alignment procedure. Moreover, the spatial residual measured on figure 7.5e is larger (6.8 μm instead of ~ 4 μm in the v-direction) and the distribution has a large tail on the positive values. Concerning the back plane, the deformation is also visible on figure 7.6c but have a different form. The spatial residual measured for this plane is more than two times larger than the other side (14.1 μm) as it is depicted on figure 7.6e.

Origin of the deviations

The deviations observed are mainly caused by the characteristics of the ladder. Ultra-thin sensors with a thickness of approximately 50 μm are used. Naturally, without any mechanical structure, the sensors tend to be very flexible and not self-supporting. Nevertheless, the gluing procedure to the flex-cable and the SiC foam induces permanent deformations of the surface that can not be flattened. Also, the foam has an open-cell structure with small bumps and the glue spots might be more or less important on some positions. The Bristol group has performed a mechanical survey on a mechanical prototype, which has non-functioning MIMOSA-20 sensors. The chips were thinned and attached to the standard flex-circuits. The measurements done with an optical survey equipment have revealed a peak-to-peak flatness of the order of the 100 μm on both sides. Figure 7.7 shows the result of this survey. The overall shape is due to the intrinsic shape of the foam.

Another parameter has to be taken into account to explain the deviation observed. During the analysis, this non-flatness structure is not taken into account. The sensors are modelled as completely flat planes and the z-position is fixed. However, the sensor's position in three dimensions is actually different due to the deformations. When the particles are not striking

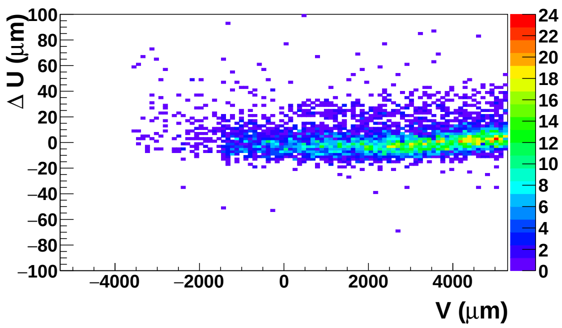

(a)

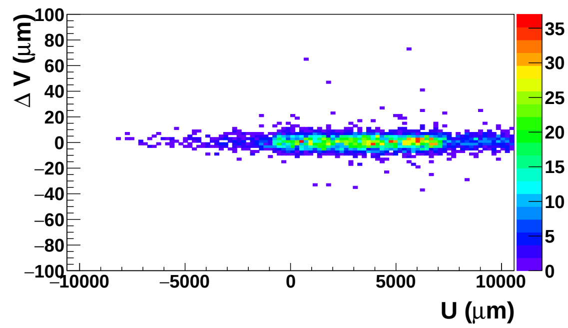

(b)

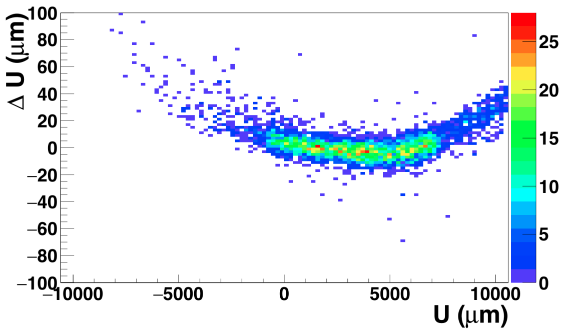

(c)

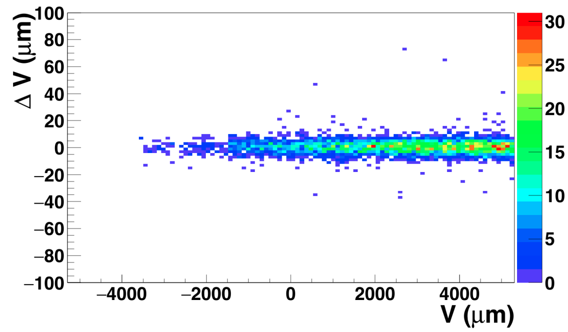

(d)

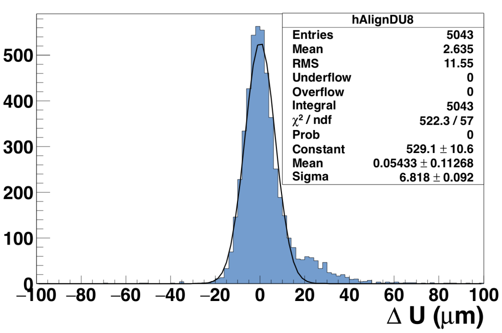

(e)

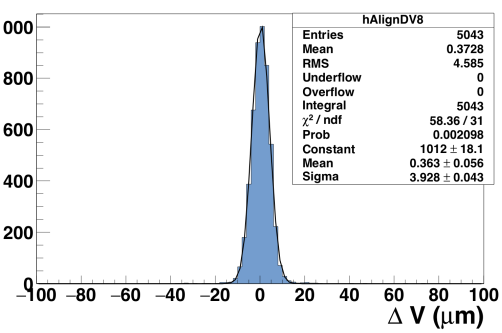

(f)

Figure 7.5 – Distribution of the residuals obtained for the front sensor with a tilt of 36°: 7.5a $\Delta u = f(v_{\text{hit}})$, 7.5b $\Delta v = f(u_{\text{hit}})$, 7.5c $\Delta u = f(u_{\text{hit}})$, 7.5d $\Delta v = f(v_{\text{hit}})$, 7.5e distribution of the residual Δu and 7.5f distribution of the residual Δv.

the sensor in normal incidence, the hit predicted with respect to the flat plane does not have the same position anymore. Thus, the residual between the position of the extrapolated track and the predicted hit is increasing.

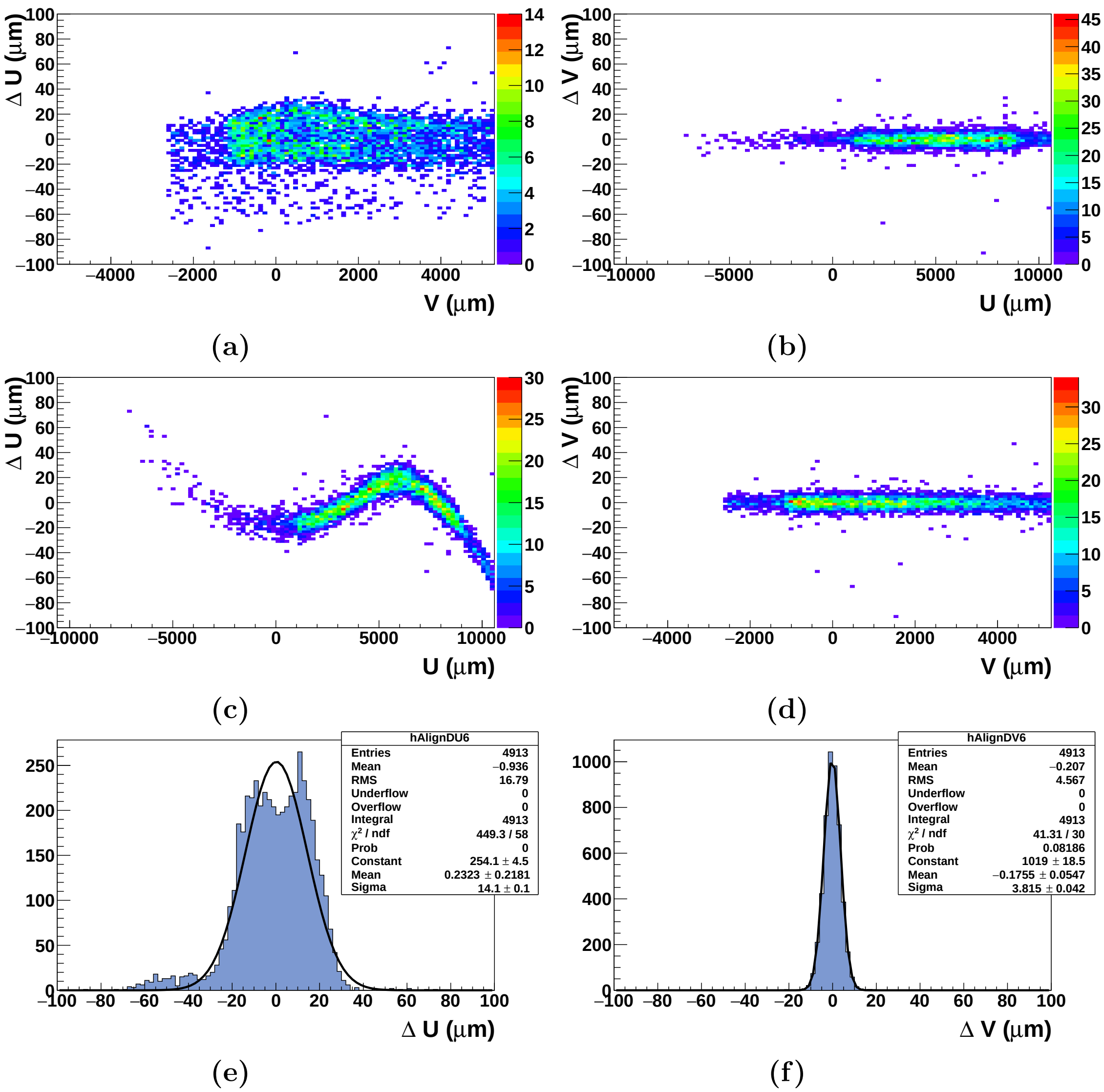

Figure 7.6 – Distribution of the residuals obtained for the back sensor with a tilt of 36°: 7.6a $\Delta u = f(v_{\text{hit}})$, 7.6b $\Delta v = f(u_{\text{hit}})$, 7.6c $\Delta u = f(u_{\text{hit}})$, 7.6d $\Delta v = f(v_{\text{hit}})$, 7.6e distribution of the residual Δu and 7.6f distribution of the residual Δv.

Figure 7.8 depicts the difference between the hit expected U_{h} on the flat plane and the extrapolation of the actual hit $U'_{\text{h extrapolated}}$. For a normal incidence, these two hits are at the same position, but larger is the angle,

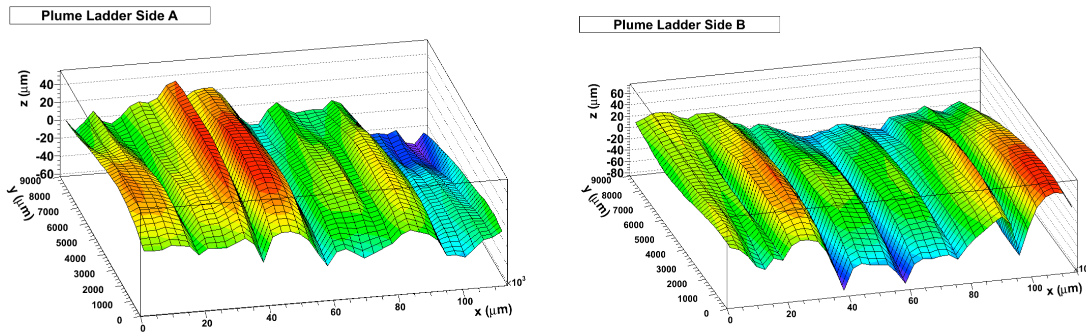

Figure 7.7 – Results of the mechanical survey of each side of the PLUME mechanical prototype.

larger is the difference between the expected hit and the extrapolated one. The deformation height δw can be expressed as a function of the angle θ and the residual δu of the track:

$$\delta w = \frac{\delta u}{\tan(\theta)}. \tag{7.3}$$

Thus, the visible deformation of the surface is sensitive to the angle of the incoming track. In the case presented above, the angle of the incoming track is only in one direction and so, the deformations are visible only in the u-direction and the other one is not affected, even if the deformations are in two dimensions.

Algorithm to estimate the deformations

The sensor deformations were already studied in Strasbourg by Robert Daniel Maria. The sensor was mapped for the alignment in order to remove the contribution of the deviation on the residual [65]. As this method is done manually and is time-consuming, an automatic method has to be implemented. A similar effect was observed in the CMS tracker during the alignment procedure with cosmic rays and a method was developed to compensate the deformations [1]. They have used modified two-dimensions Legendre polynomials to parametrise the sensors' deformations and therefore, they were able to minimise the effect of the deviations during the alignment procedure of the tracker. The method implemented in TAF was inspired by the work

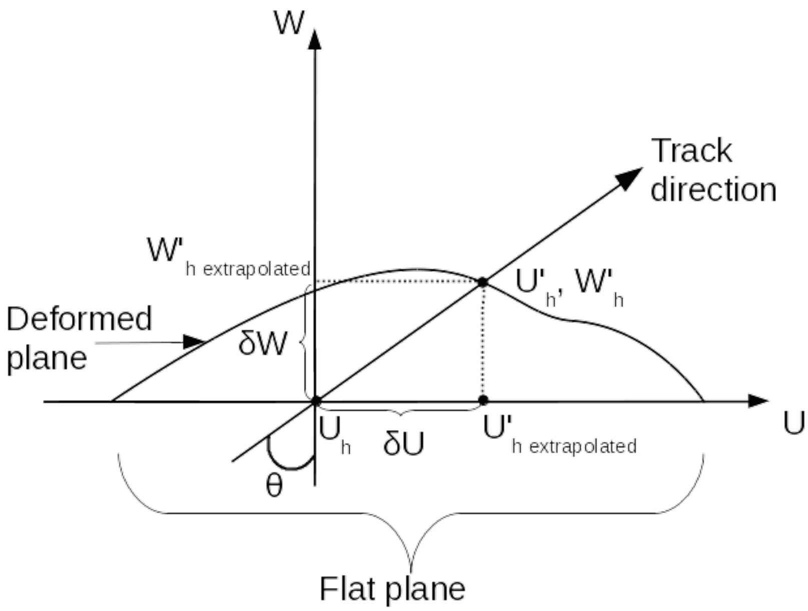

Figure 7.8 – Side view of the sensor's deformation.

which was done by the CMS collaboration. Nonetheless, contrary to the CMS tracker, the tilt was produced only in one direction. Hence, the two-dimensions Legendre polynomials can not be used to parametrise the sensor's deformations, but the problem is still the same. Tracks with a large angle of incidence are more sensitive to the exact position of the plane in three dimensions, so the coordinates of the hits have to be exactly known. The deviations observed on figure 7.5c provide an information on the behaviour of the deformation, that is extrapolated to the position of the plane on the w-direction. Thus, the hit position is calculated again with respect to the sensor's surface shape extrapolated. This shape is guessed from the track-hit residuals as a function of the hit position in the same direction. A Legendre function is used to fit the curve and the coefficient given by the fit steps are used to calculate the deformation of the plane. The equation 7.4 represents the extrapolated shape of the plane in the w-direction calculated with respect to the expected hit position u_r, which is normalised to the sensor width.

$$w\left(u_r\right) = \sum_{k=0}^{n} \omega_k P_k\left(u_r\right). \tag{7.4}$$

The ω_k are the coefficients that quantify the sensor curvature and $P_k(u_r)$

are the Legendre polynomials defined by the equation 7.5:

$$P_k\left(u_r\right) = \frac{1}{2^k!}\frac{d^k}{du_r^k}\left(\left(u_r^2-1\right)^k\right). \tag{7.5}$$

Then, the exact hit position is calculated by correcting the hit position extrapolated by $(-\omega(u_r).\tan\theta)$, according to the equation 7.3 and the residual Δu is determined by taking into account the tracks' angle during the analysis.

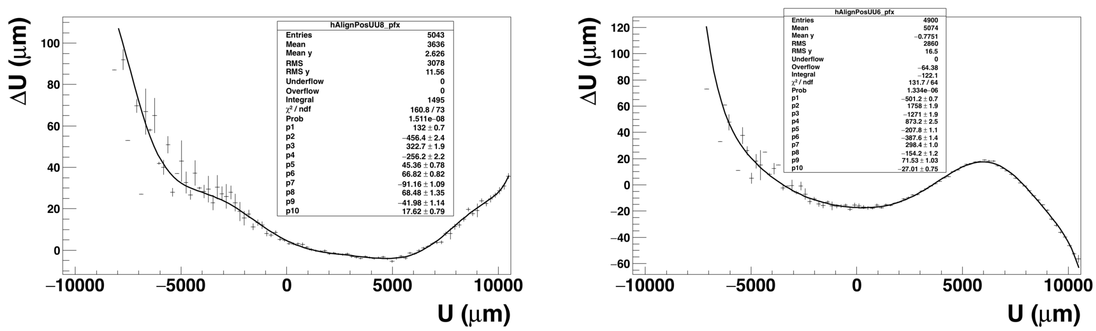

(a) (b)

Figure 7.9 – Profile of the scatter plot showing the track-hit residual in the u-direction as a function of the hit position on the plane for the same direction: 7.9a is the profile of the front plane and 7.9b is the profile of the back plane. Both profiles were fitted with a sum of Legendre polynomials up to the eleventh order.

Correction of the deformation

Contrary to the CMS case, the Legendre polynomials used here are calculated in one dimension as the tilt is only in one direction. The scatter plot displayed in section 7.2.2 was profiled and fitted with a Legendre function. The sum of Legendre polynomials up to different orders was tried to find the function fitting the best the profile. The coefficients obtained after fitting are used to parametrise the surface's shape and the position of the hit. Table 7.1 summarises the different χ^2/NDF obtained for the different orders, as well as the residual measured in the u-direction after correction.

A second-order Legendre function does not fit well the profile of $\Delta U = f(u_{\text{hit}})$ and does not provide a good improvement on the compensation of

	Front plane		Back plane	
Order	χ^2/NDF	σ_U^{front}	χ^2/NDF	σ_U^{back}
3	21683.9/84	6.51	35575.2/72	13.28
4	1449.91/83	6.18	25129.8/71	12.38
5	1449.79/82	6.00	1718.81/70	6.92
6	653.738/81	5.92	1480.55/69	6.82
7	304.206/80	5.92	634.696/68	6.41
8	288.376/79	5.94	269.296/67	6.23
9	225.376/78	5.90	250.565/66	6.24
10	225.353/77	5.91	152.236/65	6.16
11	158.053/76	5.91	131.727/64	6.18

Table 7.1 – Fit results of the scatter plot $\Delta U = f(U)$ for Legendre polynomials order and the residual obtained on each side of the PLUME ladder.

deformation. The best improvement was achieved on both sides from the 8^{th} order Legendre polynomials to higher values. Although the χ^2/NDF is better for higher order, the width of the residual distribution is of the same order ($\sigma_{\text{front}} \simeq 5.9$ μm and $\sigma_{\text{back}} \simeq 6.2$ μm). Figure 7.9a depicts the fit results for the front plane ans figure 7.9b is for the back plane. For both figures, the deviation is not well fitted for the negative values. The dispersion of the residuals is wider.

For example, using a 11^{th} order Legendre polynomials has improved the spatial residual for both planes. Instead of $\sigma_u \simeq 6.8$ μm for the front plane, the spatial residual is $\sigma_u \simeq 5.9$ μm, namely an improvement of 13.2 % of the measured spatial residual and achieving a pointing resolution of 5.6 μm for a tilt at 36°. Concerning the back plane, the spatial residual measured was 14.1 μm and after the correction it achieves 6.2 μm, namely an improvement of 56.0 % on the measured spatial residual. The point resolution of the plane is then 5.9 μm As it can be seen on figure 7.10c, the deviations are reduced. Nevertheless, the edges of the plot are less corrected. This is due to the fact that the length of the sensor used to parametrise the Legendre function is a bit different to the real size of the sensor due to the deformation. On the back plane, a bump is still visible in the middle of the scatter plot (see figure 7.11c). This may be due to a missing information on the deformation of the sensor in the other direction.

This method was applied for different angles and the results are summarised in table 7.2. The correction based on Legendre polynomials shows good results for the 28° angle with a pointing resolution of 4.6 μm. Although for larger angles the precision is not expecting to reach the normal value, the

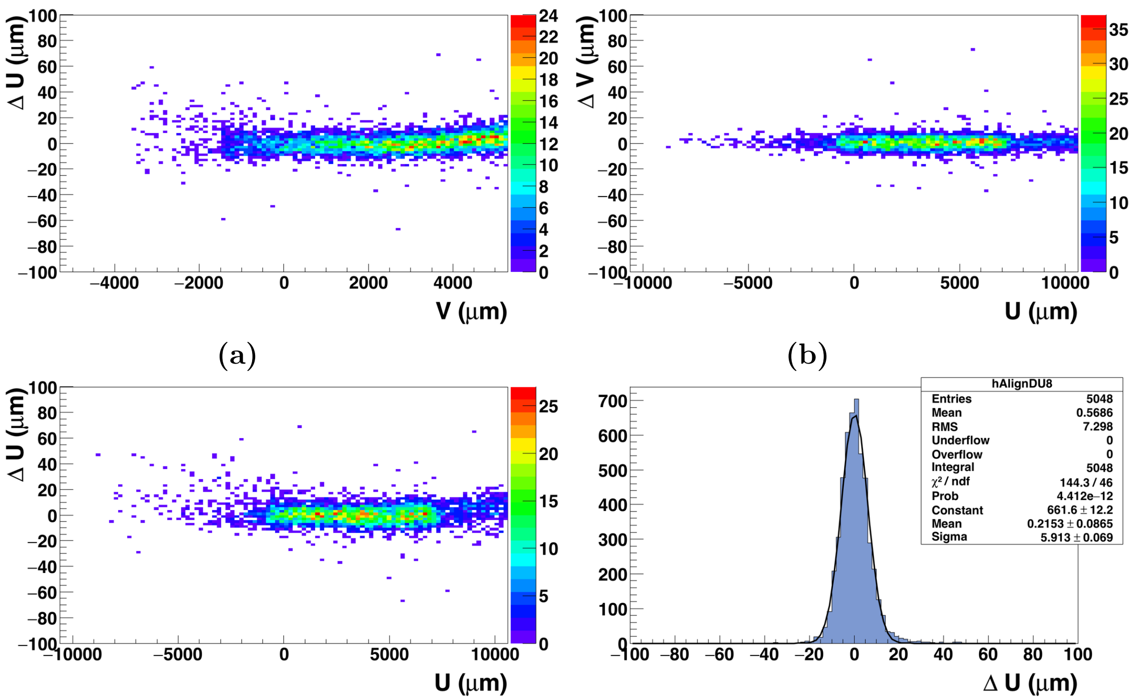

(a) (b) (c) (d)

Figure 7.10 – Results of the alignment after applying the Legendre polynomials correction and tacking into account the angle of the incoming particles for the front sensor: 7.10c $\Delta u = f(u_{\mathrm{hit}})$ and 7.10d distribution of the residuals.

results obtained are less positive. For the large angle (60°), the position of the DUT on the outside of the telescope arms does not provide a good telescope resolution ($\sigma_{\mathrm{tel}} = 18.8\ \mu$m). The pointing resolution achieved for the front and back planes are respectively 10.8 μm and 17.7 μm. The sensitivity of the reconstruction to large tracks angle, as well as a unadapted telescope configuration impact severely the spatial resolution of the sensors.

A hypothesis on the deformation of the origin might come from heating or the cooling system that induces vibration. Although few runs were performed with a different air flow speed, the impact of the cooling system and the heat was not planned for this test beam. Thus, the results are not relevant enough to conclude for any vibration or the heat that tends to deform more the surface.

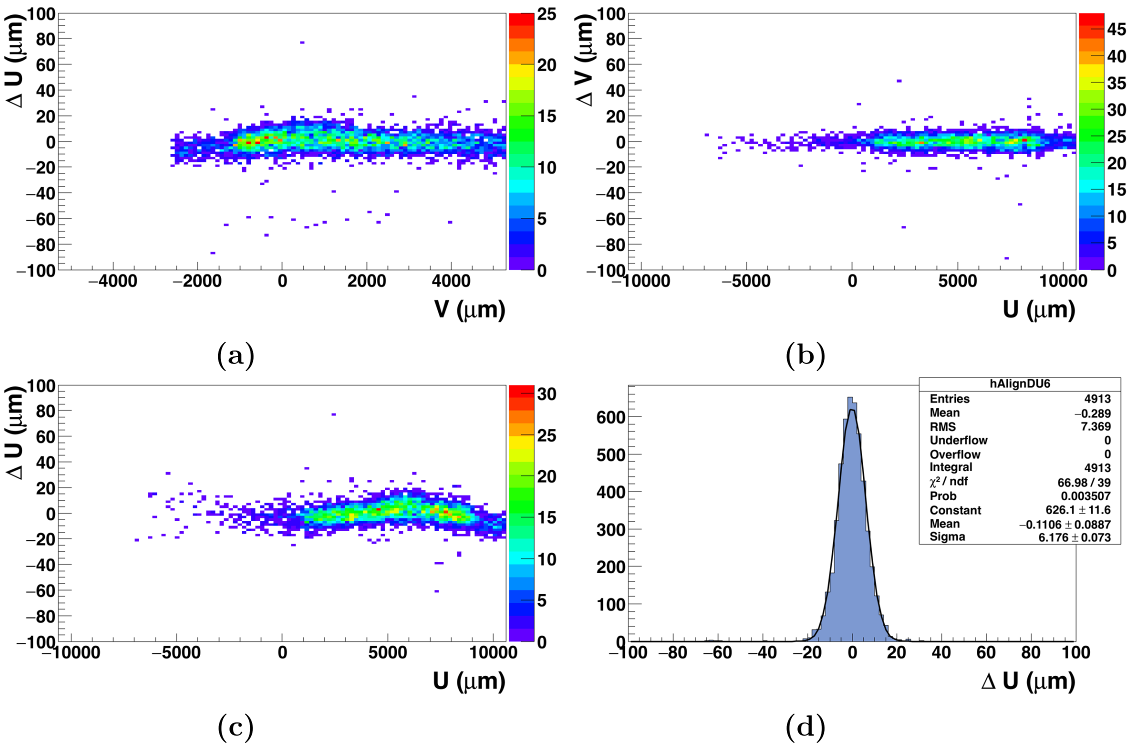

Figure 7.11 – Results of the alignment after applying the Legendre polynomials correction and tacking into account the angle of the incoming particles for the back sensor: 7.11c $\Delta u = f(u_{\text{hit}})$ and 7.11d distribution of the residuals.

Side	Tilted angle (°)	σ_U^{Def} (μm)	σ_U^{Cor} μm)	Improvement
Front	28	9.0 ± 0.1	4.9 ± 0.1	46.6 %
Back	28	5.7 ± 0.1	4.7 ± 0.1	17.5 %
Front	36	14.1 ± 0.1	6.1 ± 0.1	56.0 %
Back	36	6.8 ± 0.1	5.9 ± 0.1	13.2 %
Front	60	41.2 ± 0.15	25.8 ± 0.2	37.4 %
Back	60	23.3 ± 0.13	21.7 ± 0.1	6.8 %

Table 7.2 – Alignment results for different angles before and after using the correction based on Legendre polynomials.

7.3 Benefits of double-sided measurement

As two modules are sharing the same mechanical structure, the information provided by each side can be combined together. A mini-vector is created by connecting two hits on each side of the ladder for the same event. This combination gives access to a new information compared to a single sensor: the angular resolution.

7.3.1 Spatial resolution with mini-vectors

To study the benefits of the mini-vector, a virtual intermediate plane is defined at the center of the ladder. The two hits of each side of the DUT are connected to form a mini-vector and the intersection of this vector to the intermediate plane is determined. The intersection of the extrapolated track to the intermediate plane is also performed and the distance between the position of the track and the position of the mini is then measured.

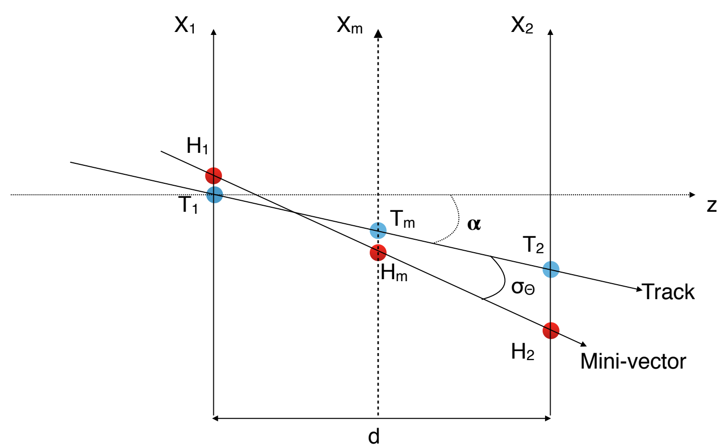

Figure 7.12 – Principle of the mini-vector. The two hits (in red) on the planes x_1 and x_2 are connected and the intersection on virtual intermediate plane x_m is then determined. The blue points represents the track extrapolated through the DUT.

A theoretical estimation of the spatial resolution for the mini-vector can be done thanks to the formula above:

$$\sigma_\mathrm{m}^2 = \frac{\sigma_\mathrm{front}^2 + \sigma_\mathrm{back}^2}{(d_\mathrm{front} - d_\mathrm{back})^2} \cdot d_\mathrm{m}^2 + \sigma_\mathrm{tel}^2. \tag{7.6}$$

Where σ_{m} is the resolution on the intermediate plane, σ_{front} and σ_{back} are the resolution of the two sides of the DUT, σ_{tel} the resolution of the telescope and $(d_{\mathrm{front}} - d_{\mathrm{back}})$ the distance between the front and back planes and d^2_{m} the position of the intermediate plane. For the plume ladder, the SiC as a thickness of 2 mm and the intermediate plane is located in the middle, the equation 7.6 can be rewritten:

$$\sigma^2_{\mathrm{m}} = \frac{\sigma^2_{\mathrm{front}} + \sigma^2_{\mathrm{back}}}{4} + \sigma^2_{\mathrm{tel}}. \tag{7.7}$$

Thus, if the resolution on both side of the telescope are similar with $\sigma_{\mathrm{front}} = \sigma_{\mathrm{back}} = \sigma$, the resolution of the mini-vector σ_{res} is then:

$$\sigma_{\mathrm{res}} = \frac{\sigma}{\sqrt{2}}. \tag{7.8}$$

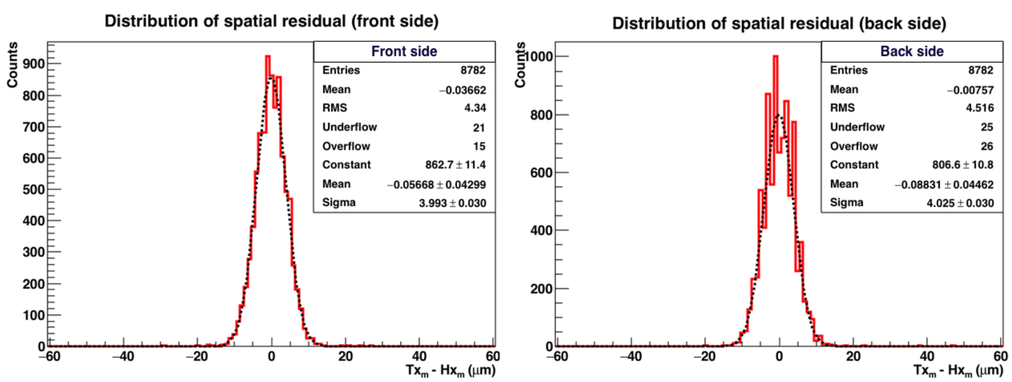

Figure 7.13 – Residual distribution for both side of the ladder in the u-direction

For a run in normal incidence, the spatial resolution measured on each side is $\sigma_{\mathrm{front}} \simeq \sigma_{\mathrm{back}} \simeq 4$ μm, according to figure 7.13. The resolution of the mini-vector should be then $\sigma_{\mathrm{res}} \simeq 2.8$ μm. The measurement of the residual for the mini-vector displayed on figure 7.14 gives a residual of 3.2 μm. Taking into account the resolution of the telescope, the spatial resolution achieved by the mini-vector is $\sigma_{\mathrm{res}} \simeq 2.9$ μm.

7.3.2 Angular resolution

The mini-vectors give an access to new information not provided by a single sensor, the angular resolution. The direction of the track can be compared

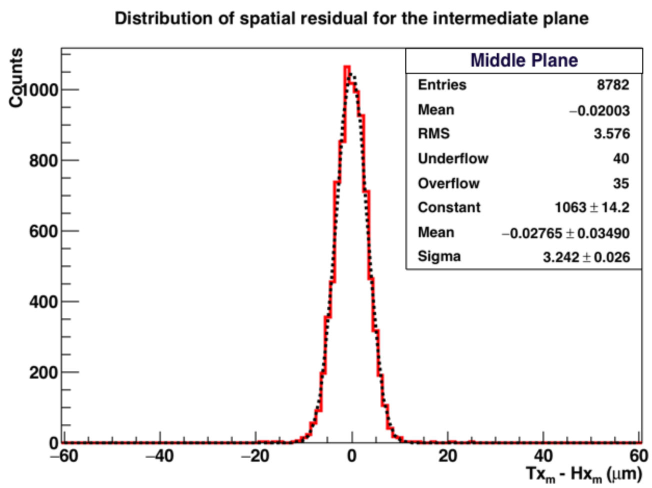

Figure 7.14 – Residual distribution of the mini-vector measured on the intermediate plane.

to the direction of the mini-vector. The estimation of the angular resolution is given by:

$$\sigma_\theta = \frac{\sqrt{\sigma_{\text{front}}^2 + \sigma_{\text{back}}^2}}{d}. \tag{7.9}$$

With σ_{front} and σ_{back} the spatial resolution on each side of the DUT in microns and d the distance between the two sides in microns. The spatial resolution here is $\sigma \simeq 3.6$ μm and the distance between the two planes 2000 μm. The angular resolution estimated is then $\sigma_\theta = 0.146^\circ$.

Figure 7.15 depicts the distribution of the angle between the tracks direction and the mini-vectors direction. As it can be seen, several peaks are present and the distribution can't be extrapolated by a Gaussian fit. The sensors have a binary output and the hit position is determined by the centre-of-gravity of the clusters. If the cluster is only one pixel, the centre-of-gravity will be in the middle of the pixel, but if the clusters contain more pixels, this centre-of-gravity will be displaced. Moreover, they are some deviations in the distance between the hit projected to one side to the real hit position on this side. Figure 7.16 represents the minimum distance between one cluster on one side to the cluster on the other side.

Hence, for one pixel clusters, the displacement between the two pixels is the pitch $p = 18.4$ μm and the angle between the two minimal hit position

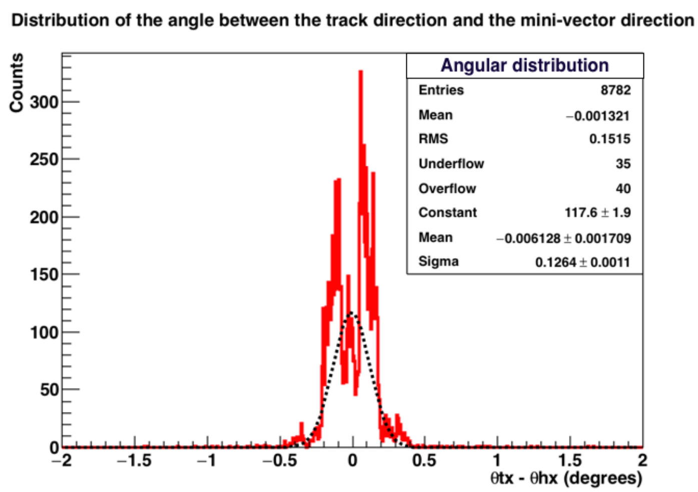

Figure 7.15 – Distribution of the angle between the tracks direction and the mini-vectors direction.

is then $\theta \sim 0.52^\circ$. A selection of the events where only clusters of 1 pixel are considered is shown on figure 7.17a. The two peaks have a spacing close to 0.5°. For clusters of 1×2 or 2×2 pixels, the distance between the two hit positions reconstructed via centre-of-gravity is half the pitch. Hence, the peaks are two times closer with a spacing of nearly 0.25°, as seen on figures 7.17b and 7.17c. Nevertheless, for larger cluster sizes the angular distribution has only one peak around 0°.

7.4 Conclusions

Along this chapter, the test beam campaign done in November 2011 at CERN was discussed. The results were focused on the alignment procedure, as well as the performances of the ladder in normal and tilted positions. The runs in tilted position were challenging to align due to some deviations between the track-hit residual and the actual hit position on the plane. This has the effect of increasing the spatial residual measured. A higher pointing resolution is expected for bending tracks but in a smaller proportion. An algorithm using Legendre polynomials to describe the sensor's shape was discussed. The results obtained for small angles are close to the value expected for a single MIMOSA-26 sensor in normal incidence. Nevertheless, the pointing resolution depends strongly on the incidence angle. For 36° and higher, the correction is less efficient to achieve the normal performances. It might also

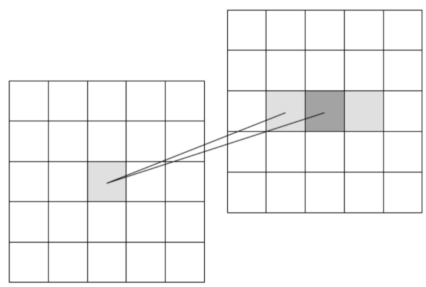

(a) One pixel per cluster.

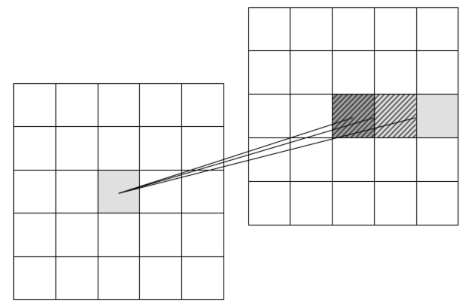

(b) 1×2 pixels per cluster.

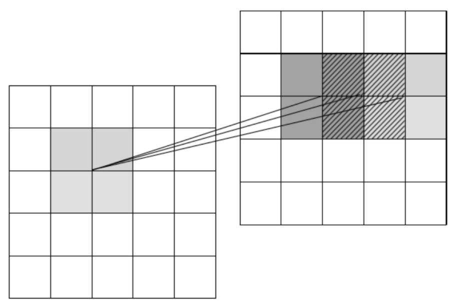

(c) 2×2 pixels per cluster.

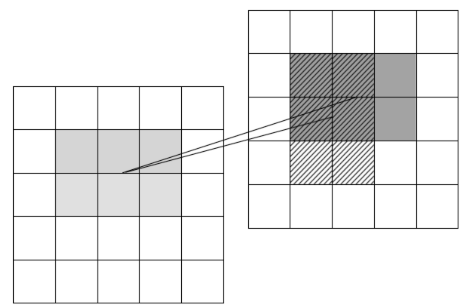

(d) 3×3 pixels per cluster.

Figure 7.16 – Minimum distance between the cluster projected on one side to the position of the cluster of this side.

be possible that the heating is increasing the deformation and that the cooling system could induce some vibrations which induce some deformation too. Nevertheless, the results obtained here for different air flow speed can not lead to a conclusion on a possible impact of the cooling system.

The second part of this chapter was talking about the benefits of double-sided measurements. For normal incidence, the pointing resolution of the mini-vector, which is the combination of the pointing resolution on each side, is better than the spatial resolution of a single sensor. Moreover, the mini-vectors give access to another information: the angular resolution. Due to the binary output and the centre-of-gravity hit position reconstruction, multiple peaks are visible and a simple Gaussian fit can not be used. The same work has to be done with ladder titled with respect to the beam to study the impact of the deformation on the mini-vectors.

The first results obtained are encouraging the mechanical structure. Nevertheless, the material budget of the ladder is estimated theoretically. The next chapter will introduce a test beam performed at DESY in 2016 and

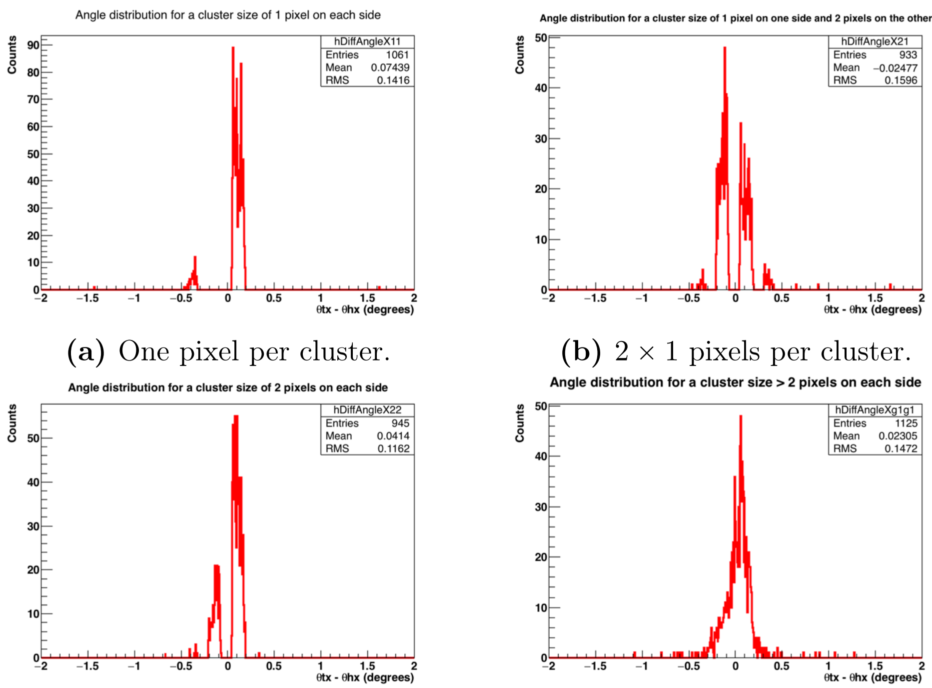

(a) One pixel per cluster.

(b) 2×1 pixels per cluster.

(c) 2×2 pixels per cluster.

(d) Clusters bigger than 2×2 pixels.

Figure 7.17 – Minimum distance between the cluster projected on one side to the position of the cluster of this side.

will specifically talk about the measurement of the radiation length for a PLUME-V1 prototype.

Chapter 8

Determination of the material budget

The discovery of new physics and the characterisation of the already known particles are possible only with performant detectors. As it was presented in chapter 5, the fabrication of a vertex detector is mostly constrained by two parameters: the pointing resolution and the material budget. The first fully functional prototype of PLUME was tested in November 2011 at CERN with 120 GeV pions. The results have shown that the pointing resolution of the ladder corresponds to the expected value for the ILD. Moreover, the use of a double-sided structure improves this pointing resolution. Nevertheless, the material budget (X_0) of PLUME has not been studied yet and only estimated by calculation. SPS beam is involving particles with too high momentum, so they suffer less from the effect of the multiple scattering. Therefore, a test beam campaign of the PLUME-V1 prototype was done in April 2016 at DESY test beam 21 with positrons up to 5 GeV. Firstly, the presentation of the test beam is discussed. Secondly, the motivation, the test beam facility, as well as the tools used for the analysis are presented. Finally, the last section is dedicated to the data analysis leading to the radiation length measurement.

Contents

8.1 Preparation of the test beam

In April 2016, a test beam campaign with electrons up to 5 GeV was performed at the DESY-II test beam facility [24]. The preparation of a test beam campaign is a long, intense and stressing period. The different aspects of the test beam have to be carefully thought to minimise the problems and the time spent for debugging during the test period. This consists in scheduling precisely the different measurements that have to be performed during the restricted time, as well as the set-up to use, the integration of the DUT and the acquisition system to use.

8.1.1 Measurements and telescope configuration

Although the first prototype was validated with 120 GeV pions in November 2011 at CERN, two aspects were not yet studied. The first one is the ability of the detector to detect and track low momentum particles such as electrons. The spatial resolution, the detection efficiency and the benefits of mini-vectors with the DESY test beam have to be measured and compared to the values obtained at CERN. Runs with different tilts (from 0° to 60° with a step of 10°) and different air flow speeds for the cooling system (3 and 6 $\mathrm{m.s^{-1}}$) are performed to study again the mechanical deformations of the ladder. The second aspect not yet studied is the measurement of the equivalent radiation length of PLUME. For the first time, the collaboration wants to confirm the theoretical estimations, which give a weighted material budget $X_0|_{\mathrm{weighted}} \simeq 0.65$ % for the version tested. Although many runs were acquired to perform the different measurements, the test beam was scheduled at the end of my Ph. D. Therefore, I am not able to perform a complete analysis of the first prototype for low momentum electrons. Section 8.3 presents the study I have performed on the radiation length measurement.

Before going to the test beam and acquiring data, the geometry of the telescope has to be determined to optimise the tracking. This depends on the spacing between the different planes and the position of the DUT respectively to the telescope. The best track extrpolated on the DUT position is achieved by placing the inner planes of the telescope as close as possible to the DUT and the outer planes as far as possible from the DUT. Because of the deformation study, which needs to rotate the ladder (see chapter 7), the inner planes can not be pressed to the DUT without modifying the geometry at each steps. Hence, to keep a consistent alignment and to reduce the time spending on the off-line alignment, it was decided to fix the inner planes as close as possible to be able to rotate the ladder without modifying the geometry. Moreover the ladder is not centered in its box, so to keep an equal distance between the two sides of the ladder and the two inner planes, the minimal distance between the telescope planes are calculated by taking into account an offset. It has to be noted also, that for the radiation length measurement, the geometry is different. The upstream planes are stacked together and really close to the DUT, whereas the downstream planes are distant from each other.

For the first time, the collaboration has decided to use the EUDET telescope and EUDAQ [28] for the acquisition, instead of the Strasbourg telescope and the IPHC acquisition. Several configuration are available for the set-up used. The first ones consist to use the six planes of the EUDET telescope [44] and to have two separate acquisitions, one for PLUME and the second one dedicated for the telescope. Then, the data have to be merged together. As the EUDET telescope is equipped with the same sensors as PLUME, the acquisition can be simplified by having only four telescope planes and connecting directly two sensors of the DUT. A simulation toolkit developed by Simon Spannagel [68] and based on General Broken Lines (GBL) [47] is used to compare the pointing resolution at the DUT position for different telescope geometries. Here, the six and four telescope planes set-ups are compared for different energies and spacing between the sensors. This simulation takes into account the material budget of the telescope, the DUT and the multiple scattering of electrons in the air[1]. One telescope plane has a material budget of ~ 0.053 % of X_0, whereas PLUME is ~ 0.65 % plus two kapton foils used to insulate the ladder from the light (~ 0.071 % X_0). For both configurations, the telescope is divided into two arms, two or three planes on each side of the DUT. The maximal distance between each reference plane of one frame is $d_{max} = 150$ mm for the six sensors configuration, whereas for the second one it is $d_{max} = 300$ mm.

[1]The simulation is not based on a proper Monte-Carlo tool, but calculates the multiple scattering with an approximation of a Gaussian process

Energy (GeV)	σ_{res} (μm)	
	4 planes	6 planes
2	4.9	4.8
3	3.8	3.8
4	3.4	3.4
5	3.1	3.2
6	3.0	3.0

Table 8.1 – Estimation of the resolution on the track extrapolation σ_{res} at the DUT position for a telescope with four planes and six planes. Practical issues, such as the alignment, will limit the precision on the track extrapolation to 100 nm.

Table 8.1 summarises the resolution on the track extrapolation at the DUT position for different energies and the use of four or six telescope planes does not have an impact on the telescope pointing resolution. Figure 8.1 displays the pointing resolution as a function of the different spacing between two telescope planes of the same frame, for an energy sets to 4.7 GeV.

As the number of telescope planes does not impact the pointing resolution, it has been decided to use only four telescope planes and two PLUME sensors (one on each side) to simplify the acquisition system. However, the synchronisation and the stability of the acquisition have to be tested before the test beam campaign.

8.1.2 Acquisition system and experimental set-up

EUDAQ

EUDAQ is a modular cross-platform data taking framework developed for the EUDET-type beam telescopes [44]. It is designed to be flexible and to have an easy integration of other devices. The software is based on *producers*, that are linked between the different subdetector systems, such as the beam telescope, the DUT user's DAQ and the Trigger Logic Unit (TLU) [20]. The events of each subdetector are then correlated to form one single global event for data belonging to one trigger. This step is done by the *Data Collector*. The robustness of the acquisition set-up planed is tested by performing multiple runs for multiple configuration in the laboratory. The data are acquired with only the PLUME to ensure that EUDAQ can cope it, and then single MIMOSA-26 sensors are added and runs of several hours are performed to look for a loss of synchronisation.

Experimental set-up

Finally, the integration of PLUME for the different measurements to perform is investigated. For the deformation studies, the DUT is mounted on a rotation stage. With respect to the local coordinate system (or sensor coordinate system), the rotation is along the u-direction. The first option considered to perform the rotation is to orient the ladder in the same direction as the telescope's sensors. Hence, the ladder is in the horizontal position and the rotation needs a complicated frame to ensure the stability of the system. The weight of the box and ladder is applied only on the rotation stage. Due to the complexity and the time needed to build this frame, a second option has been considered. The ladder is placed vertically on a rotation stage. There is a 90° rotation between the telescope sensors and the PLUME ones. The frame consists of an insulated aluminum plate on which the DUT sits. To avoid damaging the DUT during the test beam, the flex-cable is maintained on the frame by two clamps. In this way, less constraint are applied on the

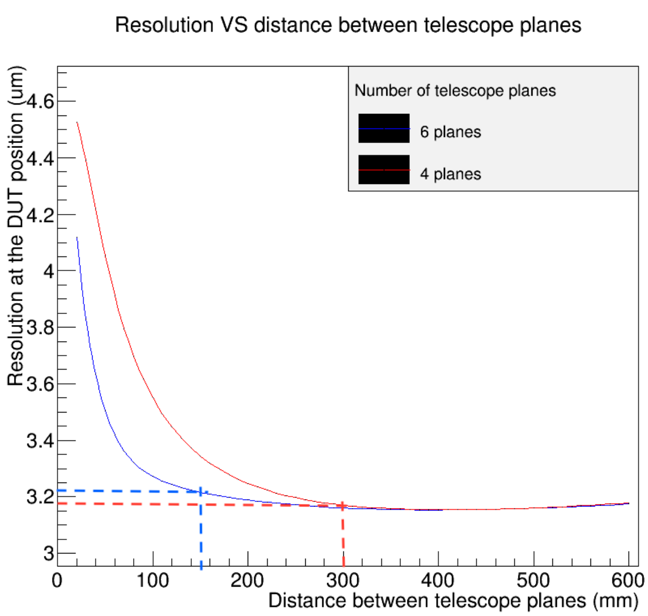

Figure 8.1 – Estimation of the track extrapolation resolution at the DUT position as a function of the distance between two telescope planes of the same arm for an energy of 4.7 GeV. The blue lines is the results for six planes, whereas the red line is for four planes. The dashed lines are the maximal distance between two planes due to the rail limitation of the telescope frame.

connectors. A plate with screws hold the ladder strongly to the frame. The frame is then mounted onto a rotation stage, which is mounted on a translation stage. Figure 8.2 shows a schematic model of the frame designed and built at DESY.

To control the heating of the ladder during the test beam, a cooling system consisting of a simple fan is used. On one endcap, a pipe is fixed and connected to the fan. Some studies in Strasbourg were done to determine the air flow speed as a function of the voltage applied. Hence, an air flow speed of 3 m.s^{-1} is achieved with 5 V and an air flow speed of 6 m.s^{-1} for 10 V. This values result in an operating temperature of all sensors between approximately 40°C and 52°C.

During the test beam campaign, the *clock* and *marker* are read from one sensor of PLUME. The *clock* is extended with a 80 cm long cable to ensure that one frame starts on the rising edge. The second input of the acquisition is a PLUME sensor (opposite side of the first sensor), followed by the four telescope planes. Moreover, Photomultiplier Tube (PMT)s are placed in coincidence on each side of the telescope. They are used to trigger the acquisition only when the beam passes through the entire set-up. Hence,

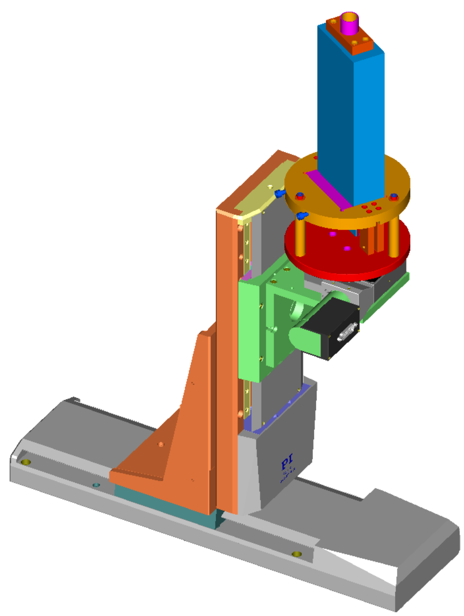

Figure 8.2 – TCAD model of the mechanical structure designed for the test beam in April. The ladder is hold on a circular frame fixed to a PI rotation stage, mounted onto a XY-table.

the fake events are reduced and the data stream is smaller. Figure 8.3 shows a schematic of the acquisition and set-up used during the test beam, while figure 8.4 is a picture of the system taken during the test beam.

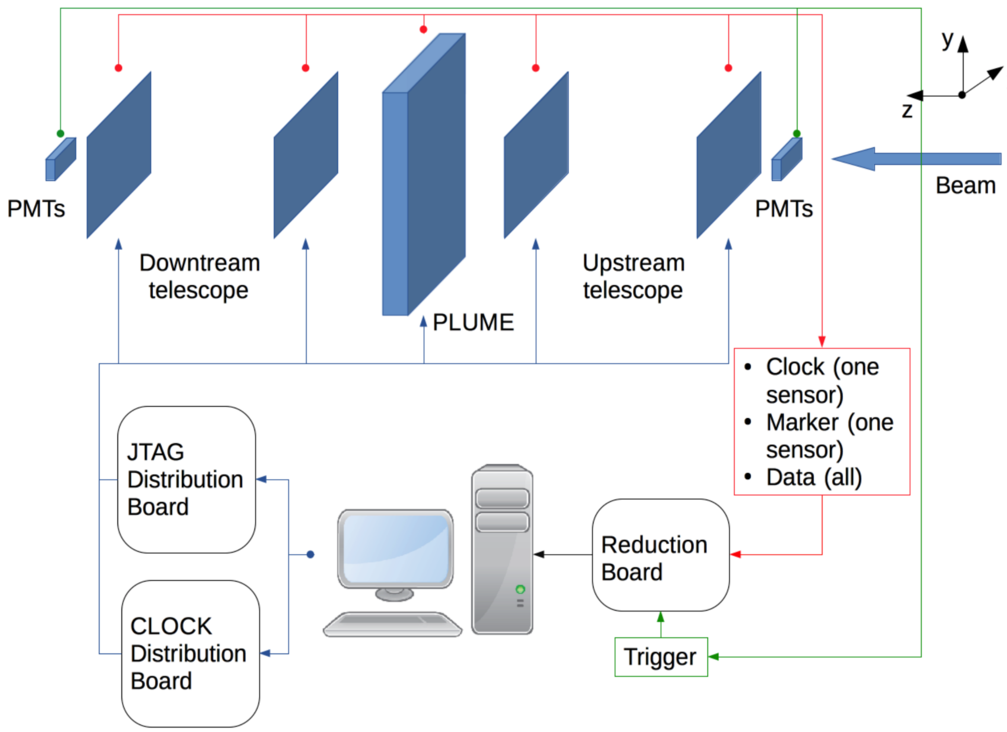

Figure 8.3 – Schematic of the test beam set-up. The PMTs are used for triggering. The clock and marker are read from only one sensor, here it comes from one PLUME sensor.

8.1.3 Issues during the test beam

The preparation of the test beam, as well as the data taking were a long and stressful period. Although everything were prepared as mush as possible to avoid any problem during the test beam, a broken component on the power distribution board has disturbed the data taking for two days. One PLUME module was not recording data anymore but was still sending *header* and *trailer*. Fortunately, after replacing the broken component, the ladder was working normally, but a shift on the thresholds has appeared. By characterising again the ladder, it has been possible to determine which thresholds

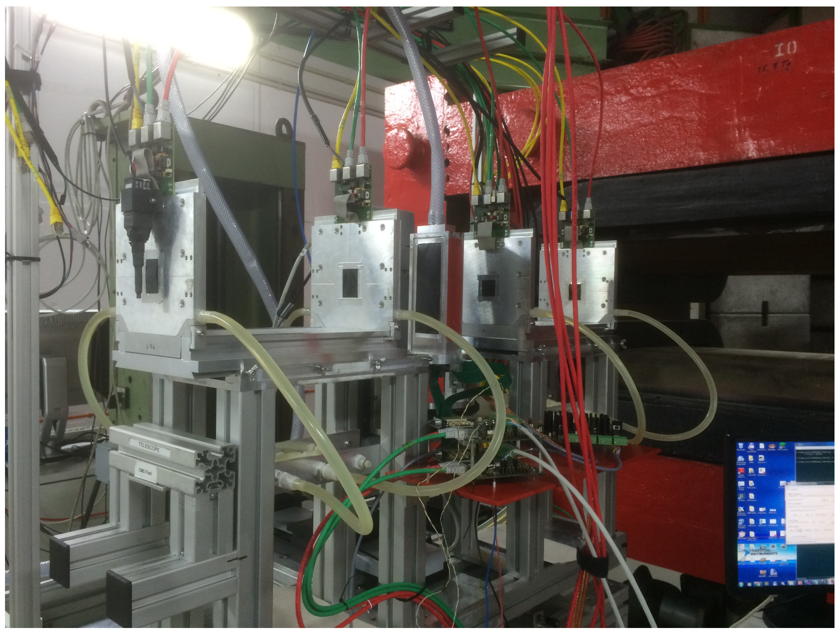

Figure 8.4 – Picture taken during the test beam. The beam is going out of the magnet (large red frame) before reaching the four detection planes (aluminum square frames), the DUT (elongated box) and the PMTs (one is visible at the left-end of the picture). The set-up is mounted on a floating frame insuring the electrical grounding.

were really applied. Nevertheless, it is likely that some data could have been corrupted and this is under investigation.

8.2 Measuring the radiation length

8.2.1 Introduction

When charged particles are traveling through matter, they lose energy via inelastic collisions with atomic electrons and this leads to the ionisation or excitation of the matter. Furthermore, along their path, they are deflected by many small angles from their initial trajectory due to Coulomb scattering from nuclei. This stochastic effect, called multiple Coulomb scattering, leaves on the average the particle undisturbed through its path. For small angles of deviation, the multiple scattering is following a Gaussian behavior, whereas for larger angles, it behaves like the Rutherford scattering. The Highland formula, which is an empirical formula, describes the distribution of the multiple scattering, or the "kink angle" θ_0 as a function of the momentum p of the incoming charge particles, its velocity βc, its charge number z and its true path length in radiation length unit $\frac{x}{X_0}$:

$$\theta_0 = \frac{13.6 \text{ MeV}}{\beta c p} \cdot z \cdot \sqrt{\frac{x}{X_0}} \left(1 + 0.038 \cdot \ln \left(\frac{x}{X_0} \right) \right). \tag{8.1}$$

For the electrons, a modified version of the equation 8.1 describes its scattering better than the Highland formula does [34].

$$\theta_0 = \frac{13.6 \text{ MeV}}{p} \left(\frac{x}{X_0} \right)^{0.555}, \text{ with } \beta c = 1. \tag{8.2}$$

The spread angle θ_0 depends on the momentum of the incoming particle, as well as the relative radiation length $\frac{x}{X_0}$. Thus, for a given relative radiation length, the kink angle is becoming smaller for higher momentum.

It is possible to determine the radiation length X_0 of a material knowing the energy of the particle, its thickness x and by measuring the kink angle θ_0.

8.2.2 Motivation

The design of a detector is driven by its intrinsic characteristics, such as the pointing resolution or the integration time, but also by some requirements on the material budget. For example, the ILC sets new goals for the design of the vertex detector, but also for other parts of the detector, as mentioned in chapters 3 and 5. For such detector, the tracking system should detect precisely the particles path and minimise their energy degradation, while the calorimeters have to measure accurately the energy deposited by the particles. During the physics analysis, the reconstruction of the events depends strongly on the knowledge of the energy loss by the particles inside the different components of the detector before they reach the calorimeters. To improve the results, a correction on the energy has to be applied. Thus, the study of the radiation length X_0 in g.cm^2, which is the amount of matter traversed by the electron is an important part of the detector development. For electrons and positrons, the radiation length corresponds to the mean distance over which these particles loss $1/e$ of their energy by bremsstrahlung.

As detector are made of different layers, the radiation length for composite materials is given as:

$$\frac{1}{X_0} = \sum_j \frac{\omega_j}{X_j}, \tag{8.3}$$

where ω_j and X_j are respectively the fraction by weight and radiation length for the j^{th} element.

8.2.3 The DESY II test beam facility

The DESY test beam facility [24] is composed of three areas. The electron beam is produced in the LINAC-II and accelerated up to 450 MeV before to be injected in the DESY-II synchrotron ring. The DESY-II is used as a storage ring for the PETRA-III accelerator. The beam is accelerated and stored until enough particles are available to be sent into PETRA, where they are used for photon science experiments.

To generate the beam delivered in the Hall 26, a graphite fiber target is placed inside the beam pipe. While the electrons are hitting the target, they lose energy and emit bremsstrahlung photons. The photons travel through the air and hit another target, on which the photons are converted to pairs of electrons and positrons. Different targets with different thicknesses are available and this will impact the particles rate. One is made of copper,

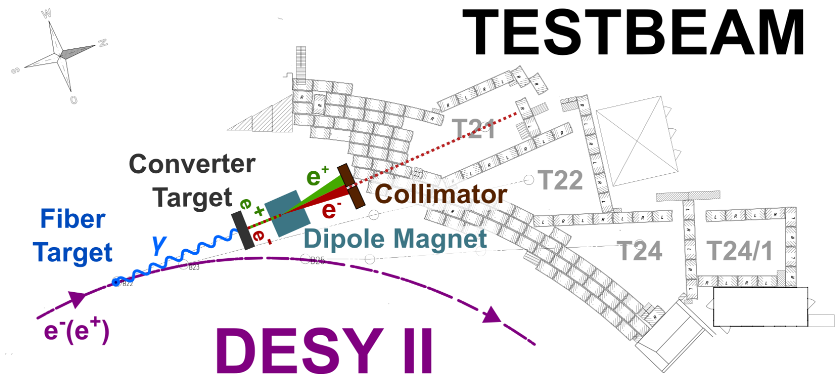

Figure 8.5 – Schematic layout of the DESY-II test beam facility [24].

whereas the other one is made of aluminum [56]. Then, a dipole magnet bends the particles and spread them according to their energy. Afterward, a tungsten collimator cuts away the unwanted particles, those having a too high or too low momentum, before the test beam area. A second collimator is located inside the test beam area and it determines the size of the beam spot. Figure 8.5 summarises the different steps to generate a beam of electrons or positrons in test beam 21, while the energies and the rates available are displayed in figure 8.6. The energy resolution achieved at DESY test beam reaches 5 %.

8.3 Analysis

8.3.1 Software analysis chain

The analysis of the test beam data is performed with EUTelescope [29][44]. It is based on the MARLIN framework, which is a part of the ILCSOFT (see 4.3.1 for more details about the ILCSOFT package). The software is used to convert the data into the LCIO format and to perform clustering search, alignment and final analysis. Each step of the analysis is driven by a dedicated processor and is described in figure 8.7.

A first processor is used to convert the raw data files acquired during the test beam into the LCIO format. The new file created contains the pixel number which fired in a given event, along with the sensor number. During the conversion, a hot pixel search is done to remove the noisy pixels from the list of hits. A pixel is considered noisy if its firing frequency is above a threshold value determined by the user (typically the cut value is between

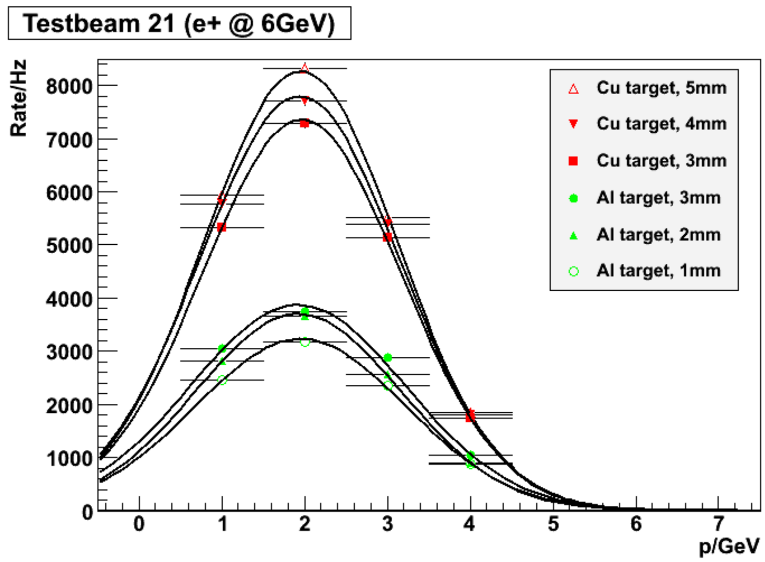

Figure 8.6 – Rate for different momentum and with different converter targets [24].

0.001 and 0.003 %). The noisy pixels correspond to defective raw or column or single pixels always sending information (see section 6.3). Then, a cluster algorithm forms clusters from adjacent fired pixels in a row and/or column. Afterward, the hit candidates are defined with a centre-of-gravity method and the position of the hit is determined in the telescope frame and in the sensor frame using the alignment constant.

Although the alignment procedure looks like the one presented in chapter 7, the procedure used with EUTelescope is slightly different. The alignment is performed with GBL and MILLEPEDE-II [48]. In the case of a complete telescope (six planes), the tracks are built from the reconstruction of triplets in the upstream and downstream telescope planes. Firstly, a hit candidate from the outer plane is extrapolated by a horizontal straight line to the inner plane of one arm. Then, a triplet is formed if there is a matching between the middle plane of the arm and the doublet built. This is done on the two arms and a criterion ensures that two triplets are coming from the same track if the distance between the two extrapolated triplets at the middle z-position of the telescope is below a cut value. This was set to 10 μm. GBL forms a track from the six hits belonging to the matching triplets. The track candidates are then passed to MILLEPEDE-II, which determines the shift and the rotation to apply for aligning the sensors. This method is applied a couple of times, until the precision of the alignment reaches a submicron

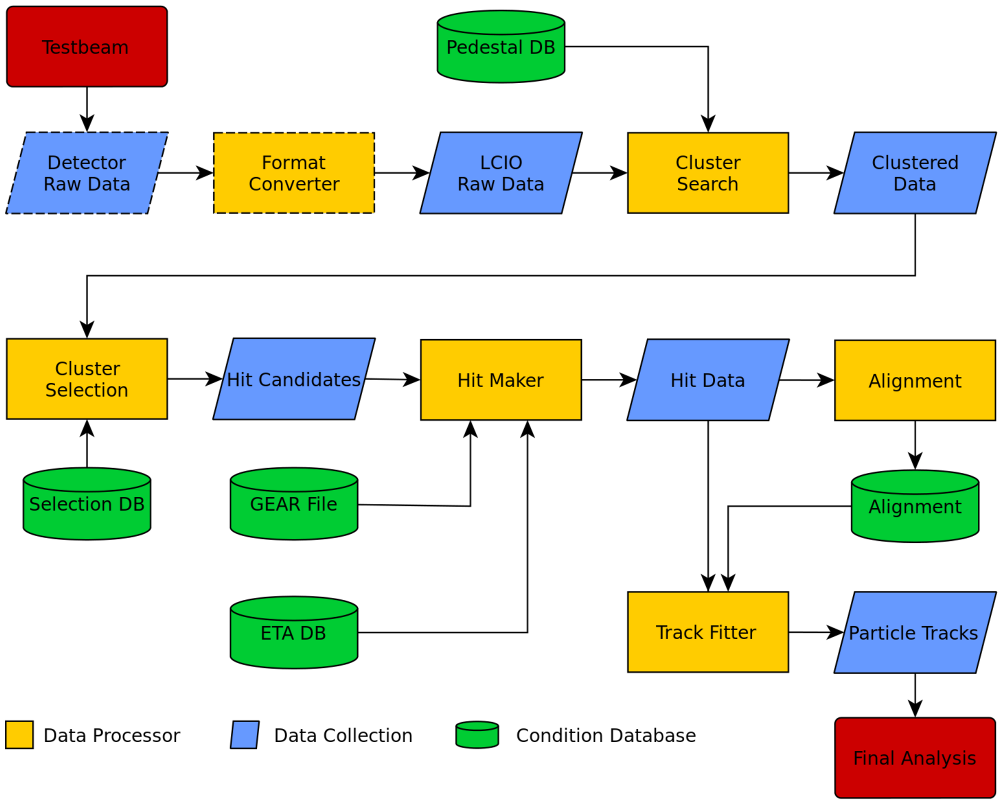

Figure 8.7 – Flow-chart of the analysis strategy by using EUTelescope [2].

order.

Nevertheless, due to the set-up used during the test beam and a limitation in EUTelescope on the number of telescope planes and the ID used, the alignment did not work for practical reasons. The number of telescope planes is hard-coded to be six and the sensor IDs in the range $[0; 5]$ are reserved for the telescope. Here, the IDs 0 and 1 are used for PLUME and the others for the telescope. Thus, a modification has to be applied to remap the sensor IDs. Although this solution can work and GBL uses only the z ordering information is used to create the tracks, EUTelescope is waiting for six hits.

Thankfully, a prototype software developed by Claus Kleinwort has permitted to perform the alignment and finish the analysis. It is based on GBL and MILLEPEDE-II and reads the hit information created by the hitmaker processor of EUTelescope. The modularity of the software allows to select the desire number of telescope planes. In the case of only four telescope planes, the triplets method is not used and tracks are formed only with doublets. Then, the track's information are feed to MILLEPEDE-II, which calculates the residuals of the tracks on each sensor and attempts to shift the position and rotate the sensors to minimise the east square fit function of these tracks. MILLEPEDE-II creates an output file with theses informations and a script update the GEAR file with the new position and orientation of each planes.

Alignment plots

8.3.2 Measurement of the radiation length

Theoretical estimation

The theoretical estimation of PLUME material budget was already discussed in chapter 5. The value defined in this chapter was a weighted radiation length, which takes into account the passive component and the insensitive areas. For the measurement done here, only the region over a sensitive surface is studied. There is no passive component and the beam is travelling through:

- Two MIMOSA-26 sensors thinned down to $\sim$ 50 μm and a material budget of $\left.\frac{x}{X_0}\right|_{\text{Mi26}} \sim 0.053$ % X_0,
- Four layers of glue (sensor/flex interface and flex/stiffener interface) with an estimated radiation length: $\left.\frac{x}{X_0}\right|_{\text{Glue}} \sim 0.01$ % X_0,
- Stiffener made of 8 % density SiC with a thickness of $\sim$ 2 mm and radiation length: $\left.\frac{x}{X_0}\right|_{\text{SiC}} \sim 0.184$ % X_0,
- Two flex-cables made of two copper layers insulated with three layers of Kapton:
  - Material budget for $\sim$ 50 μm of Kapton: $\left.\frac{x}{X_0}\right|_{\text{Kapton}} \sim 0.014$ % X_0,
  - Material budget for $\sim$ 14 μm of Copper: $\left.\frac{x}{X_0}\right|_{\text{Cu}} \sim 0.084$ % X_0.

It is assumed that the copper layers have a fill factor between 25 % and 30 %. Hence, the flex-cable material budget is: $\frac{x}{X_0}\Big|_{\text{Flex}} \sim 0.084 - 0.092$ % X_0, leading to a total radiation length of:

$$\begin{aligned} \frac{x}{X_0}\Big|_{\text{PLUME}} &= 2 \times \left(\frac{x}{X_0}\Big|_{\text{Mi26}} + \frac{x}{X_0}\Big|_{\text{Flex}} + 2 \times \frac{x}{X_0}\Big|_{\text{Glue}} \right) + \frac{x}{X_0}\Big|_{\text{SiC}}, \\ &\simeq 0.498 \ - \ 0.515 \ \% \ \mathrm{X_0}. \end{aligned} \tag{8.4}$$

Hence, the material budget expected is between 0.498 % X_0 and 0.515 % X_0.

Kink angle measurement

To measure the kink angle of the tracks, the four telescope planes, as well as the two PLUME sensors are used. So, the hit information provided by PLUME are exploited to create tracks by using the triplets method. The deviation from the incoming tracks and the outgoing ones (after the PLUME ladder) is measured with GBL, which provides information for xz and yz-angles. Figure 8.8 shows the distribution of the kink angle fitted by a Gaussian for an energy of 5 GeV and without a fiducial cut on a particular region of interest. For small deflection angles, the distribution is roughly Gaussian with larger tails than expected for a Gaussian distribution [60]. Therefore, the fit is performed in a range corresponding to the standard deviation of the distribution. To obtain θ_0, the width of the kink angle $\sigma_{\text{kink angle}}$ has to be corrected by the mean value of the kink angle fit $<$ kink angle $>$:

$$\theta_0 = \sqrt{\sigma_{\text{kink angle}}{}^2 - <\text{kink angle}>}. \tag{8.5}$$

From the equation 8.2 and by injecting θ_0 defined in equation 8.5, the radiation length $\frac{x}{X_0}$ is then:

$$\frac{x}{X_0} = \left(\frac{\sqrt{\sigma_{\text{kink angle}}{}^2 - <\text{kink angle}>} \cdot p}{13.6 \text{ (MeV)}} \right)^{\frac{1}{0.555}}. \tag{8.6}$$

The kink angle measured at 5 GeV is $\sim 1.95 \cdot 10^{-4}$ rad, leading to a radiation length of ~ 0.58 % X_0, which is over the estimated calculation.

This procedure has been repeated to the runs between 1 and 4 GeV (see figures 8.9 to 8.12) and the results of the measured kink angles as a function

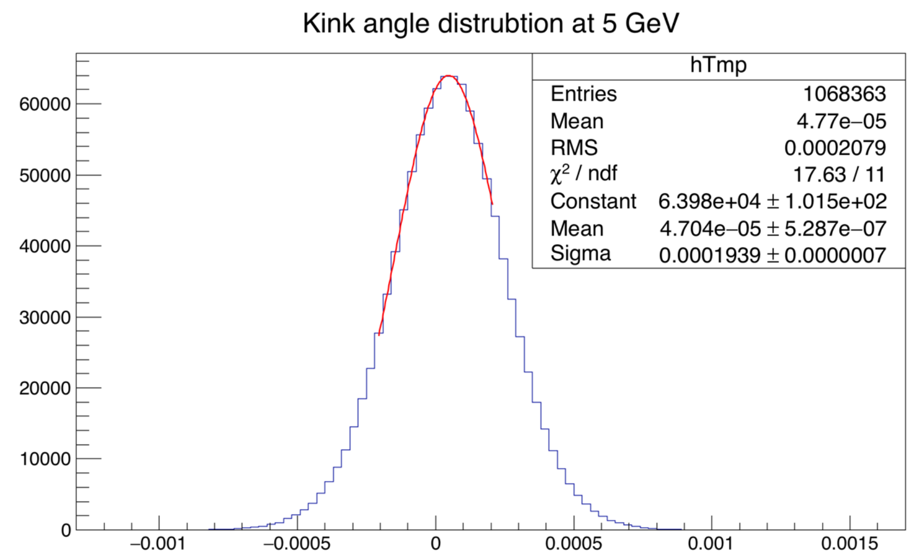

Figure 8.8 – Distribution of the kink angle given by GBL for an energy of 5 GeV without any fiducial cut. The asymmetric fit arises from a wrong alignment procedure.

of the beam momentum are represented on figure 8.13. The uncertainty on the momentum is 5 % and is the uncertainty determined at the DESY test beam facility, while the uncertainty used for the kink angle is extracted from the fit procedure corrected by the χ^2/NDF measured. The plot is then fitted with the Highland formula from equation 8.2, on which the radiation length is a free parameter. Two points (1 and 5 GeV) are outside the trend and the χ^2/ N.D.F measured is bigger than 1. Table 8.2 summarises the expected θ_0 for a radiation length of 0.5 % X_0 and compare this results to the measured θ_0.

The alignment of the 1 GeV runs are complicated to perform. At this energy, the electrons are more sensitive to the multiple scattering in the air and inside the detectors. At 5 GeV, the electrons suffer less from the multiple scattering but the alignment procedure did not work well. On figure 8.8, the distribution of the kink angle is not centered and the reason of this offset comes from a wrong alignment. For the rest of the study, this two measurements are excluded to determine the radiation length, as seen on figure 8.14. The radiation length measured is then 0.47 ± 0.02 % X_0, smaller than the expected calculation. The determination of the material budget is done here without taking into account the complete ladder. The PLUME

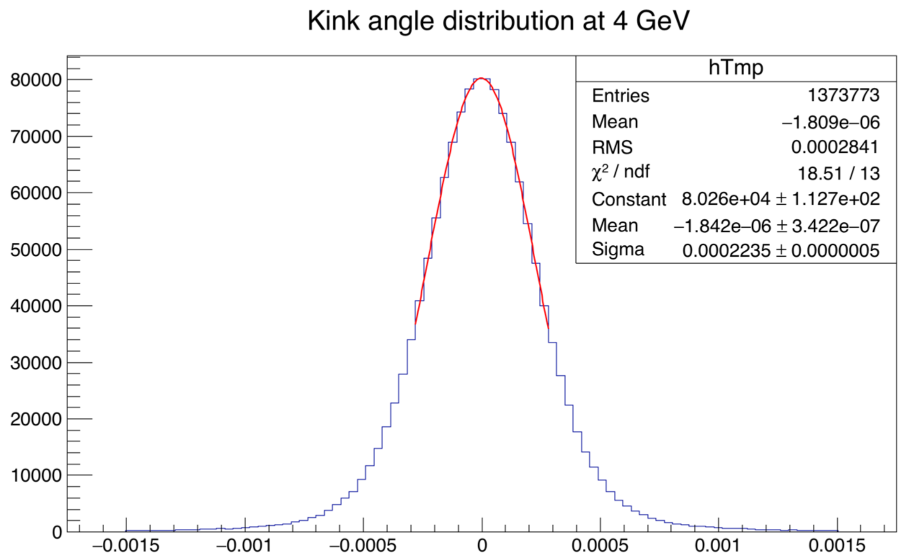

Figure 8.9 – Distribution of the kink angle given by GBL for an energy of 4 GeV without any fiducial cut.

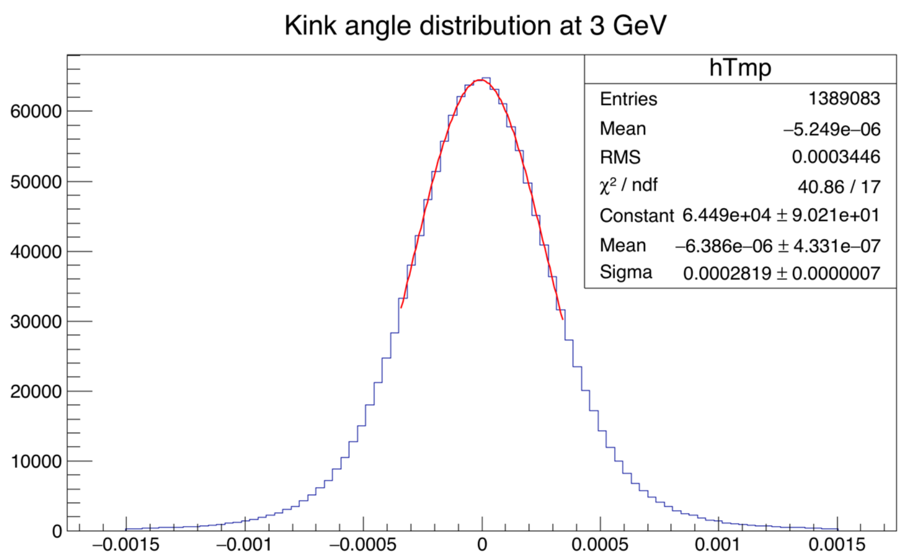

Figure 8.10 – Distribution of the kink angle given by GBL for an energy of 3 GeV without any fiducial cut.

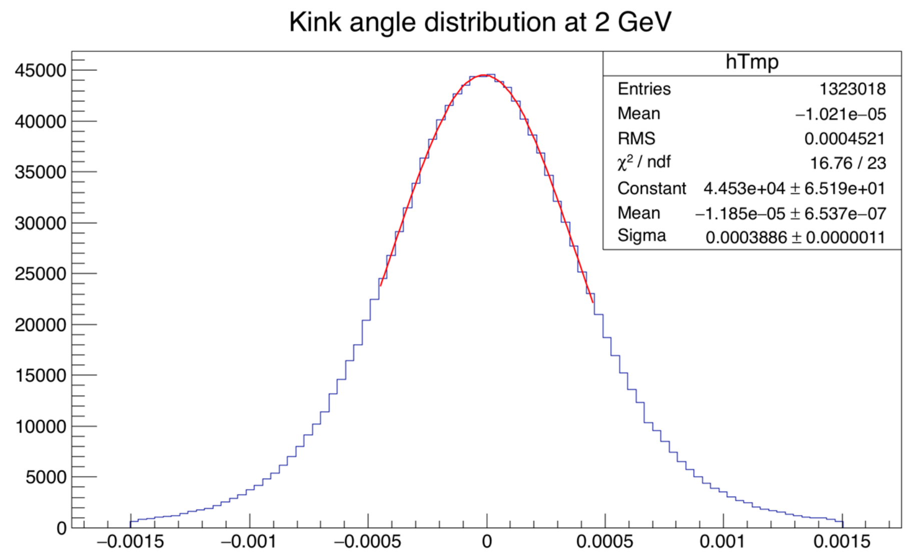

Figure 8.11 – Distribution of the kink angle given by GBL for an energy of 2 GeV without any fiducial cut.

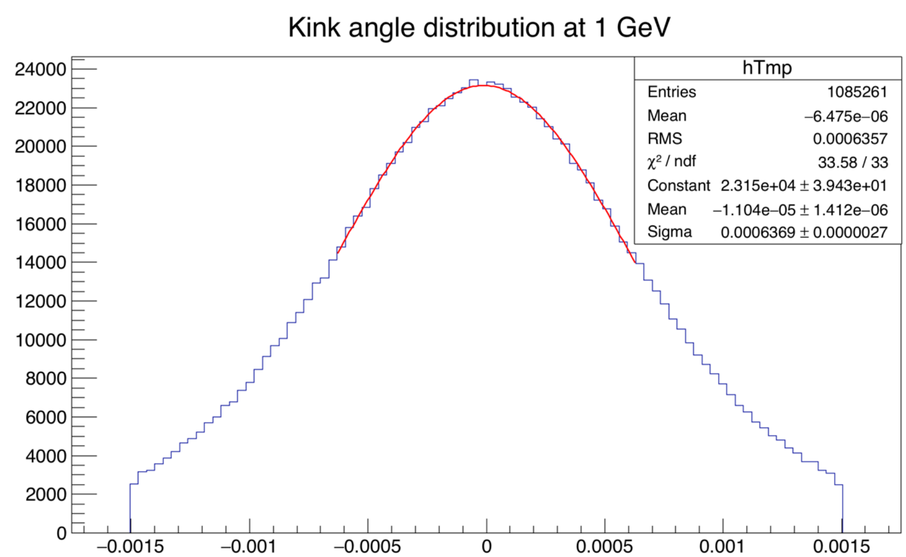

Figure 8.12 – Distribution of the kink angle given by GBL for an energy of 1 GeV without any fiducial cut.

Energy (GeV)	$\theta_0\|_{\mathrm{expected}}$ (rad)	$\theta_0\|_{\mathrm{measured}}$ (rad)
1	$7.186 \cdot 10^{-4}$	$5.740 \cdot 10^{-4} \pm 2.783 \cdot 10^{-6}$
2	$3.592 \cdot 10^{-4}$	$3.337 \cdot 10^{-4} \pm 7.764 \cdot 10^{-7}$
3	$2.395 \cdot 10^{-4}$	$2.380 \cdot 10^{-4} \pm 1.610 \cdot 10^{-6}$
4	$1.796 \cdot 10^{-4}$	$1.821 \cdot 10^{-4} \pm 7.483 \cdot 10^{-7}$
5	$1.437 \cdot 10^{-4}$	$1.549 \cdot 10^{-4} \pm 1.136 \cdot 10^{-4}$

Table 8.2 – Determination of $\theta_0|_{\mathrm{expected}}$ for a material budget of 0.5 % X_0 and comparison to $\theta_0|_{\mathrm{measured}}$.

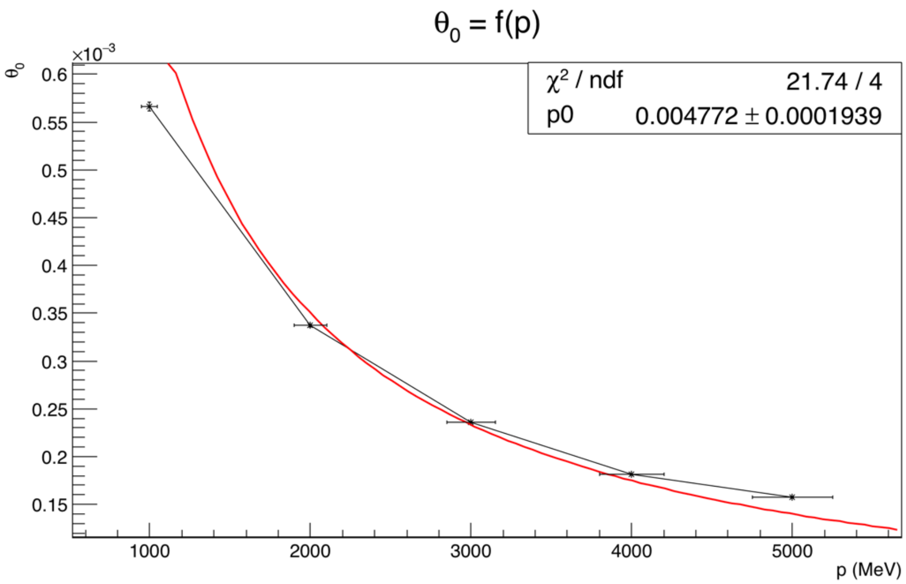

Figure 8.13 – Dependence of the measured standard deviation of the kink angle with the energy, over the full range of the energies used. Superimposed is a fit using the Highland formula where the radiation length is left as a free parameter.

sensors are used for tracking and measuring the kink angle. As the signal is considered to be created in the middle of the epitaxial layer, only one part of the MIMOSA-26 is included in the calculation. The thickness of the different MIMOSA-26 layers are the followings:

- Electronics layer: $\sim 6\ \mu$m,
- Epitaxial layer: $\sim 14\ \mu$m,

- Bulk: $\sim 30\ \mu$m.

The sensors are thinned down to $50 \pm 2\ \mu$m, but only $\sim 37\ \mu$m of silicon are taken into account during the calculation. In total, 0.028 % X_0 are missing in the calculation.

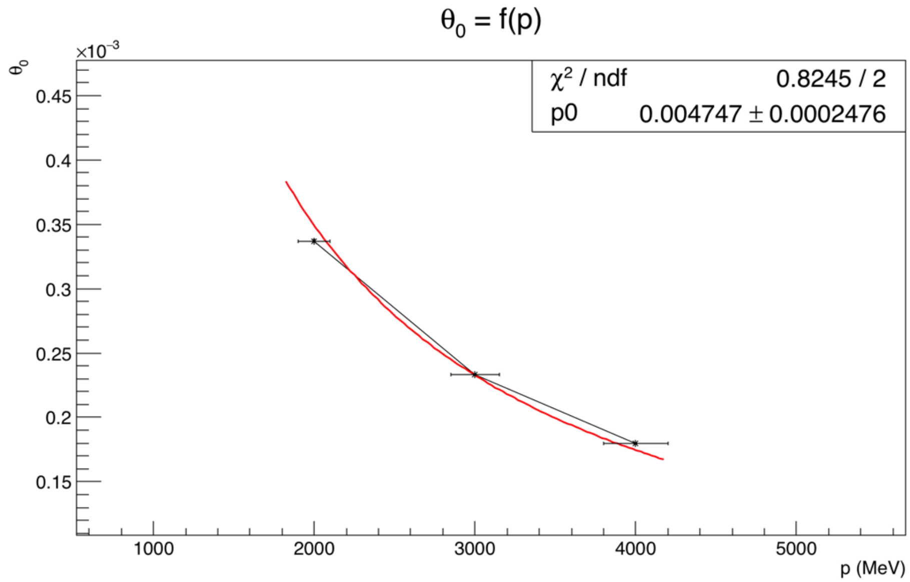

Figure 8.14 – Extrapolation of the kink angle with the energy, over a restricted range of the energies used. Superimposed is a fit using the Highland formula, where the radiation length is left as a free parameter.

To insure that the measurement is correct, the different radiation lengths measured are plotted as a function of the momentum (see figure 8.15). Although the fit shows a dependency on the momentum, the error on the second polynom is larger than the value determined by the fit. The different radiation lengths determined at different momentum are of the same order and this is consistent with the definition of the material budget.

8.4 Conclusions

The radiation length measurement of the PLUME ladder was performed for the first time with a dedicated setup placed in beam. The first results obtained to determine the material budget, which gives a radiation length of

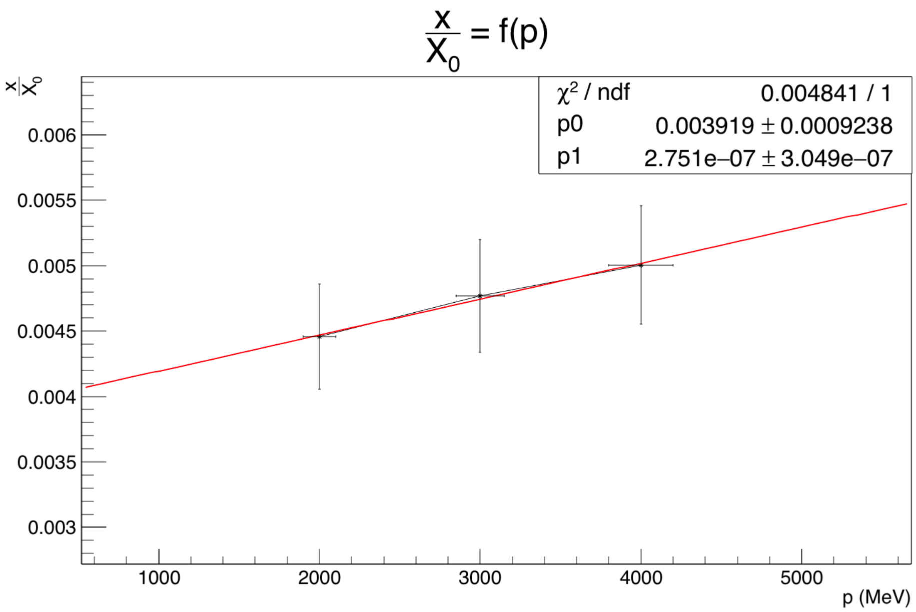

Figure 8.15 – Measured radiation lentgh $\frac{x}{X_0}$ as a function of the momentum p.

$\left.\frac{x}{X_0}\right|_{\text{measured}} \simeq 0.47 \pm 0.02$ % X_0 are confirming the theoretical calculation of $\left.\frac{x}{X_0}\right|_{\text{theoretical}} \simeq 0.498$ % X_0 for a flex with a fill factor of 25 %. The origin of the shifts on the measured radiation length at 1 and 5 GeV has to be investigated. In both cases, the alignment has to be done again. Another solution consists to perform a calibration run with a known material to apply then a correction on the radiation length measurement for PLUME.

Conclusions

This thesis was performed in the context of the ILC. This work addresses is mainly focused on the detector development for ILD and gives different steps from the construction of a double-sided vertex detector to the test in real conditions.

Although the physics studied at the ILC is presented, the thesis focuses on the detector development and presents different steps of this development.

Firstly, the physics program of the ILC was introduced and a physics analysis was presented.

Secondly, the history of the PLUME development was presented. The basic assessments were explained.

Thirdly, the study of the mechanical deformation

Finally, the radiation length measurement

Chapter 9

Résumé de la thèse

9.1 Contexte de la thèse

Le 4 juillet 2012 au CERN à Genève (Suisse), les collaborations ATLAS et CMS ont annoncé les premiers résultats d'analyse des données acquises grâce au plus grand accélérateur de particules du monde, le Large Hadron Collider (LHC)[15][16]. Les deux expériences ont présenté la découverte de la signature d'une particule compatible avec le boson prédit par le mécanisme de la brisure de la symétrie électro-faible de Brout-Englert-Higgs, le boson de Higgs. Bien que l'augmentation de l'énergie de collision du LHC pourrait permettre une meilleure compréhension de cette nouvelle particule et de contraindre encore plus les limites du Modèle Standard, voire de découvrir des traces de physique au delà de cette théorie, la complexité des évènements générés limite l'accès à certains paramètres fondamentaux.

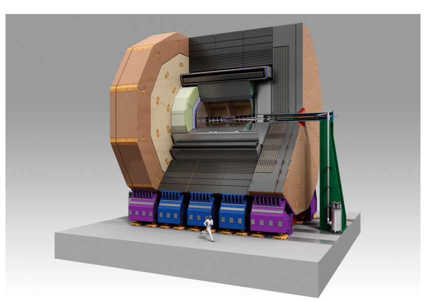

Figure 9.1 – Schéma de l'ILD, un des deux détecteurs prévus à l'ILC.

Un nouveau grand projet en physique des hautes énergies est à l'étude

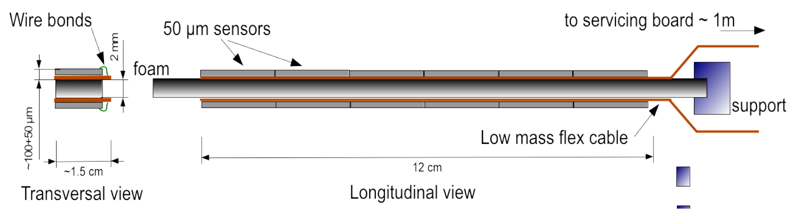

Figure 9.2 – Schéma du principe final de l'échelle PLUME.

: International Linear Collider (ILC). Ce collisionneur linéaire de 31 kilomètres de long permettra la collision d'électrons et de positrons à une échelle d'énergie comprise entre 250 GeV et 500 GeV et ultérieurement 1 TeV, pour des polarisations différentes. Grâce à l'étude des collisions électrons/positrons reposant sur l'identification complète des processus quantiques de chaque évènement, ce nouveau collisionneur devrait permettre de mieux caractériser les particules déjà connues, comme le boson de Higgs grâce à son couplage avec les fermions, mais aussi d'étudier la matière noire. Pour cela la partie centrale du détecteur, dédiée à la reconstruction des chaînes de désintégration survenues avant la première couche instrumentée, doit avoir à la fois une excellente résolution spatiale et un budget de matière (X_0) ne dépassant pas quelques millièmes de la longueur de radiation. Ce sous-détecteur, appelé détecteur de vertex, doit être optimisé afin de permettre la trajectométrie dans un milieu hautement dense en particules et de différencier la trajectoire des quarks b et c.

La collaboration PLUME, qui implique l'IPHC de Strasbourg, le DESY à Hambourg et l'université de Bristol, met en place les outils permettant de surmonter ces défis grâce à une conception innovante d'échelles de trajectométrie double face pixelisée, appelée PLUME[1][61]. Ce type d'objet est équipé de six capteurs à pixels CMOS ultra fins (amincis à $\sim 50\ \mu$m), alignés l'un à côté de l'autre, sur chaque face d'un support mécanique très léger et tente d'atteindre un record au niveau du budget de matière en se rapprochant de 0.35 % X_0. La figure 9.2 est un schéma représentant le principe d'une échelle double face développée par la collaboration. Pour chaque trajectoire, deux positions seront mesurées, une par face. Elles permettront d'évaluer le point d'intersection de la particule avec le détecteur, mais aussi son mouvement et son origine. Si les outils permettant cette double mesure sont maitrisés et optimisés, cela augmentera considérablement les capacités de trajectométrie de ce type d'instrument.

[1]**P**ixelated **L**adder with **U**ltra low **M**aterial **E**mbeded

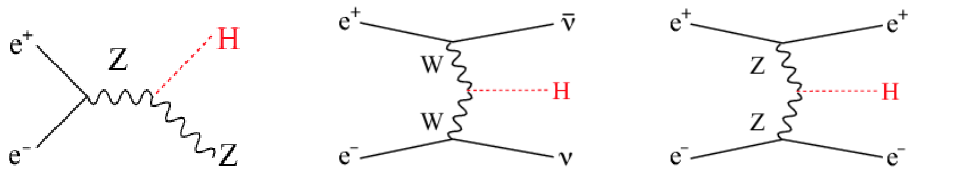

(a) Higgs-Strahlung. **(b)** Fusion de bosons W. **(c)** Fusion de bosons Z.

Figure 9.3 – Diagrammes de Feynman des principaux processsus de production du boson de Higgs à l'ILC[4][70].

Ma thèse vise à participer à la construction de la seconde génération de détecteurs de PLUME et à caractériser leurs performances.

9.2 Étude (simpliste) de la désintégration du boson de Higgs

Afin de comprendre les paramètres du système de détection, j'ai démarré une analyse de physique concernant la désintégration du boson de Higgs en deux paires de quarks charmé et anti-charmé à une énergie de centre de masse de 350 GeV à l'ILC, avec des données simulées par méthode Monte Carlo.

Contrairement aux canaux de production du boson de Higgs disponible au LHC, l'ILC est capable de produire directement le Higgs, soit par Higgs-strahlung (voir figure 9.3a), soit par la fusion de bosons W (voir figure 9.3b) ou alors par la fusion de bosons Z (voir figure 9.3c). Néanmoins, à 350 GeV, seulement le Higgs-strahlung et la fusion WW sont observables. Je me suis tout particulièrement intéressé à l'état final comportant un boson de Higgs et deux neutrinos. Ces canaux de production permettent une observation particulièrement précise des propriétés du boson de Higgs. En effet, les particules détectées dans l'état final proviennent uniquement de la désintégration du boson de Higgs. Par ailleurs, la production via Higgs-strahlung autorise une étude du boson de Higgs sans considérations des produits de désintégrations, en étudiant simplement la masse de recule.

L'étude m'a d'abord permis de comprendre l'avantage de la polarisation des électrons et positrons sur le canal de physique que l'on souhaite étudier. Par exemple, la contribution de la fusion de bosons W est atténuée lorsque les électrons sont droits et les positrons gauches. Cependant, le signal étudié est noyé dans un bruit de fond généré pas d'autres processus. Deux bruits de fonds sont considérés, ceux menant à un état final identique à notre signal,

Processus	Bruit	Signal	Significance
Section efficace (fb)	$5.69 \cdot 10^4$	$6.82 \cdot 10^2$	
Nombre d'évènements	$1.88 \cdot 10^7$	$2.25 \cdot 10^4$	5.2
Sans leptons isolés	$1.65 \cdot 10^7$	$2.23 \cdot 10^4$	5.5
$35 < \mathrm{P_t^{vis}} < 155$ GeV	$9.31 \cdot 10^5$	$1.82 \cdot 10^4$	18.7
$95 < \mathrm{m_{vis}} < 140$ GeV	$1.50 \cdot 10^5$	$1.66 \cdot 10^4$	40.6
$-1 < \cos\alpha < 0.22$	$8.76 \cdot 10^4$	$1.57 \cdot 10^4$	48.8
$26 <$ (N.R.C $>$ 1GeV) < 99	$2.25 \cdot 10^4$	$1.19 \cdot 10^4$	56.3
$0.11 <$ DurhamjD2ym < 1	$1.78 \cdot 10^4$	$1.05 \cdot 10^4$	62.3
$0 <$ abs(RefinedjPzvis) < 113 GeV	$1.51 \cdot 10^4$	$1.01 \cdot 10^4$	63.5
$156 <$ RefinedjEmiss < 230 GeV	$1.37 \cdot 10^4$	$9.85 \cdot 10^3$	64.1

Table 9.1 – Sélection du signal sur le bruit en appliquant différentes coupures consécutives pour une polarisation faisceau $\mathcal{P}_{e^-,e^+} = (-0.8, +0.3)$.

ou alors ceux produisant une réponse dans le détecteur similaire à celle du signal. Afin de différencier le signal du bruit, certains critères doivent être définis. Tout d'abord, nous nous attendons à observer deux jets provenant de la désintégration du boson de Higgs. Ainsi, tous les évènements ne contenant qu'un lepton isolé ne sont pas pris en compte. Puis, une sélection sur l'impulsion transverse visible est effectuée afin de réduire l'impact des hadrons produits par interaction $\gamma\gamma$. Ensuite, les évènements sont sélectionnés par rapport à l'hypothèse sur la structure de notre signal. Par exemple, la masse visible doit correspondre à la signature du boson de Higgs, qui est de 125 GeV. La résolution de ce paramètre dépend de la résolution en énergie des jets. D'autres paramètres sont utilisés comme par exemple l'angle entre les deux jets $\cos\alpha$. Un critère, appelé significance, permet de déterminer la qualité d'une coupure et est défini par :

$$\text{significance} = \frac{\text{signal}}{\sqrt{\text{signal} + \text{bruit}}} \tag{9.1}$$

Ainsi, si le bruit de fond est dominant, la valeur de la significance sera faible. Le tableau 9.1 représente le nombre d'événements correspondants au bruit et au signal après avoir appliqué plusieurs coupures. La significance augmente d'un facteur 10 après les trois sélections (nombre de leptons isolés, impulsion transverse, masse visible et angle entre les deux jets). Le bruit est ainsi diminué d'un facteur de plus de 200 et le signal qui nous intéresse a lui aussi été diminué, mais d'un facteur 1.4.

La suite de ce travail consiste a étudier la capacité d'identifier les quarks charmés pour différentes géométries de détecteur de vertex. Malheureusement, dû au temps qui m'a été imparti pour effectuer cette thèse, je n'ai pu effectuer cette étude.

9.3 Préparation d'une campagne de tests sous faisceaux

Comme décrit en introduction, l'objectif de la collaboration PLUME est d'atteindre un budget de matière se rapprochant de 0.35 % X_0 pour une résolution spatiale meilleure que 4 microns. La structure mécanique est validée grâce à l'utilisation de MIMOSA-26, des détecteurs monolithiques complexes qui ont une résolution spatiale de < 4 μm. Le traitement des données est directement intégré dans les photocites qui collectent les charges. Il permet de numériser directement le signal, grâce à des discriminateurs et de réduire la bande-passante de transmission des données par le biais d'un système de suppression de zéro (ne prend pas en compte les zéros envoyés par les pixels, qui ne représentent pas un signal physique intéressant). Cette méthode permet d'enregistrer les informations individuelles de plus de un million d'impacts/cm^2/s sur un capteur contenant plus de 500000 pixels sur une surface de 2 cm^2.

9.3.1 Validation en laboratoire des échelles PLUME

Les échelles PLUME sont les premiers prototypes double faces associant un budget de matière se rapprochant de 0.35 % X_0 et des pistes métallisées adaptées à la surface de détection de 1×12 cm^2, afin de réduire les zones mortes du détecteurs. Chaque module doit être validé en laboratoire afin de s'assurer que l'assemblage n'altère pas les capteurs utilisés. Après une inspection visuelle afin de contrôler l'alignement de chaque capteur l'un par rapport à l'autre et qu'aucun d'eux, ni aucune connexion n'ait été endommagé pendant l'assemblage, chaque échelle est testée électriquement. La consommation des capteurs, le contrôle JTAG ainsi que la présence de pixels morts sont vérifiés, pour ensuite évaluer les seuils des comparateurs qui vont permettre de discriminer le signal du bruit. Leur point de fonctionnement optimal, leur bruit et piédestaux sont obtenus grâce à une courbe de transfert qui représente la réponse des comparateurs à différents seuils et permet de définir un seuil où le bruit du capteur est supprimé sans en altérer ces capacités de détection. Ensuite, les propriétés de détection de ces capteurs sont contrôlés grâce à une analyse qui permet de déterminer le taux de fantôme de chaque capteur et de vérifier qu'ils détectent correctement une source radioactive.

9.3.2 Étude de la déformation des échelles lors d'une campagne de faisceau test

Actuellement, différentes versions des échelles PLUME existent : celles dont le budget de matière est de 0.65 % X_0 utilisant uniquement des pistes métallisées en cuivre; deux nouveaux prototypes, l'un utilisant des pistes métallisées en cuivre et l'autre en aluminium et dont les zones mortes de détection ont été réduites et la densité de la mousse mécanique a été diminuée de moitié. Bien que différentes versions existent, seuls les modules atteignant un budget de matière de 0.65 % X_0 ont été étudiés lors de deux campagnes en faisceau test, l'une réalisée par la collaboration en 2011 au CERN et l'autre que j'ai mené en avril 2016 au DESY. Les résultats de la première campagne ont permis à la collaboration de mettre en avant les avantages d'une double mesure. De ces résultats, je me suis intéressé à l'étude des déformations mécaniques de nos échelles et leur impact sur les résultats d'analyse. En effet, lorsque l'échelle est inclinée dans une direction et que le faisceau ne la touche plus en incidence normale, la résolution spatiale se dégrade dans des proportions inattendues. Ce comportement est dû aux contraintes mécaniques qui induisent des déformations permanentes de quelques dizaines de micromètres de la surface ne pouvant être contrôlées lors de l'assemblage. Apprendre à quantifier ces déformations et les prendre en compte pendant notre analyse est essentiel pour valider nos prototypes. Les capteurs sont modélisés par une surface parfaitement plane. Or, la position de ces plans en trois dimensions est différente puisque ceux-ci peuvent être plus ou moins déformés. Ainsi comme il a été observé, la distribution du résidu, ou distance entre la position du pixel touché et de la trace extrapolée, devient plus importante lorsque l'angle d'incidence n'est plus normal à la surface du détecteur. Il faut donc prendre en compte cette déformation dans notre analyse afin de recalculer la position exacte de chaque pixel en 3 dimensions et l'extrapolation exacte sur le plan de la trajectoire. Grâce à une première étude réalisée par un doctorant du groupe PICSEL et un article de la collaboration CMS sur l'alignement du trajectomètre[1], il m'a été possible de mettre en place un algorithme permettant de déterminer la forme de notre capteur à l'aide de polynômes de Legendre. En prenant en compte l'angle d'incidence des particules, la résolution spatiale est améliorée. Par exemple, l'analyse d'une acquisition où le module PLUME est incliné de 36° , a mis en évidence une déformation en corrélant le résidu à la position de l'impact sur la matrice de détection, par rapport à une acquisition où le plan est en incidence normale. En ajustant la figure 9.4a par un polynôme de Legendre, les coefficients obtenus permettent de paramétrer la surface du capteur et ainsi de minimiser le résidu, comme montré sur la figure 9.4b. La déviation standard de la distribution des résidus, qui définit la résolution spatiale, passe de 14.1 μm à 6.2 μm. En prenant en compte la résolution du télescope qui est de 1.8 μm, la résolution atteinte par notre capteur est d'environ 5.9 μm.

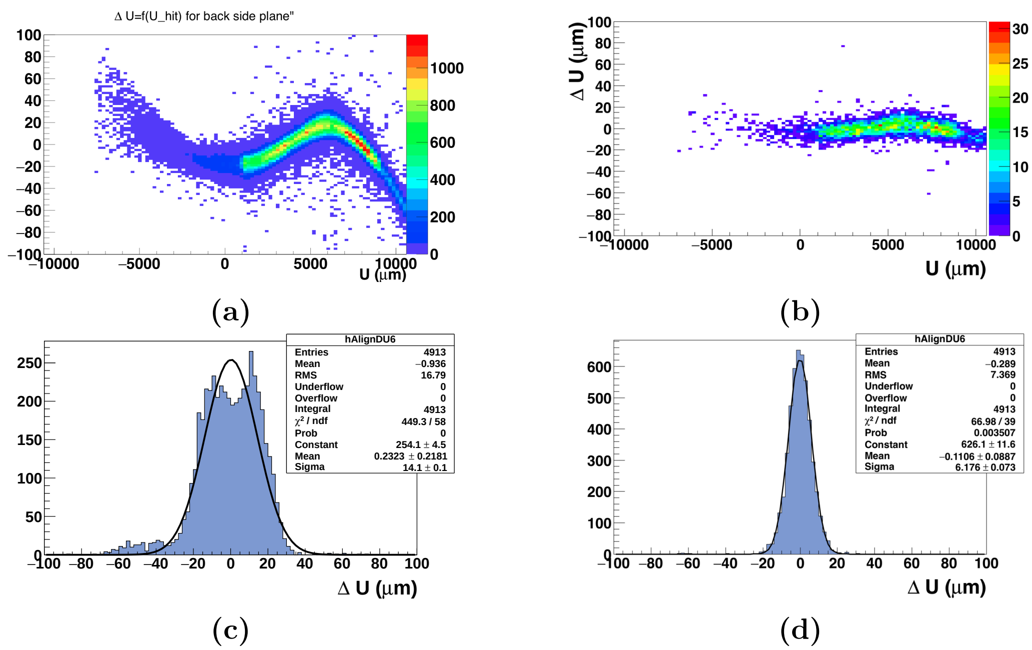

Figure 9.4 – Résultat de l'analyse de l'échelle inclinée à 36° : 9.4a résidus point d'impact/trace selon la direction u en fonction de la position du point d'impact dans la même direction avant la correction, 9.4b résidu selon u en fonction du point d'impact dans la même direction après prise en compte de la déformation, 9.4c distribution des résidus point d'impact/trace avant correction et 9.4d distribution des résidus après correction.

9.3.3 Estimation du budget de matière avec des électrons de basse énergie

Nos échelles doivent avoir des performances similaires à basse énergie à celles obtenues lors du précédent faisceau test. En effet, le détecteur de vertex doit être capable de mesurer les particules qui ont une grande impulsion, ainsi que celles qui ont une faible impulsion et qui ne pourront être détectées par les autres parties de ce détecteur. C'est pourquoi, j'ai préparé et effectué une deuxième campagne de faisceau test avec des électrons de quelques GeV au DESY en avril 2016. Avant de réaliser cette expérience, il m'a fallu m'assurer de l'intégration de notre détecteur au sein du système d'acquisition EUDAQ fourni par le DESY. Un outil de simulation estimant la résolution spatiale en fonctions de différentes géométrie de télescope m'a permis de définir une géométrie optimale pour étudier à la fois les caractéristiques attendues de l'échelle, mais aussi de pouvoir déterminer son budget de matière et le comparer aux attentes théoriques. Comme la technologie des capteurs utilisés pour le télescope et PLUME sont les mêmes, le système d'acquisition a été simplifié : deux plans de télescopes sont positionnés de part et d'autres du détecteur afin de mesurer la trajectoire des particules. Des mesures de plusieurs heures ont permis de vérifier la stabilité du système d'acquisition. En même temps, un support rotatif a été construit afin de maintenir l'échelle à la position verticale et de permettre une prise de données pour des angles variants de 0° à 60°. La figure 9.5 est une photographie prise durant la campagne de faisceau test et montre le positionnement de l'échelle PLUME, située au centre entre les quatre plans de référence.

Un des objectifs de ce faisceau test est de mesuré le budget de matière de l'échelle PLUME. En effet, seul des calculs théoriques ont permis de déterminer cette valeur cruciale dans la fabrication d'un détecteur de vertex. Les particules chargées traversant un milieu sont défléchies par par de multiples diffusions coulombiennes à petits angles causées par les noyaux de la cible. Cette déviation est appelée *Diffusion Multiple de Coulomb*. La projection de l'angle de déflexion dépend de l'énergie de la particule incidente ainsi que du matériau. Cet angle est calculé par :

$$\theta_0 \simeq \frac{13.6\text{ MeV}}{\beta c p} \left(\frac{x}{X_0} \right)^{0.555}, \tag{9.2}$$

de la manière suivante :

où, $\beta = v/c$, p est l'impulsion de la particule en MeV, x la distance parcourue et X_0 la longueur de radiation du milieu. Ce processus agissant un grand nombre de fois le long du parcours des particules dans la matière, cela a pour effet une déflexion de leur trajectoire par rapport à la direction initiale. Ainsi, grâce aux plans de référence utilisés en faisceau test, il est possible de mesurer le passage des particules avant et après avoir traversé notre échelle PLUME. En mesurant l'angle entre la trace incidente et la trace sortante, il est possible d'estimer le budget de matière du module. La mesure a été réalisée au niveau d'une zone comportant des capteurs sur l'échelle PLUME, pour des positrons ayant une énergie variant de 1 à 5 GeV. Les premiers

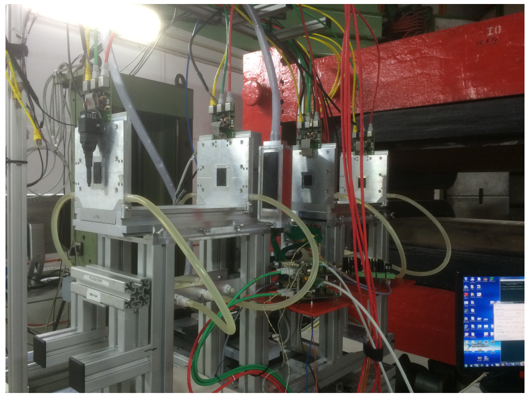

Figure 9.5 – Photo prise pendant la campagne de faisceau test au DESY. L'échelle PLUME est montée sur un support rotatif et est située entre les quatre plans de référence.

résultats ont permis de calculer un budget de matière d'environ 1.3 % X_0. Bien que le résultat valide le concept de l'expérience, le budget de matière de ce prototype est estimé à 0.65 % X_0 pour la zone étudiée. Le facteur 2 peut être gagné en améliorant l'alignement hors-ligne du système, mais aussi en effectuant une mesure de calibration avec un matériau dont le budget de matière est précisément connu.

9.4 Conclusions

Au cours de mon travail de thèse, j'ai pu étudier l'intérêt d'un collisionneur linéaire électrons/positrons afin de réaliser des mesures précises des propriétés du boson de Higgs. Je me suis tout particulièrement intéressé à un canal de désintégration inaccessible au LHC où l'état final comporte le boson de Higgs ainsi que deux neutrinos. Les différents critères permettant de différencier le signal étudié du bruit ont été étudiés grâce à des sélections sur la région d'intérêt. Malheureusement, le temps qui m'a été imparti pour réaliser mes travaux ne m'a pas permis d'étudier les performances d'identification des quarks charmés pour différentes géométries de détecteur de vertex.

Ma recherche c'est principalement concentrée sur de l'étude et de la validation des premiers concepts d'échelles de détections double faces atteignant un budget de matière de seulement 0.35 % X_0. Un banc de validation a été mis en place au DESY et a permis de vérifier que les performances des capteurs utilisés ne sont pas impactées par la structure unique de ces échelles.

Par ailleurs, les résultats de la campagne en faisceau test effectuée au CERN en 2011 ont permis de mettre en évidence l'impact de la déformation des capteurs sur la résolution spatiale de notre échelle lorsque celle-ci ne se trouve plus en incidence normale. L'algorithme développé qui utilise des polynômes de Legendre pour extrapoler la position des capteurs en trois dimensions a permis de réduire l'impact des déformations sur les résultats d'analyse en faisceau test. Bien que les résultats soient encourageants, l'algorithme peut-être amélioré en utilisant une méthode itérative afin de déterminer plus précisément la position de l'impact sur le capteur.

Enfin, grâce au faisceau délivré par le DESY, ainsi que différents logiciels d'analyse ont permis à la collaboration de réaliser pour la première fois la mesure du budget de matière de nos échelles. Les premiers résultats devraient être obtenus afin la soumission du manuscrit et présentés lors de la soutenance de thèse.

Le travail effectué au cours de ces trois années sont prometteurs pour une utilisation des échelles PLUMES dans le cadre de l'ILC. D'autres applications sont par ailleurs possibles, comme son utilisation pour l'estimation des conditions de bruit de fond machine dans l'expérience BEAST, juste avant le démarrage de Belle-II.

Publications et conférences

Conférences :

- *3rd Beam Telescopes and Test Beams Workshop*, Janvier 2015, DESY - Hambourg (Allemagne); présentation orale
  "Observing and correcting the surface deformation of light pixelated detection surface"

- *2015 International Workshop on Future Linear Colliders (LCWS15)*,Novembre 2015, Whistler (Canada); présentation orale
  "Double-sided pixelated layers studies from the PLUME collaboration"

Publication :

B. Boitrelle, J. Baudot, G. Claus, O. Clausse, L. Cousin, R. Gauld, M. Goffe, J. Goldsteind, I.M. Gregor, M. Imhoff, U. Koetz, R. Maria, A. Nomerotski, R. Page, M. Szelezniak and M. Winter "The PLUME performance evaluation" (en préparation)

Formations

- Linear Collider Physics School[2] au DESY à Hambourg du 7 au 9 octobre 2013
- 7^{th} Detector Workshop of the Terascale Alliance[3] à Göttingen du 3 au 5 mars 2014
- Introduction to Terascale 2014[4] au DESY à Hambourg du 17 au 21 mars 2014
- Linear Collider School 2014[5] à Frauenchiemsee du 11 au 15 août 2014
- Introduction school on thermal and mechanical simulations based on finite-element calculations à Berlin du 2 au 4 Mars 2015
- Cours d'allemand au DESY, septembre 2013 à février 2014 (3 heures par semaine)
- Cours d'allemand avec la PIER school depuis avril 2015 (1 heure 30 par semaine)

[2] https://indico.desy.de/conferenceDisplay.py?confId=7513
[3] https://indico.desy.de/conferenceDisplay.py?confId=9389
[4] https://indico.desy.de/conferenceDisplay.py?confId=9263
[5] https://indico.desy.de/conferenceDisplay.py?confId=9329

Acronyms

AHCAL Analogue HCAL. 38

APS Active Pixel Sensor. 61

ASIC Application-Specified Integrated Circuit. 61

BDS Beam Delivery System. 27

BEAST Beam Exorcism for A Stable experiment. 68

CCD Charged Coupled-Device. 61

CDS Correlated Double Sampling. 76

CERN Centre Européen pour la Recherche Nucléaire. 24

CLIC Compact LInear Collider. 26

CMOS Complementary Metal Oxide Semi-conductor. 57

DAQ Data AcQuisition. 62

DC Direct-current. 27

DEPFET Depleted P- Channel Field Effect Transistor. 61

DESY Deutsches Elektronen-Synchrotron. 26

DUT Device Under Test. 102

ECAL Electromagnetic CALorimeter. 35

EM electromagnetic interaction. 3

ETD End-cap Tracking Detector. 35

EW electroweak. 7

FPCCD Fine Pixels Charged Coupled-Device. 61

FPN Fixed Pattern Noise. 76

FTD Forward Tracking Detector. 35

GBL General Broken Lines. 127

GEAR GEometry Api for Reconstruction. 48

GRPC Glass Resistive Plate Chamber. 38

GUT Great Unification Theory. 20

HCAL HAdronic CALorimeter. 37

ICFA International Committee for Future Accelerators. 26

ILC International Linear Collider. 1

ILD International Large Detector. 2

IP interaction point. 30

IPHC Institut Pluridisciplinaire Hubert Curien. 61

IR interaction region. 27

ISR Initial State Radiation. 48

JTAG Joint Test Action Group. 86

LCIO Linear Collider I/O. 48

LEP Large Electron Positron collider. 39

LHC Large Hadron Collider. 1

LHCAL Low angle Hadron CALorimeter. 38

MAPS Monolithic Active Pixel Sensor. 37

Marlin Modular Analysis and Reconstruction for the LINear collider. 48

MIMOSA Minimum Ionizing MOS Active pixel sensor. 61

MIP Minimum Ionizing Particle. 69

MVA multivariate analysis. 54

OKF Optiprint-Kapton-Flex-cable. 65

PFA Particle Flow Algorithm. 32

PICSEL Physics with Integrated Cmos Sensors and ELectron machines. 62

PLUME Pixelated Ladder with Ultra-low Material Embedding. 1

PMT Photomultiplier Tube. 130

QCD Quantum Chromodynamics. 10

QED Quantum Electrodynamic. 8

QFT Quantum Field Theory. 7

RTML Ring To the Main Linac. 28

SDHCAL Semi-Digital HCAL. 38

SET Silicon External Tracking. 35

SiC Silicon Carbide. 63

SiD Silicon Detector. 32

SIT Silicon Internal Tracker. 35

SM Standard Model. 1

SNR Signal to Noise ratio. 77

SRF Superconducting Radio-Frequency. 26

SUSY Supersymmetry. 20

SUZE Suppression de zéro. 75

TAF TAPI Analysis Framework. 97

TLU Trigger Logic Unit. 128

TN Temporal Noise. 76

TPC Time-Projection-Chamber. 32

VXD Vertex Detector. 2

ZIF Zero Insertion Force. 63

Bibliography

[1] Alignment of the CMS tracker with LHC and cosmic ray data. pages 1748–221, 1088.

[2] About eutelescope analysis strategy. http://eutelescope.web.cern.ch/content/about-eutelescope.

[3] R. Appleby, L. Keller, T. Markiewicz, A. Seryi, R. Sugahara, and D. Walz. The International Linear Collider Technica. 3, 2006.

[4] D. M. Asner, T. Barklow, C. Calancha, K. Fujii, N. Graf, H. E. Haber, A. Ishikawa, S. Kanemura, S. Kawada, M. Kurata, A. Miyamoto, H. Neal, H. Ono, C. Potter, J. Strube, T. Suehara, T. Tanabe, J. Tian, K. Tsumura, S. Watanuki, G. Weiglein, K. Yagyu, and H. Yokoya. ILC Higgs White Paper. page 152, oct 2013.

[5] H Baer, T Barklow, K Fujii, Y Gao, and a Hoang. [1306.6352] The International Linear Collider Technical Design Report - Volume 2: Physics. *... preprint arXiv:13066352*, 2, jun 2013.

[6] M. Battaglia. Vertex tracking at a future linear collider. *Nucl. Instruments Methods Phys. Res. Sect. A Accel. Spectrometers, Detect. Assoc. Equip.*, 650(1):55–58, sep 2011.

[7] Jerome Baudot, Olena Bashinska, Nathalie Chon-Sen, Wojciech Dulinski, Franziska Hegner, Marie Gelin-Galibel, Rhorry Gauld, Mathieu Goffe, Joel Goldstein, Ingrid Gregor, Christine Hu-Guo, Ulrich Koetz, Andrei Nomerotski, and Marc Winter. Development of Single- and Double-sided Ladders for the ILD Vertex Detectors. mar 2012.

[8] T. Behnke, J. E. Brau, B. Foster, J. Fuster, M. Harrison, J. P. Paterson, M. Peskin, M. Stanitzki, N. Walker, and H. Yamamoto. ILC Technical Design Report Volume 1: Executive Summary. *ILC Tech. Des. Rep. Vol. 1 Exec. Summ.*, 1:1–60, 2013.

[9] Ties Behnke. The international linear collider. *Fortschritte der Phys.*, 58(7-9):622–627, 2010.

[10] Matteo Cacciari, Gavin P Salam, and Gregory Soyez. The anti-k t jet clustering algorithm. 2008.

[11] Constantino Calancha Paredes, A Dubey, H Ikeda, A Ishikawa, S Ito, E Kato, A Miyamoto, T Mori, H Sato, T Suehara, Y Sugimoto, and H Yamamoto. Progress in the development of the vertex detector with fine pixel CCD at the ILC.

[12] CERN. The super proton synchrotron. https://home.cern/about/accelerators/super-proton-synchrotron, 2016.

[13] J. Chadwick. *Possible Existence of a Neutron.* 1932.

[14] Clic home page. http://clic-study.web.cern.ch.

[15] ATLAS Collaboration. Observation of a new particle in the search for the Standard Model Higgs boson with the ATLAS detector at the LHC. *Phys. Lett.*, B716:1–29, 2012.

[16] CMS Collaboration. Observation of a new boson at a mass of 125 GeV with the CMS experiment at the LHC. *Phys. Lett.*, B716:30–61, 2012.

[17] Donut Collaboration, K Kodama, N Ushida, C Andreopoulos, N Saoulidou, G Tzanakos, P Yager, B Baller, W Freeman, B Lundberg, J Morrn, R Rameika, J C Yun, J S Song, C S Yoon, S H Chung, P Berghaus, M Kubanstev, N W Reay, R Sidwell, N Stanton, S Yoshida, S Aoki, T Hara, and J T Rhee. Observation of Tau Neutrino Interactions. 2000.

[18] Jochen Schieck for the DEPFET Collaboration. DEPFET Pixels as a Vertex Detector for the Belle II Experiment. 2013.

[19] G. Contin, E. Anderssen, L. Greiner, J. Schambach, J. Silber, T. Stezelberger, X. Sun, M. Szelezniak, C. Vu, H. Wieman, and S. Woodmansee. The maps based pxl vertex detector for the star experiment. *Journal of Instrumentation*, 10(03):C03026, 2015.

[20] D Cussans. Description of the JRA1 Trigger Logic Unit (TLU), v0.2c. 2009.

[21] A. Denner, S. Heinemeyer, I. Puljak, D. Rebuzzi, and M. Spira. Standard Model Higgs-Boson Branching Ratios with Uncertainties. *Eur. Phys. J.*, C71:1753, 2011.

[22] Deutsches Elektronen-Synchrotron DESY. Marlin, a modular application framework for anal- ysis and reconstruction code based on lcio. http://ilcsoft.desy.de/portal/software_packages/marlin/index_eng.html, 2016.

[23] Deutsches Elektronen-synchrotron Desy and Hamburg Germany. A review of e+ e- Linear Colliders. 22:529–539, 1988.

[24] Test beam at desy. http://particle-physics.desy.de/test_beams_at_desy/index_ger.html.

[25] M Deveaux, S Amar-Youcef, A Besson, G Claus, C Colledani, M Dorokhov, C Dritsa, W Dulinski, I Fröhlich, M Goffe, D Grandjean, S Heini, A Himmi, C Hu, K Jaaskelainen, C Müntz, A Shabetai, J Stroth, M Szelezniak, I Valin, and M Winter. Radiation Tolerance of CMOS Monolithic Active Pixel Sensors with Self-Biased Pixels. 2009.

[26] F. Englert and R. Brout. Broken Symmetry and the Mass of Gauge Vector Mesons. *Physical Review Letters*, 13:321–323, August 1964.

[27] ˜a R Erwin, R H March, W D Walker, M Goldhaber, T D Lee, C N Yang, G Danby, J-M Gaillard, K Goulianos, L M Lederman, N Mistry, M Schwartz, and Z Steinbergert. OBSERVATION OF HIGH-ENERGY NEUTRINO REACTIONS AND THE EXISTENCE OF TWO KINDS OF NEUTRINOS. *Phys. Rev. Phys. Rev. Phys. Rev. Lett.*, 9(6):101–1640, 1961.

[28] Eudaq, a generic data acquisition framework. https://eudaq.github.io.

[29] Eutelescope home page. http://eutelescope.web.cern.ch.

[30] Mueller Felix. Development of a triple gem readout module for a time projection chamber & measurement accuracies of hadronic higgs branching fractions in $\nu\nu$ h at a 350 gev ilc, 2016.

[31] E. Fermi. An attempt of a theory of beta radiation. 1. *Z. Phys.*, 88:161–177, 1934.

[32] R. P. Feynman and M. Gell-Mann. Theory of the fermi interaction. *Phys. Rev.*, 109:193–198, Jan 1958.

[33] Y. Fukuda, T. Hayakawa, E. Ichihara, K. Inoue, K. Ishihara, H. Ishino, Y. Itow, T. Kajita, J. Kameda, S. Kasuga, K. Kobayashi, Y. Kobayashi,

Y. Koshio, M. Miura, M. Nakahata, S. Nakayama, A. Okada, K. Okumura, N. Sakurai, M. Shiozawa, Y. Suzuki, Y. Takeuchi, Y. Totsuka, S. Yamada, M. Earl, A. Habig, E. Kearns, M. D. Messier, K. Scholberg, J. L. Stone, L. R. Sulak, C. W. Walter, M. Goldhaber, T. Barszczxak, D. Casper, W. Gajewski, P. G. Halverson, J. Hsu, W. R. Kropp, L. R. Price, F. Reines, M. Smy, H. W. Sobel, M. R. Vagins, K. S. Ganezer, W. E. Keig, R. W. Ellsworth, S. Tasaka, J. W. Flanagan, A. Kibayashi, J. G. Learned, S. Matsuno, V. J. Stenger, D. Takemori, T. Ishii, J. Kanzaki, T. Kobayashi, S. Mine, K. Nakamura, K. Nishikawa, Y. Oyama, A. Sakai, M. Sakuda, O. Sasaki, S. Echigo, M. Kohama, A. T. Suzuki, T. J. Haines, E. Blaufuss, B. K. Kim, R. Sanford, R. Svoboda, M. L. Chen, Z. Conner, J. A. Goodman, G. W. Sullivan, J. Hill, C. K. Jung, K. Martens, C. Mauger, C. McGrew, E. Sharkey, B. Viren, C. Yanagisawa, W. Doki, K. Miyano, H. Okazawa, C. Saji, M. Takahata, Y. Nagashima, M. Takita, T. Yamaguchi, M. Yoshida, S. B. Kim, M. Etoh, K. Fujita, A. Hasegawa, T. Hasegawa, S. Hatakeyama, T. Iwamoto, M. Koga, T. Maruyama, H. Ogawa, J. Shirai, A. Suzuki, F. Tsushima, M. Koshiba, M. Nemoto, K. Nishijima, T. Futagami, Y. Hayato, Y. Kanaya, K. Kaneyuki, Y. Watanabe, D. Kielczewska, R. A. Doyle, J. S. George, A. L. Stachyra, L. L. Wai, R. J. Wilkes, and K. K. Young. Evidence for oscillation of atmospheric neutrinos. *Phys. Rev. Lett.*, 81:1562–1567, Aug 1998.

[34] Geant4 multiple scattering. http://geant4.cern.ch/G4UsersDocuments/UsersGuides/PhysicsReferenceManual/html/node34.html.

[35] Gear home page. http://ilcsoft.desy.de/portal/software_packages/gear/index_eng.html.

[36] H. Georgi and S. L. Glashow. Unity of All Elementary Particle Forces. *Phys. Rev. Lett.*, 32:438–441, 1974.

[37] Steven Green, John Marshall, Mark Thomson, and Boruo Xu. Cambridge linear collider group - home page. http://www.hep.phy.cam.ac.uk/linearcollider/calorimetry/.

[38] Peter W. Higgs. Broken symmetries and the masses of gauge bosons. *Phys. Rev. Lett.*, 13:508–509, Oct 1964.

[39] A Himmi, G Doziere, O Torheim, C Hu-Guo, and M Winter. A Zero Suppression Micro-Circuit for Binary Readout CMOS Monolithic Sensors. pages 3–7.

[40] ICFA. Final International Technology Recommendation Panel Report. (September), 2004.

[41] The linear collider collaboration home page. http://www.linearcollider.org.

[42] Ilcsoft homepage. http://ilcsoft.desy.de. Accessed: 2010-09-30.

[43] IPHC. *MIMOSA26 User Manual.*

[44] H Jansen, S Spannagel, J Behr, A Bulgheroni, G Claus, E Corrin, D G Cussans, J Dreyling-Eschweiler, D Eckstein, T Eichhorn, M Goffe, I M Gregor, D Haas, C Muhl, H Perrey, R Peschke, P Roloff, I Rubinskiy, and M Winter. Performance of the EUDET-type beam telescopes.

[45] Jérôme Baudot. TAF short manual. http://www.iphc.cnrs.fr/IMG/pdf/taf_shortdoc.pdf, 2015.

[46] Goldstein Joel. Low mass vertex detector r&d. WG4 meeting: low-mass engineering and power dissipation, 2010.

[47] Kleinwort and Blobel (DESY). General broken lines documentation. http://www.desy.de/~kleinwrt/GBL/doc/cpp/html/, 2016.

[48] Kleinwort and Blobel (DESY). Millepede-ii. http://www.desy.de/~kleinwrt/MP2/doc/html/index.html, 2016.

[49] Oleg Kuprash. Power pulsing of the CMOS sensor Mimosa 26. *Nucl. Instruments Methods Phys. Res. Sect. A Accel. Spectrometers, Detect. Assoc. Equip.*, 732:519–522, 2013.

[50] Lcio homepage. http://lcio.desy.de.

[51] T. D. Lee and C. N. Yang. Question of Parity Conservation in Weak Interactions. *Physical Review*, 104:254–258, October 1956.

[52] Yiming Li, Chris Damerell, Rui Gao, Rhorry Gauld, Jaya John John, Peter Murray, Andrei Nomerotski, Konstantin Stefanov, Steve Thomas, Helena Wilding, and Zhige Zhang. ISIS2: Pixel Sensor with Local Charge Storage for ILC Vertex Detector. page 11, jun 2010.

[53] Ronald Lipton. Muon Collider: Plans, Progress and Challenges. page 6, apr 2012.

[54] Cousin Loïc. Trajectométrie dans le cadre du projet européen aida, 2015.

[55] O. Markin. Backgrounds at future linear colliders. feb 2014.

[56] Nobert Meyners. Conversion targets. http://particle-physics.desy.de/test_beams_at_desy/beam_generation/e259596/conversion_targets.pdf, 2002.

[57] Mokka home page. http://ilcsoft.desy.de/portal/software_packages/mokka/.

[58] E. Noether. Invariante variationsprobleme. *Nachrichten von der Gesellschaft der Wissenschaften zu Göttingen, Mathematisch-Physikalische Klasse*, 1918:235–257, 1918.

[59] A Nomerotski, L Bachynska, J Baudot, N Chon-Sen, G Claus, R De Masi, M Deveaux, W Dulinski, R Gauld, M Goffe, J Goldstein, I.-M Gregor, Ch Hu-Guo, M Imhoff, U Koetz, W Lau, C Muntz, C Santos, C Schrader, M Specht, J Stroth, M Winter, and S Yang. PLUME collaboration: Ultra-light ladders for linear collider vertex detector.

[60] K. A. Olive et al. Review of Particle Physics. *Chin. Phys.*, C38:090001, 2014.

[61] PLUME project. http://www.iphc.cnrs.fr/PLUME.html.

[62] Pythia home page. http://home.thep.lu.se/~torbjorn/Pythia.html.

[63] Burton Richter. Very High-Energy electron-Positron Colliding Beams for the Study of the Weak Interactions. *Nucl. Instrum. Meth.*, 136:47, 1976.

[64] RH Richter, L Andricek, P Fischer, K Heinzinger, P Lechner, G Lutz, I Peric, M Reiche, G Schaller, M Schnecke, F Schopper, H Soltau, L Str uder, J Treis, M Trimpl, J Ulrici, and N Wermes. Design and technology of DEPFET pixel sensors for linear collider applications. *Nucl. Instruments Methods Phys. Res. A*, 511:250–256, 2003.

[65] Maria Robert. Study of the time-dependent cp asymmetry in d^0 decays in the belle ii experiment, 2015.

[66] Adrian Signer. ABC of SUSY. *Journal of Physics G: Nuclear and Particle Physics*, 36(7):073002, jul 2009.

[67] The standard model of particle physics. http://www.brighthub.com/science/space/articles/84750.aspx.

[68] Simon Spannagel and Hendrik Jansen. Gbl track resolution calculator v2.0, April 2016.

[69] The ATLAS Collaboration. Study of the spin of the Higgs-like boson in the two photon decay channel using 20.7 fb-1 of pp collisions collected at \sqrt{s} = 8 TeV with the ATLAS detector. *ATLAS NOTE*, 2013.

[70] Junping Tian and Keisuke Fujii. Measurement of Higgs couplings and self-coupling at the ILC. *Eur. Phys. Soc. Conf. High Energy Phys.*

[71] I Valin, C Hu-Guo, J Baudot, G Bertolone, A Besson, C Colledani, G Claus, A Dorokhov, G Dozière, W Dulinski, M Gelin, M Goffe, A Himmi, K Jaaskelainen, F Morel, H Pham, C Santos, S Senyukov, M Specht, G Voutsinas, J Wang, and M Winter. A reticle size cmos pixel sensor dedicated to the star hft. *Journal of Instrumentation*, 7(01):C01102, 2012.

[72] Whizard home page. https://whizard.hepforge.org.

[73] Marc Winter. Development of Swift, High Resolution, Pixel Sensor Systems for a High Precision Vertex Detector suited to the ILC Running Conditions. 2009.

[74] C. S. Wu, E. Ambler, R. W. Hayward, D. D. Hoppes, and R. P. Hudson. Experimental Test of Parity Conservation in Beta Decay. *Physical Review*, 105:1413–1415, February 1957.